A Component-Level Study on the Effect of Warm Forming on Formability and Springback of Aluminum Alloy Brazing Sheet

by

Kyu Bin Han

A thesis
presented to the University of Waterloo
in fulfillment of the
thesis requirement for the degree of
Master of Applied Science
in
Mechanical and Mechatronics Engineering

Waterloo, Ontario, Canada, 2018

Author’s Declaration

I hereby declare that I am the sole author of this thesis. This is a true copy of the thesis, including final revisions, as accepted by my examiners.

I understand that my thesis may be made electronically available to the public.

Abstract

This thesis investigates the effect of warm forming (up to 350°C) on the formability and springback behavior of AA3003/AA4045 brazing sheet (0.2 mm gauge) for three temper conditions: O-, H22- and H24-tempers. The geometry under study is referred as a surrogate heat-exchanger component (SHC) and contains complex features found on commercial automotive thermal management systems.

The hardening behavior of the material was modeled with the well-known extended Nadai phenomenological model, which captured the thermal softening, strain rate sensitivity and negative hardening behavior at elevated temperatures. Tensile simulations were performed and compared to the experimental results, demonstrating good agreement.

Four tooling configurations that consider different die designs, blank geometries, and forming method were developed to improve the formability and wrinkling behavior associated with the aggressive geometries found in the SHC. Finite element models were used to predict the results of the tooling configurations in the development process. The tooling configuration with the best formability, wrinkling behavior and process efficiency was selected. Formability improvement was not clearly observed with the warm forming process. However, preliminary observations show that the reduction in springback using warm forming was very effective.

With the selected tooling configuration, more in-depth springback characterization was completed for a wide range of forming process parameters such as: temperature, punch load, sheet direction, and holding time. At room temperature, H22- and H24-tempers exhibited significantly higher springback compared to O-temper, which can be attributed to the higher strength of the harder tempers. The effect of warm forming on springback was negligible for the O-temper but significant for harder tempers. For H24, a springback reduction up to 88% was observed at 325°C relative to room temperature at high punch load condition.

Numerical simulations were performed to predict the springback and were compared to the experiments. The simulations considered several different factors that affect springback behavior

such as through-thickness compression, thermal expansion and bi-metallic strength gradient. The simulation results qualitatively captured the effect of temperature on springback in the experiments with moderate quantitative agreement. The largest discrepancy was associated with an inability of the model to accurately predict the effect of punch load on springback.

Overall, this study has served to characterize warm forming technology for a potential commercial application in the automotive heat exchanger industry. It was shown that the warm forming process did not offer significant benefit in terms of formability and wrinkling behavior; tooling optimization was more effective for formability and wrinkle control. However, warm forming was very beneficial in reducing springback, thus adoption of this technology should be very useful in applications where part dimensional accuracy is critical.

Acknowledgement

First and foremost, I would like to thank Prof. Michael Worswick for giving me the opportunity to work on this project. His guidance and support throughout the duration of the graduate studies were invaluable. Working under him was one of the greatest learning experiences I've ever had. I would also like to thank Dr. Sooky Winkler, Dr. Srihari Kurukuri and Ryan George for their help in this project.

The financial support from Dana Canada Corporation, Automotive Partnerships Canada, the Natural Sciences and Engineering Research Council (NSERC), the Canada Foundation for Innovation, the Ontario Research Fund and the Canada Research Chairs Secretariat is gratefully acknowledged.

The experiments in this thesis could not have been possible without the help from Eckhard Budziarek and Tom Gawel, who provided technical support in the laboratory.

The time I spent in the Forming and Impact Mechanics Research Group was truly enjoyable due to these individuals: Sante DiCecco, Sam Kim, Chi-Hsiang Liao, Jacqueline Noder, Cameron O'Keeffe, Kaab Omer, Cale Peister, Pedram Samadian, David Shen, and Amir Zhumagulov. Thank you all.

Most importantly, I thank my parents for their endless love and encouragement. I could not have done it without them. Lastly, I thank Karen Ma for being part of this journey.

To my parents

Table of Contents

List of Figures

List of Tables

1 Introduction

For decades, the automotive industry has been dominated by internal combustion engines. However, with more strict regulations on fuel economy and emissions, the industry is being pushed towards electric vehicles and hybrid electric vehicles (EVs and HEVs) that use batteries as energy storage systems. The batteries in EVs and HEVs require effective thermal management since batteries have a very narrow operating temperature range for optimal performance and cycle life [1]. For example, the performance of Lithium-ion cells widely used in EVs and HEVs degrades at temperature beyond 65^0C or below 0^0C [2]. Therefore, automotive manufacturers integrate thermal management systems within their vehicles' battery pack design. For high energy density batteries, an active liquid cooling system is used for the most efficient results [3]. Typically, the battery pack comprises stacks of rectangular cells with cooling plates sandwiched in between the cells. The battery cooling plate (Figure 1) consists of very shallow serpentine channels through which a coolant is pumped to extract heat from the battery cells.

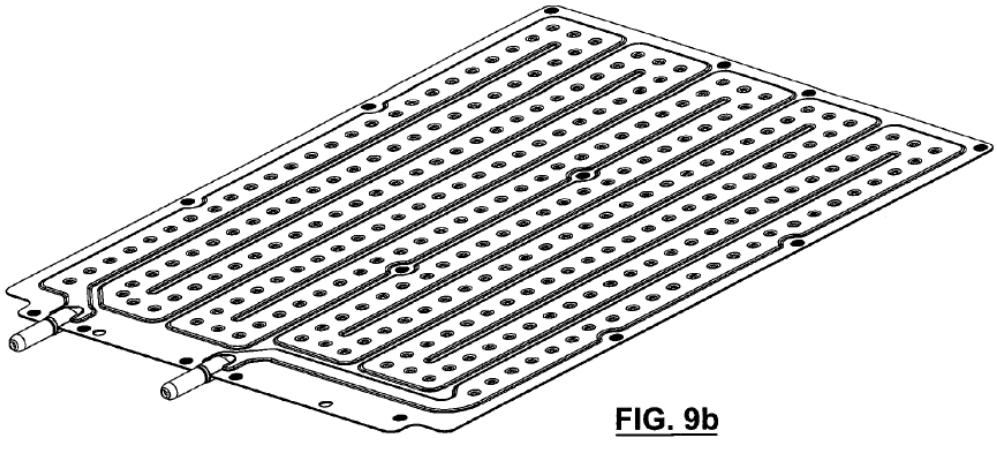

Figure 1: A typical battery cooling plate by Dana Canada Corporation [4]

The favored material choice for the battery cooling plate has been aluminum alloy sheet because aluminum alloys have high strength-to-weight ratio, good thermal conductivity and good corrosion resistance. The most common way of utilizing aluminum alloys in the manufacture of the battery cooling plate is in the form of brazing sheets [5]. An aluminum alloy brazing sheet is a laminate composite structure consisting of an AA3XXX core alloy that provides structural strength and an AA4XXX clad alloy with lower melting temperature as a filler metal. During the brazing process, the clad alloy melts and joins the two halves of the battery plates together via a process of wetting and capillary action.

Unfortunately, brazing sheet materials can exhibit poor formability and excessive springback; this is particularly the case for brazing sheet with harder tempers (e.g. H22 or H24) which are higher strength and more durable compared to softer, more easily formed O-temper sheet. These limitations are normally overcome using complex forming operations using multi-stage progressive die systems that are expensive. The current work is focused on utilizing warm forming techniques to improve the formability and springback behavior of aluminum alloy brazing sheet, ideally reducing the complexity of the required tooling systems. A small-scale component that is fully representative of the commercial battery plate is developed which will provide useful insights regarding warm forming at a component-level. Forming experiments are performed with several different tooling configurations and a wide range of process parameters are considered for the springback control. Numerical models are also developed to simulate and provide greater insight into the experiments.

A description of the research results is provided starting in chapter 2 of this thesis. The balance of this chapter serves to introduce the current state of the art in terms of warm forming and simulation of forming processes.

1.1 Warm Forming

Generally, sheet metal forming is carried out at ambient temperature. In the automotive industry, low carbon steel has been a common material of choice due to its excellent formability at ambient temperature, reasonable strength and low cost. The application of aluminum alloys has been

limited because of their relative poor formability despite their high strength-to-weight ratio and corrosion resistance. In order to overcome the formability challenge, warm forming emerged as a promising solution in the 1970s, as it was discovered that an aluminum-magnesium alloy could achieve a total elongation of 300% at about 250^0C [6]. Warm forming refers to the process of forming sheet metals at elevated temperatures below the recrystallization temperature. Warm forming improves the formability of aluminum alloys by strain rate hardening [7]. At elevated temperatures, aluminum alloys exhibit increased positive strain rate sensitivity that prevents localized necking by improving the uniformity of strain distribution and stabilizing any inhomogeneities [8,9]. The effect of warm forming can be further enhanced by applying a temperature gradient, but isothermal forming is often preferred due to the complexity of non-isothermal tooling design. An additional benefit of warm forming is improved springback behavior due to decreased flow stress at elevated temperatures [10]. The reduction in flow stress is driven by the enhanced dynamic recovery mechanism at elevated temperatures [11]. A typical warm forming tooling schematic, in this case for non-isothermal warm forming, is shown in Figure 2.

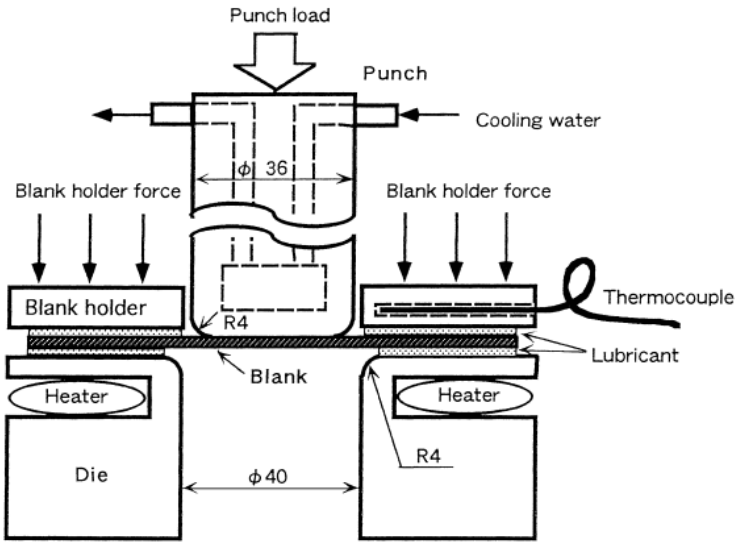

Figure 2: Warm forming tooling schematic[12]

The increase in formability and improvement in springback characteristics that arise from warm forming could allow for parts with greater complexity to be formed and increase the usage of aluminum alloys in the automotive industry.

1.2 Formability

Although aluminum alloys have seen some adoption in the automotive industry due to their high strength-to-weight ratio, their usage is limited due to their poor formability at room temperature in comparison to convention steel. The formability of sheet metal is measured based on what is known as the forming limit which is defined as the strain state at which a localized thinning initiates [13]. The two most important factors affecting the formability of sheet metal are the strain hardening exponent and strain rate sensitivity [14]. Initially, very little laboratory formability data for aluminum alloys existed, thus Hecker [15] performed a variety of process experiments (i.e. deep drawing, bending, flanging and stretching) on aluminum alloys at room temperature and compared the results to those of low carbon steel. It was found that all of the aluminum alloys tested (3003-O, 5052-O, 6061-T4 and *etc.*) had lower forming limits relative to steel. In addition, aluminum alloys exhibited lower Lankford coefficients and strain hardening capacity compared to low carbon steel. It was concluded that aluminum alloys have very poor stamping performance in all modes of sheet metal forming. According to Davies *et al.* [16], studies regarding the phenomenon of superplasticity at elevated temperature in different metals including aluminum alloys goes all the way back to the 1920s. Under certain conditions, significant elongations up to 1000% have been documented. More recently, there have been numerous studies reported in the literature showing improvement in formability by utilizing warm forming. Many of the early studies were done on 5000-series Al-Mg alloys. Ayres [17] measured the ductility of AA5182-O sheet and found that elongation is greatly enhanced by dynamic recovery at elevated temperatures. He observed that the ductility is a strong function of strain rate at elevated temperature and obtained 175% elongation at 250^0C compared to 27% at ambient temperature. The majority of the increased elongation was from an increase in the post uniform deformation within the diffuse necking regime. Shehata *et al.* [6] performed uniaxial tensile tests and found that the ductility of aluminum-magnesium alloys was greatly enhanced up to five times at 300^0C. The total elongation was shown to increase with decreasing strain rate and a reduction in flow stress with increasing temperature was also demonstrated. Their results are shown in Figure 3. Hot pressing tests were also performed and it was shown that the maximum cup height increased significantly at elevated temperatures. One useful effect observed in the hot pressing test was a rather small effect of raising temperature beyond 150^0C up to 500^0C. In addition, the effect of punch speed was not significant

as expected. This behavior indicates that warm forming could be implemented with fairly low temperatures and at conventional press speeds.

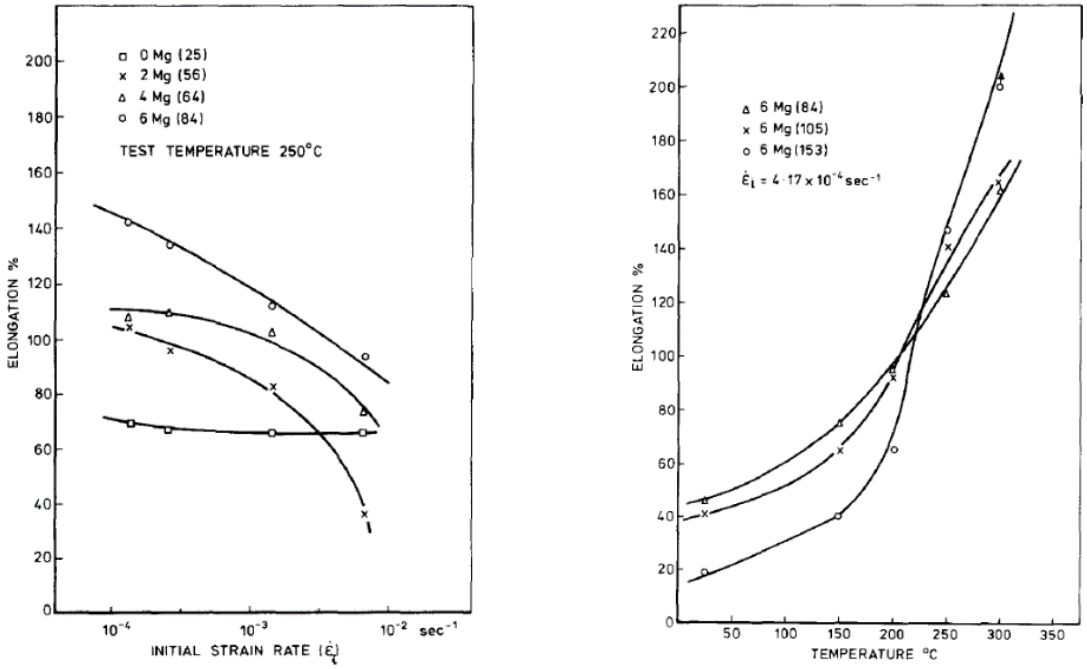

(a) (b)

Figure 3: (a) Effect of strain rate on failure strain (b) Effect of temperature on failure strain [6]

Ayres *et al.* [8] performed tensile tests and cup forming tests at elevated temperatures for AA5182-O. It was found that at elevated temperatures, the magnitude of strain hardening diminishes and the effect of strain rate hardening dominates. At 200^0C, the forming limit of the plane strain condition was measured as twofold greater than that of room temperature. It was also observed that at the elevated temperatures, the cups made with slower punch speed had a wider and higher strain distribution at failure as seen in Figure 4. More recently, Li and Ghosh [10] performed uniaxial tensile tests on AA5182, AA5754 and AA6111-T4 aluminum alloys in the temperature range of 200^0C to 350^0C. The elongations increased significantly with increasing temperature and decreasing strain rate. The majority of the elongations at elevated temperatures were in the post-uniform regime and were attributed to higher strain rate hardening at elevated temperature.

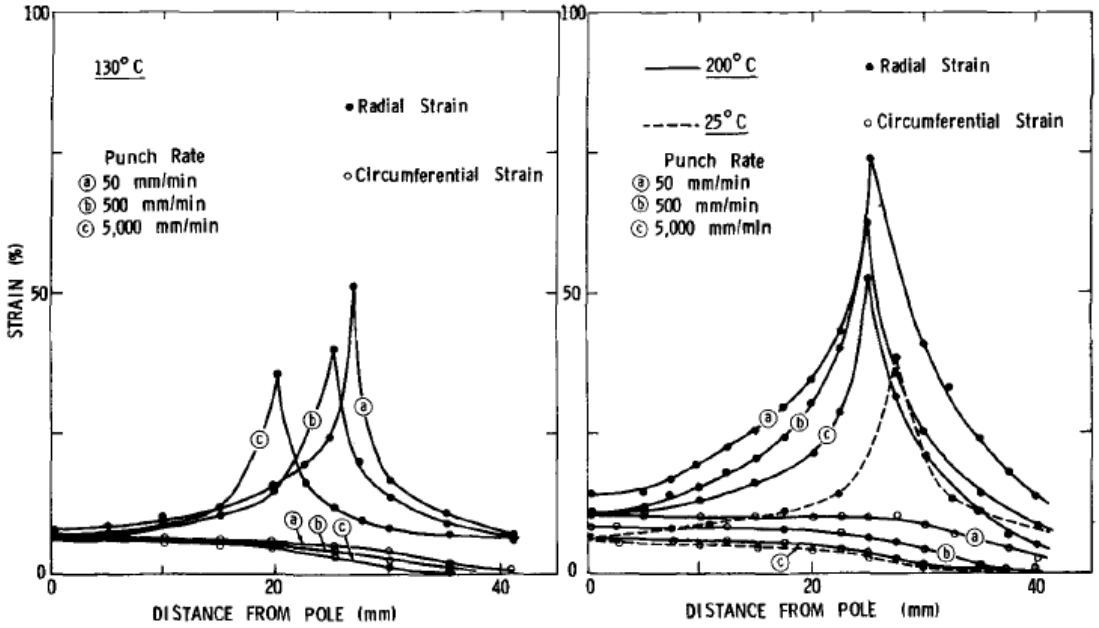

Figure 4: Strain distribution at failure at different temperatures and punch speeds [8]

Li and Ghosh [18] extended their investigation by studying biaxial warm forming on the same aluminum alloys in the temperature range of 200^0C to 350^0C under both isothermal and non-isothermal conditions. The part depth increased with the tooling temperature (Figure 5) but it was found that applying a thermal gradient (50^0C) between the die and the punch resulted in greater formability. The cold punch promoted drawing rather than stretching of the part leading to a greater part depth. It was also found that the forming limit strains for the three alloys formed at 250^0C were comparable to A-K steel formed at room temperature. At 350^0C, the forming limit strains were 2-3 times greater than that of A-K steel formed at room temperature. Lastly, the effect of warm forming was considerably greater for strain hardening alloys compared to precipitation hardening alloys. Naka *et al.* [12] explored the effect of forming speed and temperature on the deep drawability of cylindrical cups with 5083-O aluminum alloy. The tests were done non-isothermally with the punch cooled to room temperature and the rest of the tooling heated up. It was found that the limiting draw ratio (LDR) increased drastically with increasing die temperature and decreased with increasing forming speed. The temperature increase lowered the deformation resistance of the flange due to a reduction in flow stress. The increase in punch speed lowers the LDR because the fracture strains at elevated temperatures are reduced to the fracture strain at room temperature due to strain rate hardening. Bolt *et al.* [19] investigated the effect of temperature by

forming box-shaped and conical rectangular geometries with AA1050, AA5754 and AA6016 series aluminum sheet in the temperature range of 100^0C to 250^0C. The maximum increases in cup height of 25% at 175^0C and 65% at 250^0C were observed for the box shaped and conical rectangular geometries, respectively. The temperature range used in the experiment did not have detrimental effects on the strength of the material after forming which was validated by checking the hardness of the as-formed parts.

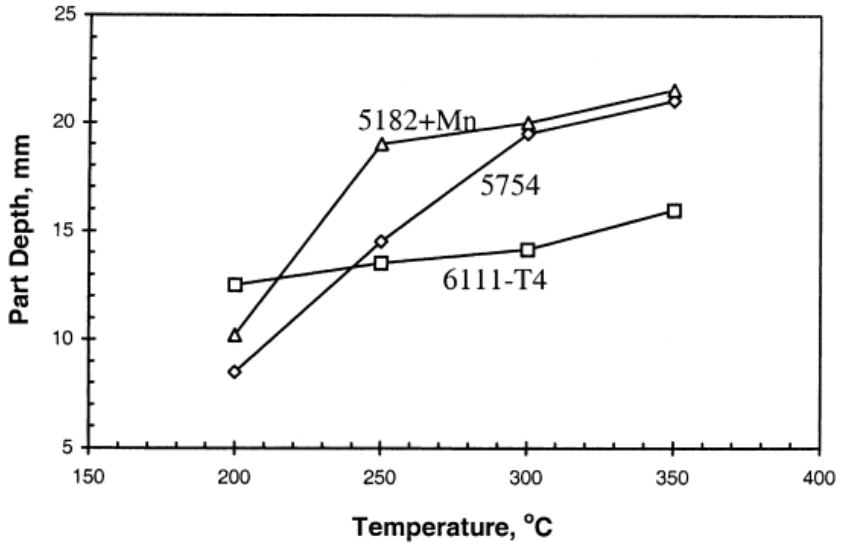

Figure 5: Effect of temperature on part depth for different aluminum alloys [18]

Takuda *et al.* [20] performed non-isothermal cylindrical deep drawing experiments with an aluminum alloy sheet A5182-O. The tests were conducted at room temperature and at warm conditions with the die and blank holders at 250^0C and the punch kept at room temperature. Test specimens formed at each condition are shown in Figure 6.

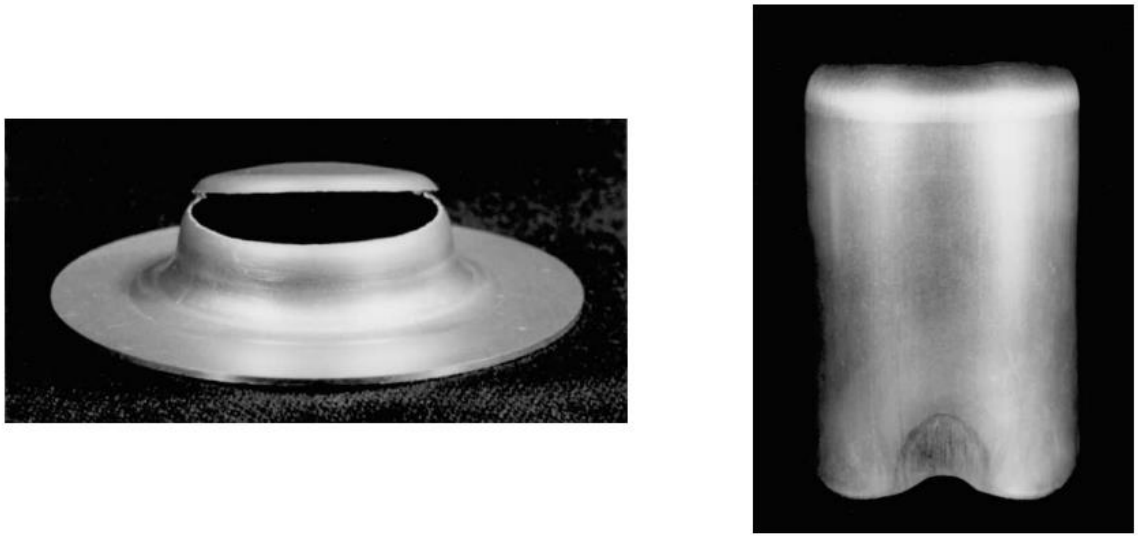

(a) **(b)**

Figure 6: (a) Deep drawn cup at room temperature (b) Deep drawn cup at elevated temperature [20]

At room temperature, fracture occurred at the punch corner, but the cup was successfully drawn fully for the warm condition. The punch cooled the corners rapidly increasing the flow stress thus preventing strain localization at the corners and distributing the strain along the sidewalls. Kaya [21] did an experimental study on AA5754-O and AA5052-H32 and the main objective was to determine the effects of various process parameters on cylindrical cup deep drawing at elevated temperatures. It was found that a PTFE based lubricant performed very well at elevated temperature conditions. The lubrication helped in attaining higher punch velocities. The temperature increase reduced the amount of sheet thinning at the cup bottom corner whereas a punch velocity increase had the opposite effect (Figure 7). The temperature increase also helped in achieving the maximum punch velocity. There also has been efforts to numerically simulate the warm forming process to predict the experimental results. Takuda *et al.* [20] performed a 2-D thermo-mechanical finite element analysis (FEA) to simulate a non-isothermal cylindrical cup deep drawing experiment. The flow curves were obtained from uniaxial tension tests and modeled with a power law hardening law. The simulation was able to predict the thickness profile of the blank, capturing the necking response around the punch corner at room temperature. The FEA was also capable of predicting the successful drawn cup at elevated temperatures. The comparison between the experimental and simulated results showed the reliability and effectiveness of the finite element method that incorporates plastic deformation and temperature together.

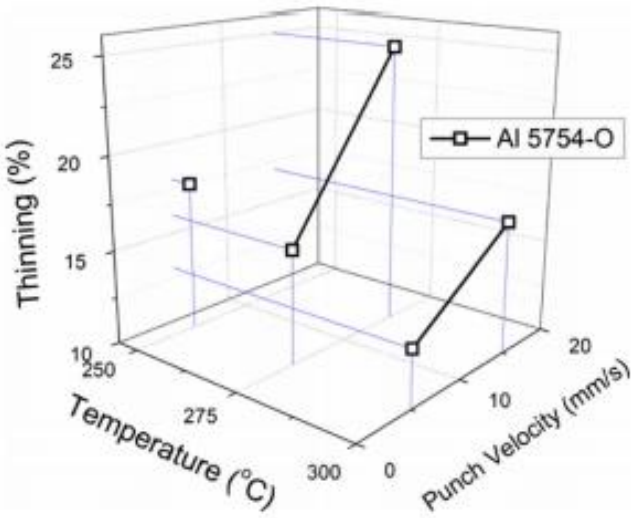

Figure 7: Effect of temperature and punch velocity on sheet thinning of AA5754-O [21]

Van den Boogaard *et al.* [22] simulated cylindrical cup deep drawing of AA5754-O aluminum alloy using coupled thermo-mechanical finite element method and the Bergstrom [23] constitutive model that accounted for thermal softening and strain rate sensitivity. Three different yield functions (von Mises, Hill-48 [24] and Vegter [25]) were implemented and compared with the experimental results. The von Mises model underestimated the shear deformation which is the main deformation mode in cup deep drawing. All yield functions predicted too much thinning at the bottom of the cup, especially using the Hill-48 model due to poor prediction of flow stress within the biaxial regime. It was concluded that the yield function has a significant impact on numerical simulations of cylindrical cup deep drawing. It was also shown that the Bergstrom model was able to capture the flow stress behavior between room temperature and 200^0C at intermediate strain rates. At higher temperatures, the response started to deviate before the maximum stress was reached and under predicted the overall response. Abedrabbo *et al.* [26] modeled an AA3003-H111 aluminum sheet with a temperature-dependent Barlat YLD96 [27] anisotropic yield function and temperature- and strain rate-dependent modified power law. The material model was validated with thermo-mechanical simulations of limiting dome height tests and it was shown that the model accurately predicted the deformation behavior and the failure locations. Palumbo and Tricarico [28] performed warm deep drawing experiments and thermo-mechanical finite element analysis considering AA5754-O. It was found that punch speed and the thermal gradient between the blank holder and punch have significant impact on the formability.

The limiting draw ratio increased up to 44% with respect to the room temperature condition. The finite element simulation was modeled with a Von Mises yield surface and physics-based Bergstrom hardening model and it successfully predicted the experimental results.

Tari *et al.* [29] simulated warm forming of AZ31B magnesium alloy sheet by incorporating the elevated temperature constitutive behavior of the material. The yield surface was modelled with a modified CPB-type yield function [30], [31] and the hardening behavior was captured with Cowper-Symonds strain hardening model and extended Nadai model [32]. The simulation was able to provide qualitative predictions of punch load and strain distribution for elevated temperature limiting dome height and deep drawing experiments. Ghavam *et al.* [33] performed a numerical simulation of non-isothermal deep drawing with an AA3003 aluminum alloy. The material was modelled with the Barlat YLD2000 yield criterion [34] to capture the anisotropic behavior and the Bergstrom hardening rule to predict the temperature and strain rate dependence. The simulation accurately predicted the punch load-displacement response at different process parameters including temperature, punch speed, binder force and lubrication condition. Bagheriasl *et al.* [35] also successfully predicted the mechanical behavior of an AA3003 aluminum alloy at a component level by using the Barlat YLD2000 yield criterion and the Bergstrom hardening rule. Both the punch force and failure locations were captured accurately. Kurukuri *et al.* [36] predicted the constitutive behavior of AA3003 sheet under warm forming conditions with three different hardening laws: extended-Nadai, Bergstrom and Nes [37] models. The models were compared and assessed with the ability to capture work hardening behavior and strain rate jump response. All three models were capable of describing the work hardening behavior with great accuracy. For the strain rate jump response, the Nes model had the best accuracy due to its strong physics-based nature.

There also have been studies regarding warm forming of high strength aluminum alloys such as AA7075. Dicecco *et al.* [38] used two different localization detection methodologies to construct forming limit curves (FLC) of AA6013-T6 at room temperature and 250°C. The two methods yielded very different results at 250°C, emphasizing the need for a validated method for generating warm FLCs. Both methods were able to capture the formability increase at elevated 250°C. Wang *et al.* [39] performed tensile and limiting dome height tests on AA7075-T6. The tensile tests show

that temperature did not have an effect on the mechanical behavior of AA7075 below 140^0C. Above this temperature, the flow stress decreased and elongation increased with increasing temperature. The limiting dome height increased significantly with increasing temperature and at 220^0C, the limiting dome height was greater than that of AA5182-O at room temperature which is known to have good formability. A dramatic loss in strength was observed, however, for tests above 220^0C, emphasizing the importance of limiting temperature in warm forming of precipitation hardening alloys. Kumar *et al.* [40] investigated warm forming of AA7020-T6 alloy sheet by performing tensile, Swift-cupping and cross-die tests. The tensile test results show that the yield strength and ultimate tensile strength decreased with increasing temperature due to dissolution of GP zones and η' precipitates. At high temperatures, the fracture strain, limiting dome ratio and cup depth increased as a result of dynamic recovery which stabilized the deformation and annihilated dislocations. The strength of T6 temper material decreased up to 30% with warm forming compared to the as-received condition.

There have been a limited number of studies conducted on aluminum brazing sheets, the material of interest in the current study. Bagheriasl *et al.* [41] performed limiting dome height experiments on a 0.5mm thick AA3003 brazing sheet at elevated temperatures and different punch speeds. Forming limit diagrams were developed at different temperatures and it was found that the limit strain increased significantly at temperatures above 100^0C. The limit strain for plane strain conditions at 250^0C increased by 229% compared to that of room temperature. The formability increased with decreasing punch speed but the effect was not as significant as increasing the temperature. McKinley *et al.* [42] investigated the effect of warm forming on the formability of AA3003 brazing sheet by performing non-isothermal cylindrical cup deep drawing experiments. The cups were formed with 228.6 mm diameter circular blanks with 0.5 mm thickness in a die set with temperatures ranging from 25^0C to 300^0C. The cup could not be drawn successfully when the tooling temperature was below 150^0C. The cups formed successfully at the temperatures above 200^0C. It was also observed that the acceptable blank holder force increased with increasing die temperature, indicating improved formability. Furthermore, tensile test at 250^0C showed a 200% increase in the failure strain and a very large post-uniform elongation. Jain *et al.* [43] performed limiting dome height experiments on the AA3003 brazing sheet used in the current study for three different temper conditions in the temperature range of 25^0C to 250^0C at two forming speeds. A

maximum of 30% increase in dome height was observed at 250^{0}C compared to the height at 25^{0}C. All three tempers exhibited formability increase with increasing temperature but the effect was reduced for harder temper materials. An increase in forming speed from 0.4 mm/s to 1.6 mm/s decreased the formability by up to 9% at 250^{0}C.

1.3 Springback

Bending and stretching operations are sheet metal forming processes used widely in the automotive industry to manufacture components such as body panels. One of the biggest challenges faced by these processes is springback, a geometrical discrepancy in the formed part between the fully loaded (within the tooling) and unloaded states (after removal from tooling). Springback is caused by the elastic recovery of the internal stress after the forming load is removed. A schematic of springback phenomenon in stretch forming process is shown in Figure 8. An equal and opposite moment M changes the radius of curvature from R to R_f once the load is removed and forms an equilibrium with the residual stress distribution that satisfies the force and moment balance [44].

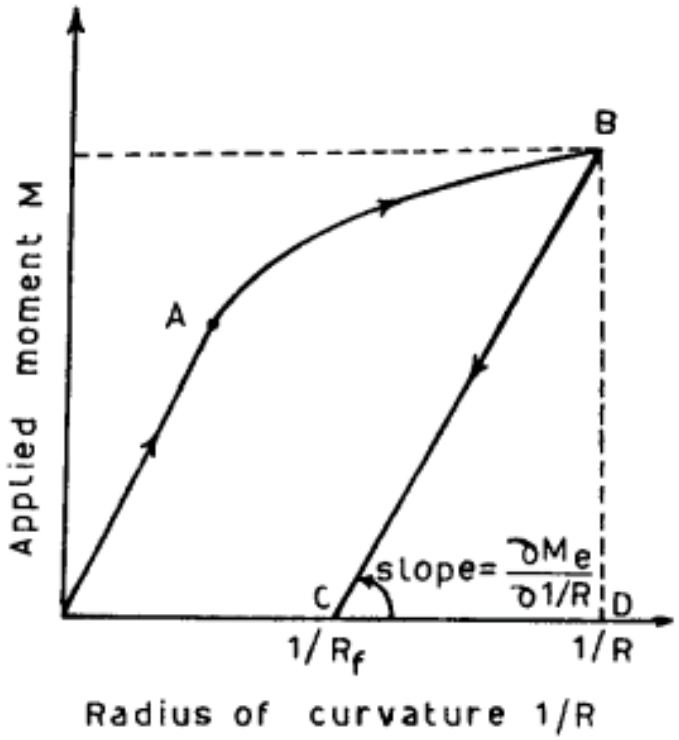

Figure 8: Applied moment vs curvature during forming and springback [44]

1.3.1 Influence of Process Parameters on Springback

The amount of springback is affected by several process parameters such as the applied tension, geometry of the component, the bending radius and the mechanical properties of the material. The work done by Panthi *et al.* [45] showed the influences of different parameters on springback in a typical sheet metal bending process. It was shown that springback increased with increasing yield strength and decreasing elastic modulus. This was also validated in the v-bending experiments done by Mori *et al.* [46]. More springback was observed when the tensile strength-to-elastic modulus ratio increased, as shown in Figure 9.

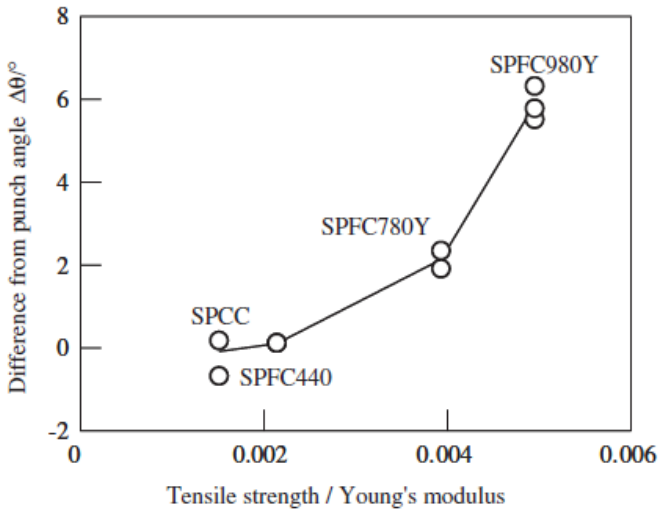

Figure 9: Effect of tensile strength-to-elastic modulus on springback [46]

Verma *et al.* [47] did an analytical study on simple bending of high strength steel and found that sheet thickness has a great impact on springback. An increase in sheet thickness led to reduced springback. The trend was also shown experimentally in the air bending process performed by Garcia-Romeu *et al.* [48]. In U-bending experiments done by Samuel [49], springback increased with increasing punch radius and decreasing die radius. This is in an agreement with work done by Yoshida *et al.* [50] and Ouakdi *et al.* [51]. Samuel [49] also studied the effect of friction on springback. It was observed that springback decreased with an increase in the coefficient of friction. A draw-bending simulation performed by Li *et al.* [52] exhibited the same results regarding the coefficient of friction. Many researchers have reported that texture-based anisotropy and deformation-induced anisotropy (Bauschinger effect) affect springback. Verma *et al.* [47]

evaluated the effect of normal anisotropy on the amount of springback. A numerical simulation was done with the Hill-48 yield surface and isotropic hardening and it was shown that springback increased with normal anisotropy. Dongjuan *et al.* [53] developed an analytical model for the U-bending process to predict springback using the Hill-48 yield surface. The model took into account the effect of deformation history, thinning and neutral surface shift with three different material hardening types (kinematic, isotropic and combined). It was concluded that springback is underestimated when isotropic hardening is applied and overestimated when kinematic hardening is applied. It was suggested to use the combined hardening law for the most accurate results. An increase in springback with increasing normal anisotropy was also observed. Gau *et al.* [54] experimentally investigated the Bauschinger effect on springback predictions for different steels and AA6111-T4. It was observed that the Bauschinger effect is negligible for the steels studied but significant for AA6111-T4. Figure 10 shows the Bauschinger effect for AA6111-T4 where 'B' indicates bending and 'R' indicates reverse-bending. Springback decreased considerably with cyclical loading.

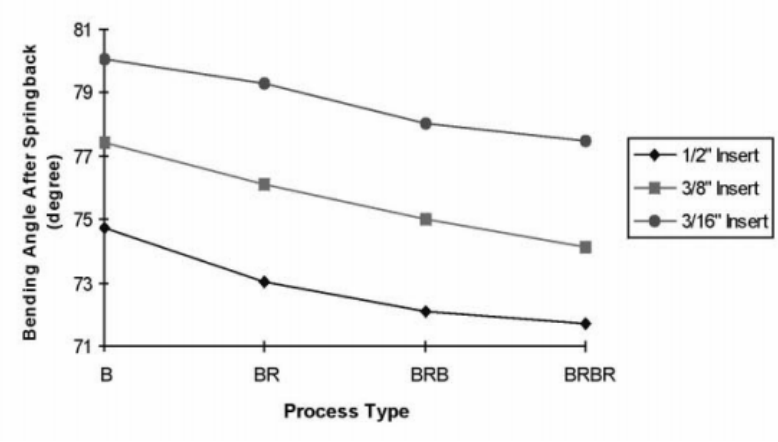

Figure 10: The Bauschinger effect on springback [54]

1.3.2 Springback Reduction Methods

Springback inhibits the dimensional accuracy required for subsequent downstream assembly processes such as welding and brazing operations. Springback is more severe for aluminum alloys than steel alloys of similar strength because aluminum alloys have an elastic moduli that is one third that of steel. In general, there are two "standard" strategies to prevent springback: 1)

increasing sheet tension to reduce internal bending moment and 2) compensating by over-specifying the bend angle [55]. There are numerous studies in the past that attempted to determine the controlling factors for springback and methods to reduce springback. An early study by Baba *et al.* [56] investigated the effect of time and magnitude of stretching in stretch-forming of a metal sheet. The obtained results showed a reduction in springback with increasing tensile force and the springback was minimized when the sheet was stretched after bending was done. Liu [57] studied the effect of restraining force by forming flanged channels on special equipment that applied the restraining force directly on the sheet with a hydraulic actuator. It was found that increased restraining force decreased angular springback and side wall curl. However, the magnitude of restraining force that could be applied was limited due to onset of fracture of the vertical side walls. The best results were observed when the restraining force was introduced in the middle of a forming cycle rather than from the beginning. This process divides the forming cycle into two distinct stages of drawing and stretching. The key factor for this process was the timing at which the restraining force is applied and the timing was dependent on the mechanical properties of the material. Schmoeckel *et al.* [58] also studied the effect of varying blank holder pressure. The experimental and numerical results both show that a sudden increase in the blank holder pressure at the end of forming cycle decreased the shape deviations greatly. This type of approach has been widely used to remedy springback problems for the past century [59]. The increased sheet tension reduces the stress gradient through the thickness of the sheet hence decreasing the bending moment that causes springback. However, this approach is limited by the formability of the material as high sheet tension can cause fractures. Furthermore, there has been lot of effort to develop die design methods that account for springback. Karafillis *et al.* [60] utilized finite element analysis to obtain the traction distribution in the fully loaded part which is the driving force for springback. Then the same traction distribution was used to perform inverse elastic simulation on the undeformed part to iteratively calculate the optimal die shape. This method was termed the "force descriptor algorithm" and the flowchart can be seen in Figure 11 (b). The results showed that the algorithm was very effective and showed high accuracy compared to conventional experimental trial and error die design procedures. Similarly, Gan *et al.* [61] developed a new die design method termed the "displacement adjustment method (DA)" which is based on an iterative finite element method. The concept of this method is to move the die surface nodes in the opposite direction of springback as seen in Figure 11 (a). DA was tested under different forming simulations in 2D and 3D and the

results were compared with the force descriptor algorithm. Overall, the DA method converged faster and had higher accuracy, but sometimes had oscillations in the iterative solution. Also, the DA method converged for non-symmetric parts that the force descriptor algorithm failed to. It was confirmed experimentally that the DA is an effective method of designing die shapes without traditional trial and error methods. There are also more advanced DA method such as the "smooth displacement adjustment" method developed by Weiher *et al.* [62] and "surface controlled overbending" method developed by Lingbeek *et al.* [63].

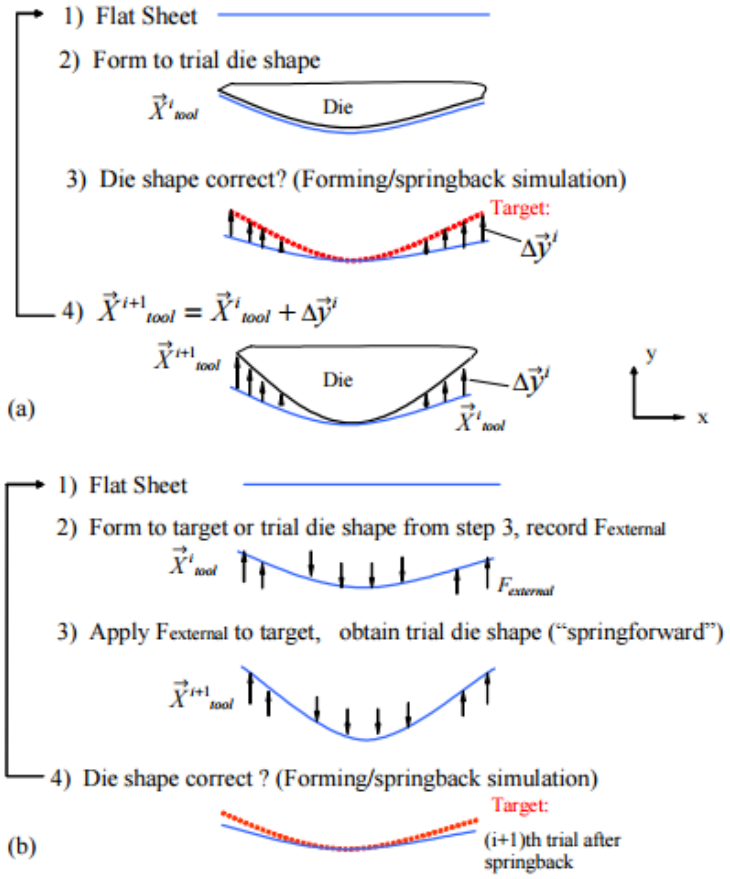

Figure 11: (a) Flowchart of DA method (b) Flowchart of force descriptor algorithm [61]

Although these die design strategies require less rigorous tooling optimizations based on experience and trial-and-error, they are still time-consuming and cost-intensive. An alternative method to reduce springback and the focus of the current thesis is warm forming.

1.3.3 Springback at Elevated Temperatures

There have been numerous studies conducted on warm forming itself but only a limited number of studies has been done on the springback behavior of aluminum alloys at elevated temperatures. Moon *et al.* [64] investigated the effect of tool temperature on the reduction of springback of aluminum 1050 sheet. A non-isothermal u-bend test with punch temperatures of -10^0C and 25^0C and die temperatures of 25^0C, 100^0C, and 200^0C were performed. It was observed that the springback increased with increasing ram speed and the sensitivity to ram speed increased with increasing die temperature. Also, springback was significantly reduced (~20%) with increasing die temperature due to lowered flow stress at elevated temperatures. Yanagimoto *et al.* [65] performed isothermal warm forming of a rail-shape geometry (Figure 12) with AA6061-T4. The tests were performed at a temperature range of 20^0C and 250^0C and it was shown that springback decreased dramatically with increasing temperature up to 60%. Also, isothermal bending was done on the same material which showed similar results.

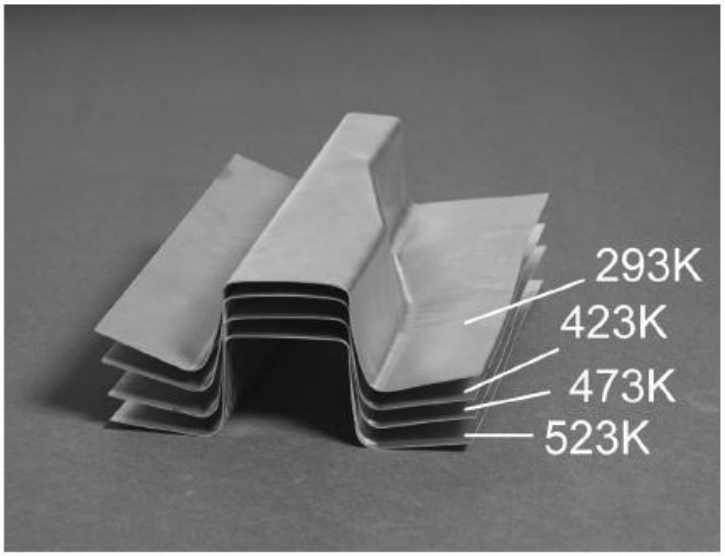

Figure 12: Rail-shape geometries formed at different forming temperatures [65]

Kim *et al.* [66] performed thermo-mechanical finite element simulation of a draw bending process to study the springback characteristics of AA5754-O. The magnitude of springback was greatly reduced at forming temperatures above 200^0C due to decreased material strength at elevated temperatures. It was also observed that increases in blank holder force and friction help in reducing

springback because high sheet tension lowers the through-thickness stress gradient. The punch speed was found to have negative impact on springback above 200^0C due to strain rate sensitivity. Osturk *et al.* [67] investigated the springback behavior of a hardened AA5083-H111 using a 60^0 angle v-bend test at various temperatures ranging from -50 to 300^0C. It was observed that there was no difference in springback for 0, 25 and 100^0C. Springback increased between 100 and 200^0C and then it decreased up to 300^0C. At 300^0C, springback decreased 75% compared to room temperature condition. At -50^0C, springback increased slightly. Also, an increase in frictional force with temperature was seen, thus use of lubricant was recommend at elevated temperatures. Greze *et al.* [68] studied the springback behavior of AA5754-O at elevated temperatures by performing a split-ring test. The split-ring test consists of deep drawing of a cylindrical cup and cutting a ring at a height of 15 mm from the cup bottom. Then the ring is split open by cutting and the opening of the ring is measured to quantify the springback as shown in Figure 13. The drawing operations were performed isothermally. It was determined that the stress gradient in the cup walls decreased with increasing temperature. A springback reduction of 67% was observed when the forming temperature increased from 25^0C to 200^0C. Numerical simulations were performed using an elastic-viscoelastic material model with the von Mises yield surface. The simulations were able to predict the force-displace curves accurately but the springback was over-predicted significantly. Laurent *et al.* [69] performed a similar study in which the cups were formed non-isothermally and split-ring tests were done on AA5754-O sheet. During the forming experiment, the punch temperature was held constant at room temperature and the rest of the tooling were heated up to 100, 150 and 200^0C. The effect of temperature was relatively small for 100 and 150^0C but significant reduction (20.45%) was observed at 200^0C. An isotropic material model with the Hockett-Sherby [70] hardening and power law strain rate dependency was used to simulate the split-ring tests which produced fairly good predictions.

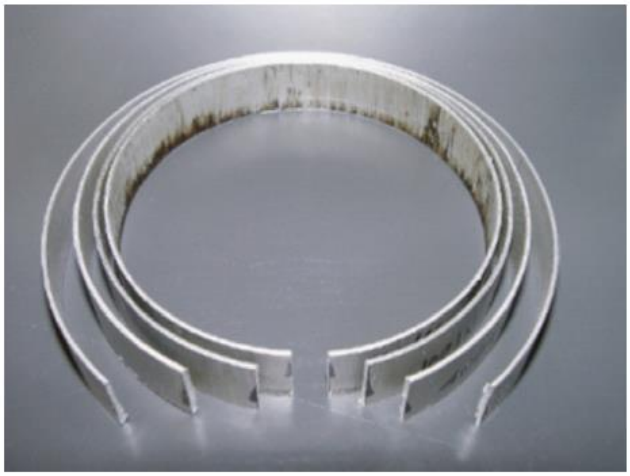

Figure 13: Ring opening at several different temperatures in the range of 25-200^{0}C [68]

Takata [71] conducted hat-shaped bending of AA5182 through warm forming. The results showed that the springback of the hat-shape geometry formed with the aluminum alloy at elevated temperatures was comparable to that of mild steel formed at room temperature. Wang *et al.* [72] characterized the springback behavior of AA5754-H111 through simple bending at elevated temperatures. The springback angle was reduced by 66% when the forming temperature was increased from 20^{0}C to 250^{0}C. It was concluded that the decrease in through-thickness tangential stress gradient led to the reduction in springback. Also, finite element analysis was used to calculate the average through-thickness tangential stress gradient and it was observed that there is a linear relationship between these values and the springback angle. Verma *et al.* [73] studied the springback behavior of AA3003 brazing sheet by warm forming a simple hat channel and found that the reduction in springback (hat channel side wall angular deviation) for three different tempers was in the range of 91-95% when forming at 250^{0}C, compared to room temperature, as shown in Figure 14.

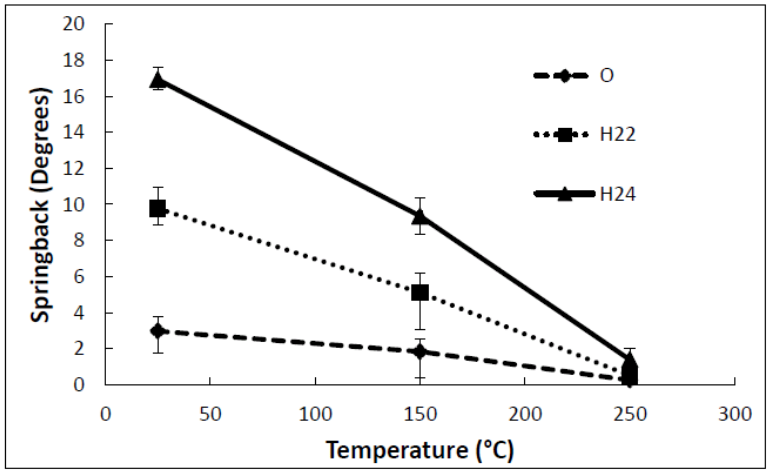

Figure 14: Springback reduction in hat channel side wall of three tempers at elevated temperatures [73]

1.4 Current Work

A considerable amount of work has been reported in the literature to study the formability and springback behavior of aluminum alloys at room temperature. However, the number of studies regarding these topics at elevated temperature is limited, especially for the springback behavior. Furthermore, there have been very few studies conducted on AA3XXX brazing sheet at elevated temperatures, the focus of current research, to investigate the formability and springback characteristics. In addition, the majority of previous studies were done using simple geometries such as u-channels or cup draws in controlled laboratory experiments. Therefore, the objective of this study is to characterize the effects of warm forming at a component-level to observe whether the trends are scalable from simple geometries and to evaluate the feasibility of scaling up warm forming technology to real-life production.

The focus of this research is on an aluminum brazing sheet with an AA3003 core alloy and an AA4045 clad alloy with a proprietary braze promoting coating on the surface, provided by Dana Canada. The sheet was studied in the O-, H22- and H24-temper conditions. The current work investigates the effect of warm forming on formability and springback of 0.2 mm thick aluminum brazing sheet by forming complex parts with specially designed features that simulate vehicle battery cooling plates as opposed to the simple hat channels studied by Verma *et al.* [73].

Currently, some material formability and springback challenges are encountered during the manufacture of battery cooling plates. However, it is evident that warm forming has great potential as a method to dramatically reduce springback and increase formability from previous studies [33], [35], [41]–[43], [73]. If successful, this advanced manufacturing technology will enable to use of harder aluminum brazing sheets with improved handling characteristics and strength. The harder tempers may also exhibit improved corrosion resistance due to their resulting post-braze microstructure [74]. Hence, the warm forming technology could significantly contribute to the manufacture of next generation automotive heat exchangers with improved performance, durability and cost.

The remainder of this thesis is structured as follows. Chapter 2 introduces the material and the component to be studied in this work. It also describes the experimental set-up and different tooling configurations used in the forming experiment. Chapter 3 describes the material modelling effort and set-up for the forming numerical simulations. Chapter 4 deals with the formability challenges associated with forming a complex part with aggressive geometries that are found in actual battery cooling plates. It presents the tooling configuration development process and the forming experiment results. Chapter 5 details the springback characterization of the component and investigates the effects of numerous experimental parameters. The springback simulation set-up is described in Chapter 6 and the predictions are compared to the experimental results. Chapter 7 draws conclusions and makes recommendations for future work.

2 Experiments

2.1 Materials

The brazing sheet considered in the current research is a multi-layer aluminum composite structure that consists of an AA3003 core and approximately 10% AA4045 clad on one side. The surface of the clad layer is coated with Dana Canada's proprietary Ni-based brazing promotor. The AA3003 core is a high manganese content aluminum alloy in which manganese is added for solid solution strengthening. The AA4045 alloy is an Al-Si hypo-eutectic alloy with a lower melting temperature than the core alloy. The typical chemical composition of each alloy is summarized in Table 1. The purpose of the core alloy is to provide structural strength and the clad layer serves as a filler metal in the brazing process. A cross section of the brazing sheet is shown in Figure 15. The transition from the clad to the core can be easily identified by the presence of Si nodules in the clad [74].

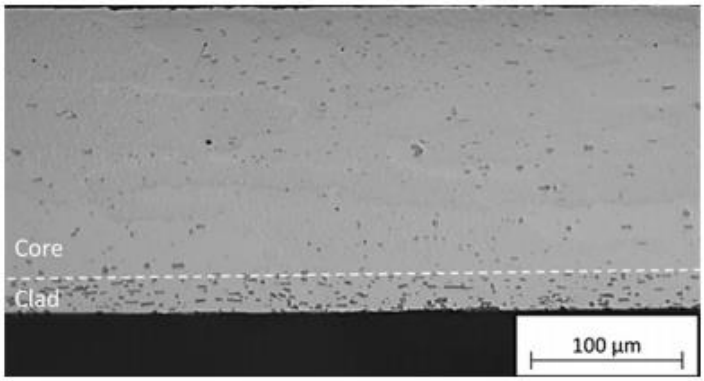

Figure 15: Cross section of a typical AA3003 core and AA4045 clad brazing sheet [74]

The three temper conditions studied are O-, H22- and H24-tempers. The O-temper is the fully annealed condition while H22- and H24-temper conditions are strain hardened and partially annealed to 25% and 50% of the full hardness respectively. The sheet is quite thin at 0.2 mm which

contrasts with previous studies that considered the same sheet material but with a thicker gauge (0.5 mm) and dual-sided clad layers [33], [35], [36], [41], [42] used in engine heat exchangers.

Table 1: Chemical composition in wt.% of Al alloys used in the brazing sheet (bal. Al) [75]

Alloy	Si	Fe	Cu	Mn	Others
AA3003	0.18	0.33	0.64	0.86	≤0.08
AA4045	9.19	0.10	0.11	-	≤0.08

2.2 Material Characterization

The material considered in this study was characterized by Verma *et al.* [73] through tensile tests at elevated temperatures for the O-, H22- and H24-temper conditions. The tests were performed at temperatures of 25^0C, 150^0C, 200^0C and 250^0C and strain rates of 0.002 s^{-1} and 0.02 s^{-1}, along the rolling, transverse and diagonal directions. The tests were conducted on an Instron universal test machine located at the CanmetMATERIALS facility. The lateral and axial strain measurements were obtained using a MTS biaxial video extensometer. The tensile geometry used is shown in Figure 16. The test specimens were cut with EDM instead of CNC machining or jet cutting as it provided the best edge quality results, as required for tensile testing of such thin gauge material.

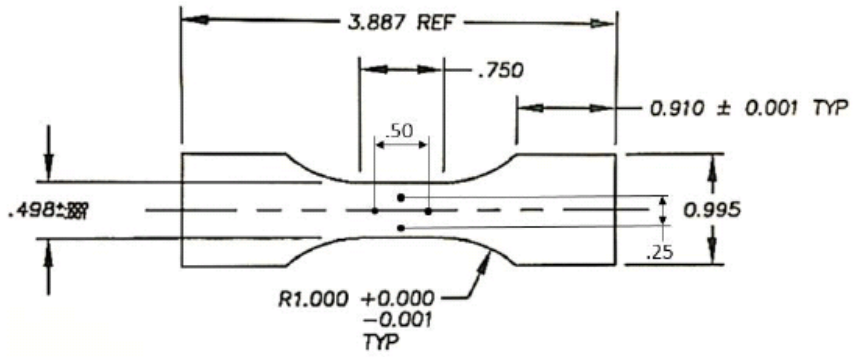

Figure 16: Tensile geometry with dimensions in inches

The effect of material temper at room temperature is shown in Figure 17. The difference in strength between the tempers is evident, with harder tempers having higher strength. The yield strength of H22 and H24 are 163% and 272% greater than that of O-temper respectively. A higher level of strain hardening is observed in the O-temper as the H22 and H24 are already strain hardened

materials. Also, the O-temper sheet exhibited the highest elongation while H22 showed the lowest ductility.

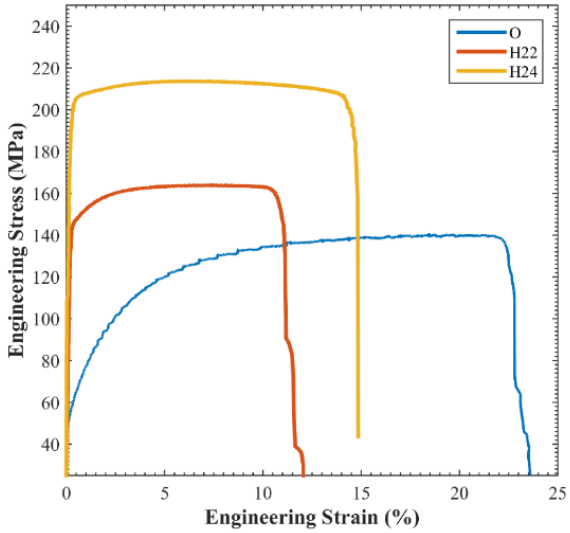

Figure 17: Engineering stress-strain curves for O-, H22- and H24-tempers at room temperature at 0.02 /s. Measured data due to Verma [73]

Figure 18, Figure 19, and Figure 20 show the effect of temperature and strain rate on the tensile behavior of the O-, H22- and H24-temper sheet, respectively. Overall, all three tempers exhibited a similar behavior in that the total elongations increased and strength decreased at elevated temperatures.

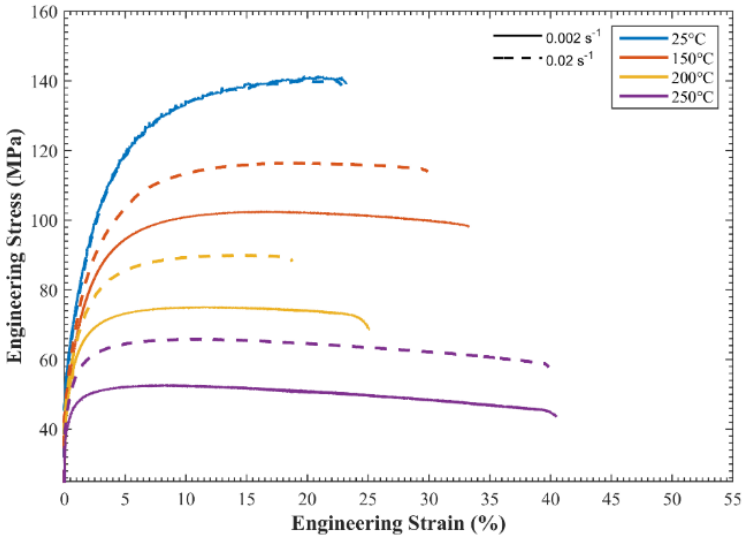

Figure 18: Engineering stress-strain curves of O-temper at different temperatures and strain rates. Measured data due to Verma [73]

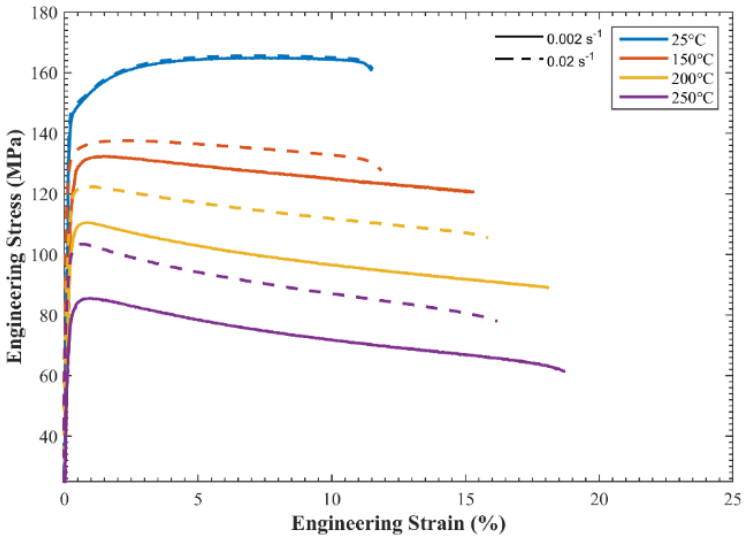

Figure 19: Engineering stress-strain curves of H22-temper at different temperatures and strain rates. Measured data due to Verma [73]

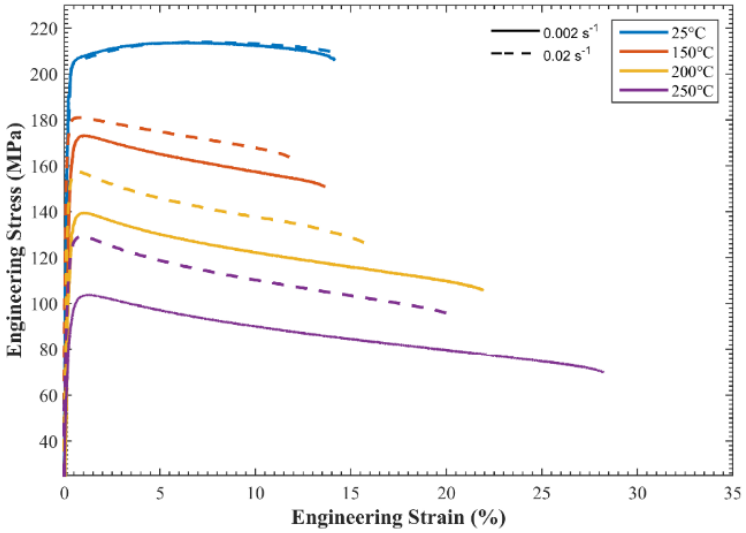

Figure 20: Engineering stress-strain curves of H24-temper at different temperatures and strain rates. Measured data due to Verma [73]

Verma [73] reported that the degree of strain hardening decreased with temperature for all temper conditions. The harder temper materials even exhibited negative hardening behavior at elevated temperatures since the degree of strain hardening was very low to begin with at room temperature. At elevated temperatures, both H22 and H24 reached the ultimate tensile strength immediately after yielding and entered the diffuse necking regime with very little strain hardening. The strain rate sensitivity increased as temperature increased. At room temperature, the strain rate effect was

negligible but higher strain rates lead to increased stress levels at elevated temperatures indicating a positive strain rate sensitivity. The experimental results in different material directions showed a similar behavior which indicates a low level of in-plane anisotropy. Due to the limitation in the tensile experimental set-up, reliable Lankford coefficients (R-values) could not be determined. Future tensile tests should be performed with more advanced strain measurement such as digital image correlation system rather than a video extensometer to accurately capture the anisotropy behavior.

2.3 Component Geometry

As reviewed in Chapter 1, most of the formability and springback characterizations reported in the literature utilized simplified geometries such as u-channels. These geometries are preferred for the ease of experimental design/set-up and obtaining measurement data. Furthermore, the existing literature contains numerous similar studies with experimental results and procedures that could be referred to and compared against. For example, Verma [73] selected a u-shape that was an approximation of the battery plate channel cross-section and contains sufficient bending strain to promote a measurable degree of springback. Although these geometries are easier to use in laboratory studies, there is a possibility that such results are not fully representative of industrial heat exchanger components. Hence, a more representative surrogate heat-exchanger component (hereafter referred as the SHC) was developed, as shown in Figure 21.

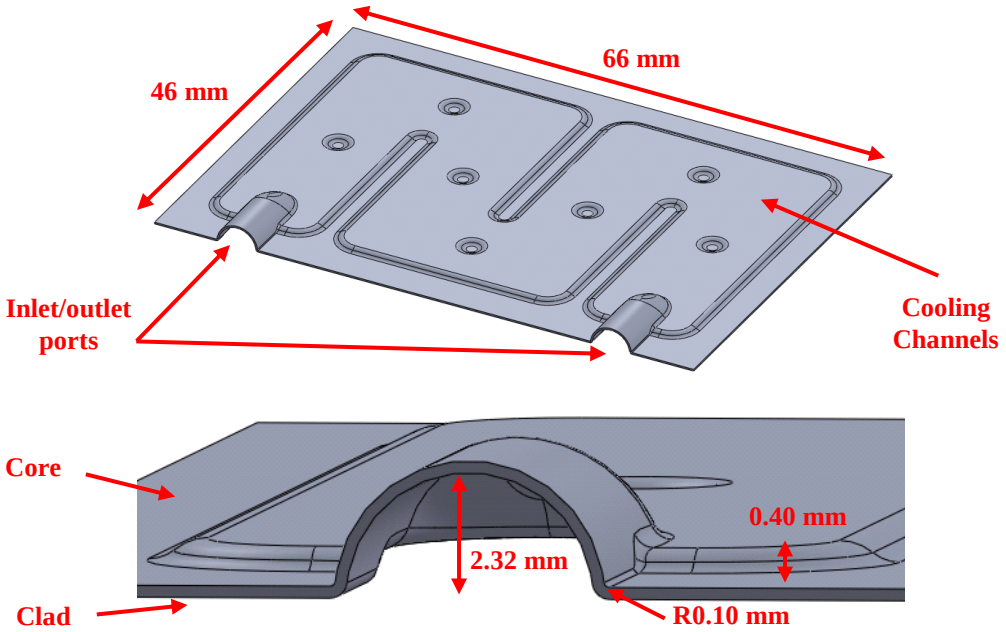

Figure 21: Surrogate heat-exchanger component (SHC)

The developed part contains key features of an actual full-scale battery plate such as the cooling channels and inlet and outlet (I/O) ports; however, the plate contains fewer, channels that are smaller in length than a commercial battery plate such as that shown in Figure 1. On the SHC, the core side is located at the top surface while the clad side is on the bottom surface (brazing surface). Also, the SHC is formed with the rolling direction of the sheet aligned with the length of the component. The purpose of the study of the SHC reported in this thesis is to assess the potential benefit in terms of improved formability and reduced springback using a warm forming process at a component level without the need to manufacture a full-scale warm-formed battery plate. The SHC is also symmetric which enables brazing studies using a single tooling set and subsequent durability testing to examine the effects of warm forming on brazeability and corrosion resistance (as part of related work outside of this thesis).

2.4 Experimental Set-up

The developed SHC was formed using a custom tooling assembly, developed as part of this research, mounted within an Instron 1331 mechanical testing apparatus (Figure 22). During the forming cycle, the punch remained stationary and the die moved upwards. The hydraulic frame is equipped with a load cell and has a force capacity of 100kN which was more than sufficient to

form the SHC. The Instron frame allowed for precise control of the displacement and load acting on the bottom die set which was crucial for the extremely thin gauge material used in the current work.

Figure 22: Custom tooling assembly on the Instron frame

The CAD of the assembly is shown in Figure 23. The alignment of the tooling assembly is guided by a four-post ball bearing die set. Other components included in the assembly are the forming dies, heating/cooling blocks and insulation blocks. The forming dies are heated using eight 200W cartridge heaters, with thermocouples providing feedback to a temperature controller. The cartridge heaters are embedded in separate heating blocks rather than the forming dies themselves to allow for easy interchangeability of the forming dies. The blanks are pre-heated in the forming dies prior to forming via thermal conduction. In order to isolate the heat from the load cell, insulation blocks and chilled water cooling blocks were utilized. The insulation block is made out of ZIRCAL-95, a high density calcium silicate hydrate mix that can withstand temperatures up to 1000^0C and compressive stress up to 450 MPa. The thermal conductivity of this material is 0.31 and 0.27 W/m·K at 200 and 400^0C respectively [76]. The chilled water was supplied at 10^0C.

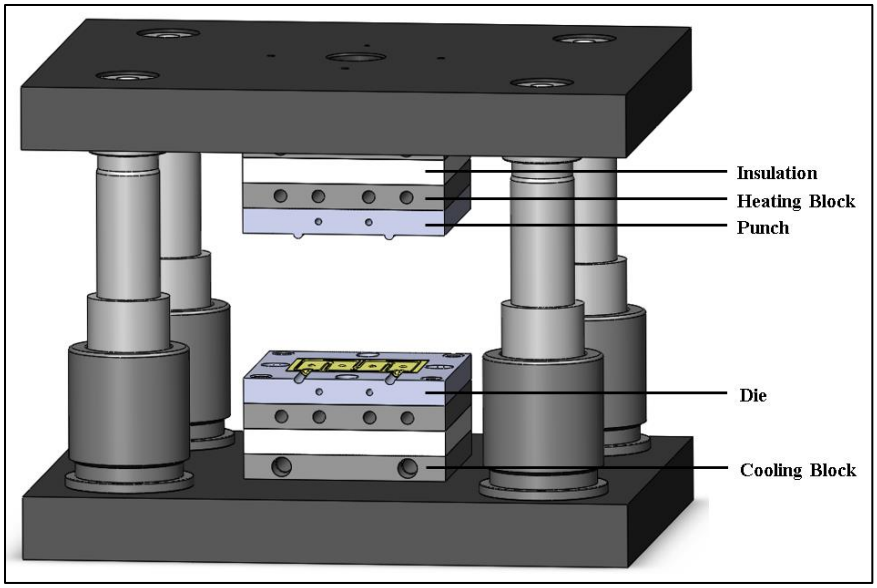

Figure 23: CAD of the custom tooling assembly. SHC shown in yellow.

The most important process parameter was the blank temperature since this work aims to study the effect of warm forming on formability and springback. Other parameters considered are material temper, lubrication, forming speed, punch load and sheet direction.

2.4.1 Tooling Configurations

The forming experiments considered a succession of four different tooling configurations, developed over the course of this research, that consider different die and blank geometries and forming methods. The different tooling configurations will be hereinafter referred as TC1 to TC4. CAD drawings of the different tooling configuration (TC) female dies are shown in Figure 24. The male dies are shown in Section 3.3.

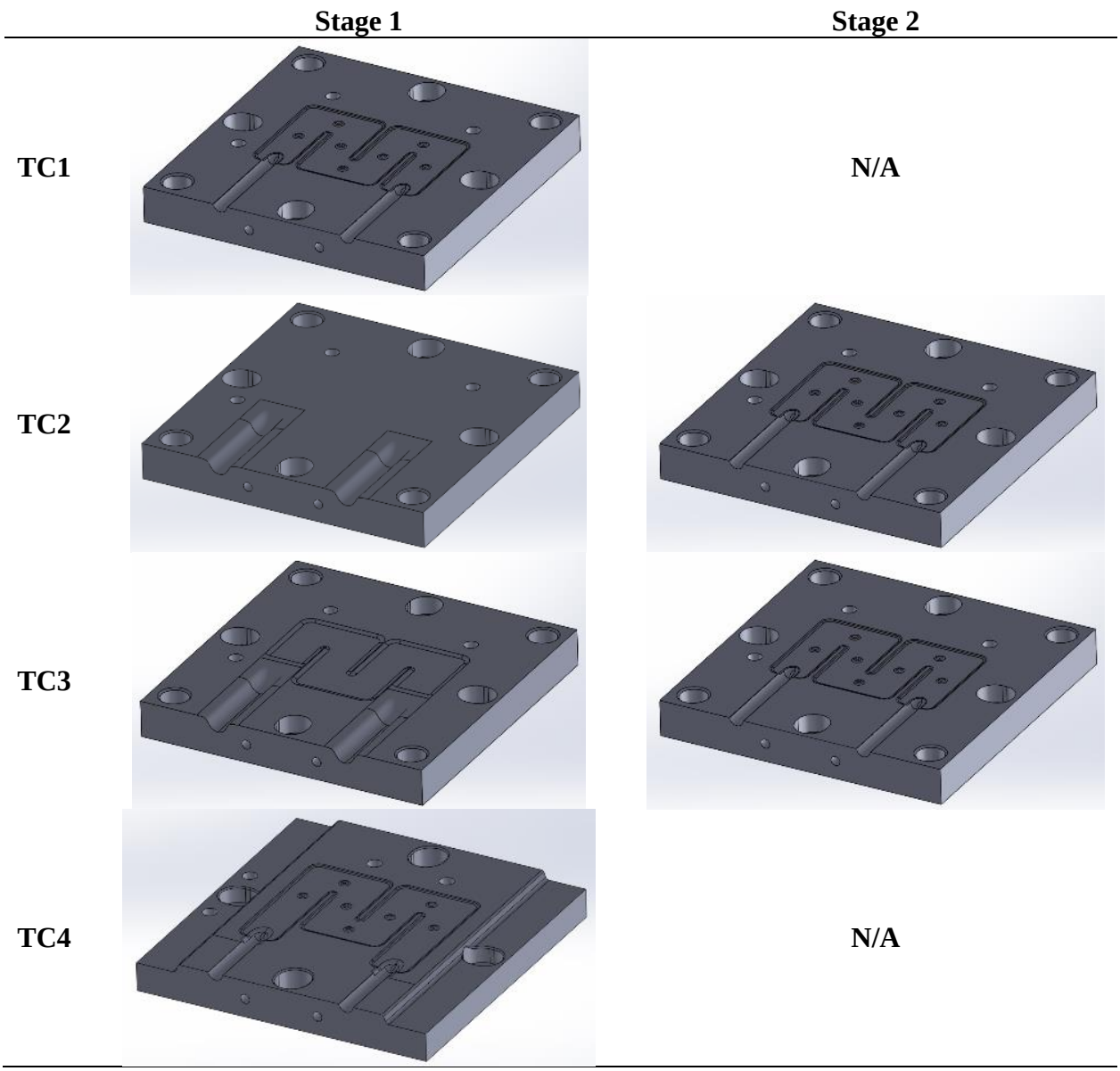

Figure 24: CAD of female dies for the different Tooling Configurations (TC)

The detailed forming process and tooling development are described in Chapter 4. Overall, the forming experiments utilized two different methods. TC1 and TC4 considered a single-stage forming operation in which the final part is formed with a single forming operation without any intermediate forming operations. TC2 and TC3 considered multi-stage forming operations in which the part is formed in two stages. For TC1 to TC3, rectangular blanks were used to form the parts. An office paper trimmer was used to cut rectangular blanks (76.2 mm x 63.5 mm) from the coils since other cutting methods, such as water jet cutting and electrical discharge machining

(EDM), were not necessary for such thin material gauge (0.2 mm). In addition, the paper trimmer was more representative of the shear tool used to produce blanks in commercial fabrication of battery plates. The width of the blank was designed to be longer on one side to test the formability under different material flow conditions (side draw-in) as shown in Figure 25. The material flow for the longer side would be considerably more restricted compared to the shorter side. Dowel pins were used to locate the blank in the tooling prior to forming.

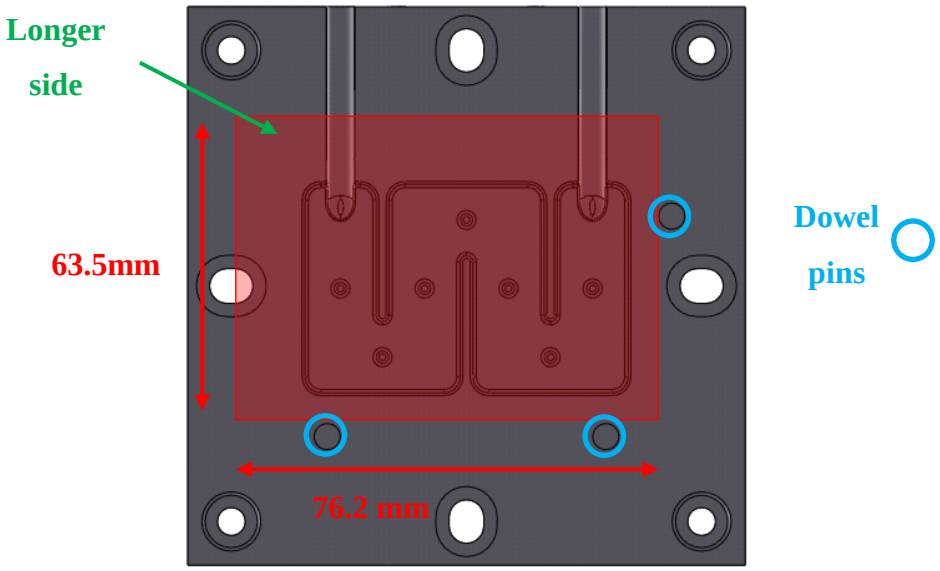

Figure 25: Rectangular blank for TC1 to TC3

For TC4, a "developed blank geometry" was used, as shown in Figure 26. The blank geometry was designed to have optimized material flow. The blank design process is described in Chapter 4.

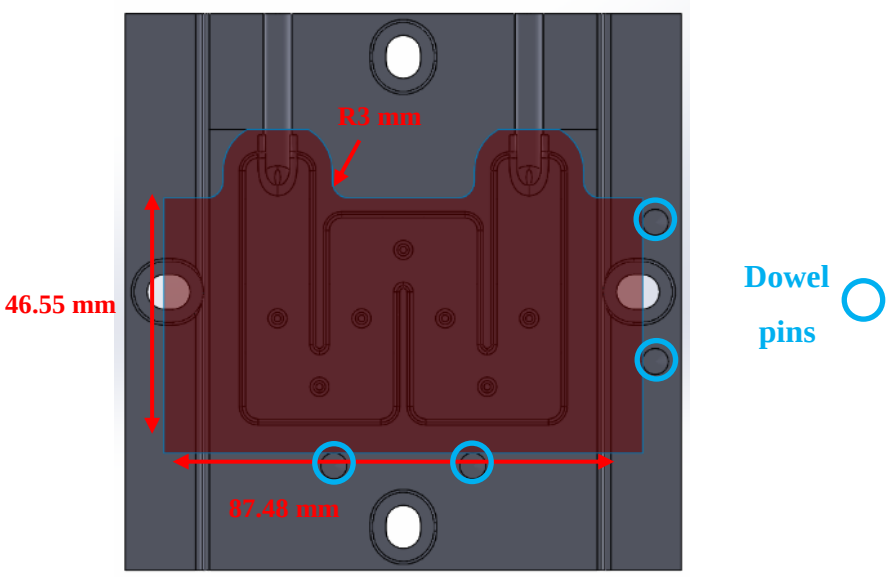

Figure 26: TC4 blank geometry

The rationale behind the development of these different tooling and blank geometries is detailed in Chapter 4 of this thesis; however, the primary factors were wrinkle control and avoidance of necking/fracture. The general sequence of tooling design changes can be summarized as follow:

- Parts formed using TC1 exhibited cracking at the I/O port-cooling channel junction.
- Cracking was somewhat mitigated in TC2 using a pre-form operation (Stage 1) to "gather" material in the I/O port region prior to final forming in the second stage. The part exhibited excessive wrinkling after the first stage which could not be pulled out during the second stage.
- TC3 included the channel geometry in the first stage to reduce wrinkling.
- TC4 introduced geometric modifications to the I/O port-cooling channel intersection to reduce the "sharpness" of the local radii thereby reducing necking/fracture in that region. In addition, a developed blank was used to ease material flow into the I/O port feature while still maintaining a sufficient flange width for brazing. Finally, a "down flange" was added to the sides of the tooling (running parallel to the cooling channels) to restrain the blank during forming and reduce springback.

As noted, these tooling developments are described in detail in Chapter 4.

The geometric features that all tooling configurations share are shown in Figure 27. The locating dowel pins align the top and bottom die sets together and are also used to position the blanks in the tool prior to forming. The dies have slotted bolt holes through the centerline to prevent misalignment due to thermal expansion at elevated temperatures. The slotted holes will allow the dies to expand outwards freely while keeping the axes of the dies, the two datum center lines (shown in red), constant at any temperature. In addition, the die sets were designed with 10% die clearance relative to the sheet thickness. The dies were fabricated through CNC machining using AISI4140 steel. Due to the limited numbers of parts formed, the tools were not hardened nor were they coated.

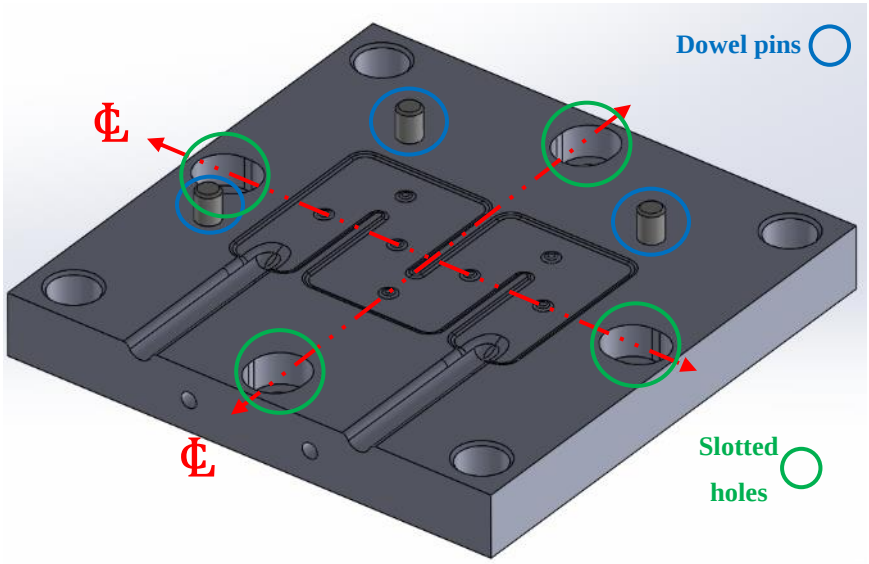

Figure 27: Common geometric tooling features on all tooling configurations

Two lubricants were considered in the experiments, referred to as “Teflon” and “Fuchs”. The Teflon lubricant is a PTFE-based high performance dry lubricant rated for high temperature and pressure applications. The Teflon lubricant is supplied in an aerosol can and was sprayed onto the blank prior to forming. The Fuchs lubricant is Forge Ease Al278 mixed with an alcohol and is specifically designed for warm forming applications. The Fuchs lubricants was applied to the blanks prior to forming using a roller brush. For the forming process with TC1 and TC2, the top die was manually positioned using the hand-held controller of the Instron tensile frame. In order

to make the forming process more robust and reliable, the actuator stroke was changed to displacement-control using a closed-loop system for TC3 and TC4. In order to heat the blank, the heated dies were partially closed initially such that both the top and bottom dies are in contact with the blank surface. After the predetermined heating time of 40 seconds has passed, the top die was displaced further to form the component. This procedure was repeated twice for TC2 and TC3 as the blank formed in the first stage would be subsequently formed in the second stage.

2.4.2 Thermal Validation

In order to ensure that the blanks reached the target temperatures prior to forming, two thermocouples were attached to a test blank in two different locations to record the temperature history during the heating cycle. The first location was at the middle of the blank and the second location was at the input/output port (I/O port), as seen in Figure 28. A data acquisition system was used to record the temperature history (Figure 29) from which it was determined that the blank successfully reached the target temperatures within 40 seconds; thus, the heating time prior to forming was selected to be 40 seconds.

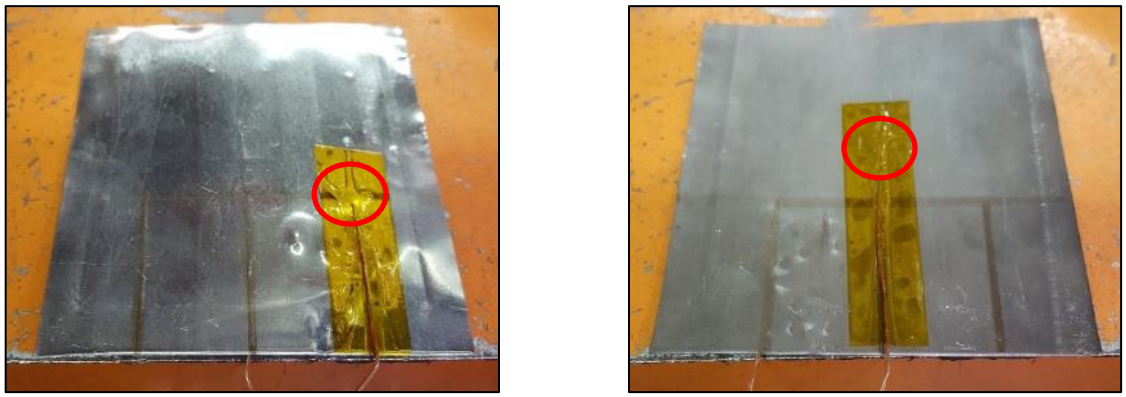

(a) **(b)**

Figure 28: Thermocouple at the (a) I/O port (b) middle of the blank

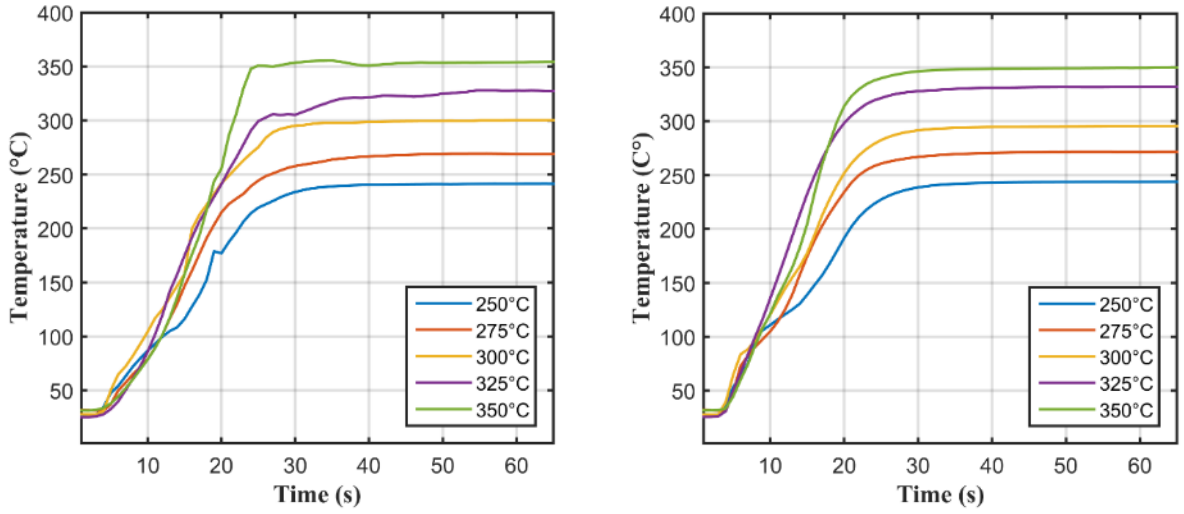

Figure 29: Temperature history at the (a) I/O port (b) middle of the blank. The target temperatures are indicated in the legend.

2.4.3 Micro-hardness Tests

One of the major concerns related to warm forming is recrystallization caused by elevated forming temperatures. Vickers hardness tests were performed to determine if there was indeed any recrystallization and adverse effects on the strength of the material. Sample blanks were heated to temperatures ranging from 25 to 350°C and cold mounted into pucks made of epoxy resin. The pucks were cold mounted since the hot mounting technique exposes the specimens to elevated temperature and pressure, which could potentially affect the results. The pucks were ground and polished using SiC abrasive papers with grit values ranging from 220 to 2400. A Wilson 402MVD hardness tester was used which has a built-in microscope that allows users to view the actual diamond indent and measure the diagonals. The indents were made on the material thickness with 100 gf and the force was applied for 15 seconds. The minimum spacing between indentations was greater than 2.5 times the indent diagonal [77] to separate the strain hardening effect of prior indents. The results are summarized in Figure 30. Each sample was indented seven times and the error bars correspond to the standard deviations. The test results show that there was no significant decrease in the hardness with the increasing heating temperatures.

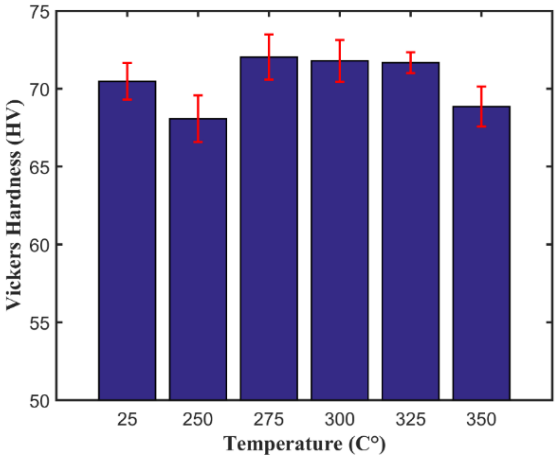

Figure 30: Vickers hardness results after heating cycle at different temperatures

2.5 Friction Characterization

Friction is one of the most important process parameters in metal forming; thus it must be characterized experimentally to produce accurate numerical simulations. In the current work, two lubricants were considered initially: Teflon and Fuchs. However, the Fuchs lubricant was omitted from the friction characterization as it had negligible performance difference from the Teflon spray which had cleaner surface quality and superior application method. According to work done by Noder [78], the COF for Teflon and Fuchs were comparable up to 20 mm sliding distance which is significantly higher than the sliding distances in the current work. The coefficient of friction (COF) of the Teflon lubricant was determined using the Twist Compression Test (TCT) apparatus shown in Figure 31.

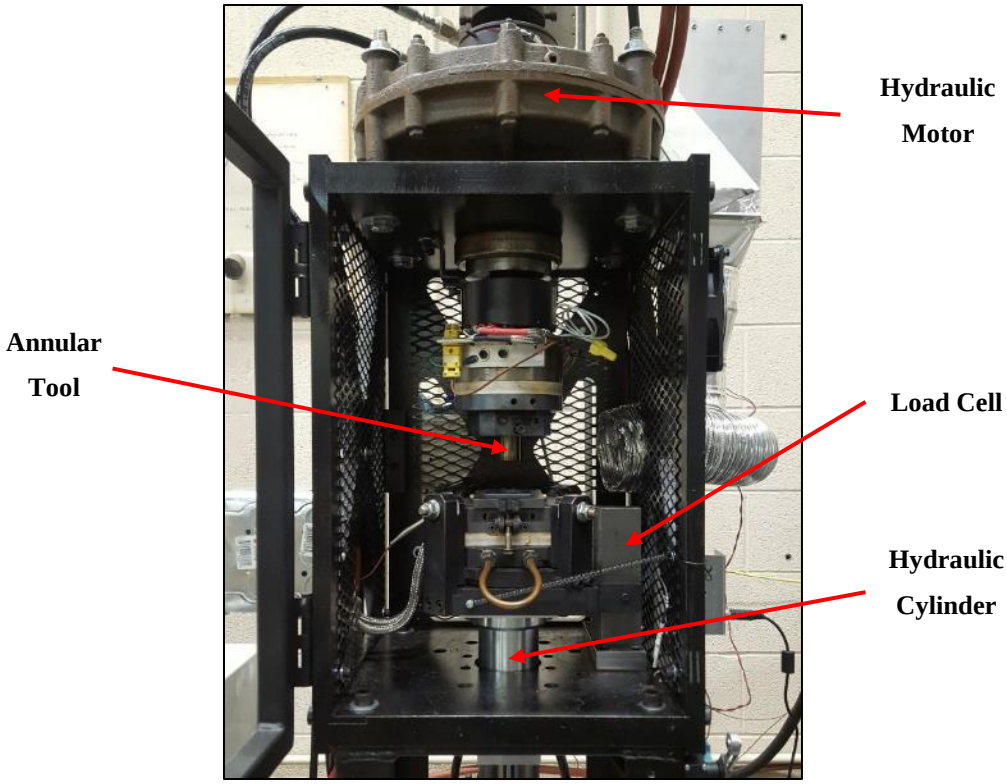

Figure 31: Twist compression test (TCT) apparatus

The TCT is a tribological test developed by Schey [79] that can closely simulate actual metal forming conditions, such as interfacial pressure and sliding speed. It uses an annular tool which is pressed against a fixed sheet specimen at a specified pressure and then rotated. A load cell is used to measure the torque transmitted by the frictional force. The coefficient of friction is calculated with the following formula:

$$COF = \frac{T}{rPA} \tag{1}$$

Where T is the transmitted torque, r is the annular tool mean radius, P is the applied pressure and A is the cross-sectional area of the annular tool.

Recently, the TCT apparatus was upgraded by George [80] to perform testing at elevated temperatures corresponding to conditions during warm forming. A detailed description of the warm friction TCT procedures is provided by Noder *et al.* [78]. This elevated temperature test

capability was employed in the current work to evaluate the lubricant performance under the warm forming conditions considered in the SHC forming experiments. The annular tool material used was AISI 4140 steel which is identical to the tool material used in the forming experiments. The test matrix is summarized in Table 2 below.

Table 2: Twist compression test matrix showing number of specimens tested for each condition.

	Core		Clad	
Temperature	Dry	Teflon	Dry	Teflon
25	3	3	3	3
240	3	3	3	3
310	3	3	3	3

Since the sheet metal has two different surfaces on the core and clad, the TCT was performed on both surfaces using dry and lubricated conditions at 25, 240 and 310°C. The sliding speed was set to be constant at 1 mm/s for all conditions for smooth data acquisition. Due to the very thin gauge of the sheet, the interfacial pressure was set relatively low especially for the elevated temperature conditions otherwise the specimens wrinkled excessively. The interfacial pressure was set at 10, 5, and 1 MPa for temperatures of 25, 240 and 310°C, respectively.

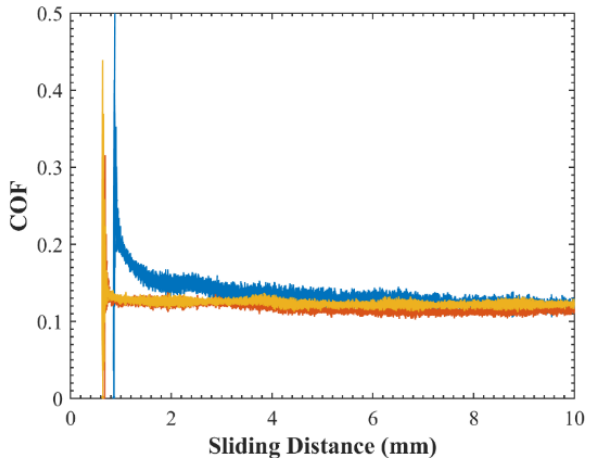

Figure 32: Twist compression test result for clad surface lubricated with Teflon at 25°C

Figure 32 shows the test results for the clad surface lubricated with Teflon at room temperature. The coefficient of friction was obtained by taking the average of the values in the sliding distance

range of 2 to 4 mm for the three repeats. A summary of the TCT experiments is shown in Figure 33.

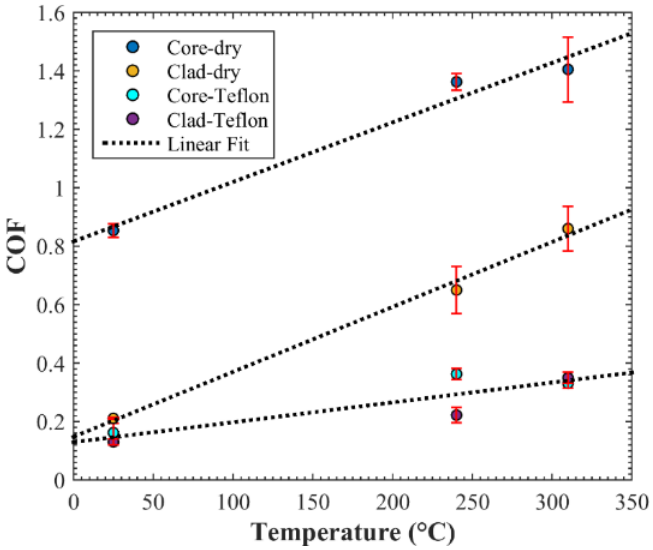

Figure 33: Effect of temperature on COF at dry and lubricated conditions

It was concluded that the COF can be approximated as a linear function of temperature. Also, under dry conditions, the core side had a significantly higher COF compared to the clad side. This difference is attributed to the fact that the clad side is coated with Dana's proprietary Ni-based braze promoter. The exact nature of the coating is proprietary but the coefficient of friction between mild steel and pure Nickel was found to be 0.49 [81]. When the surfaces were lubricated with the Teflon spray, the difference in COF between the core and clad surfaces was no longer observed. Therefore, only a single linear fit was used to represent the COF for lubricated conditions. The equations describing the COF as a function of temperature in °C are as follows:

$$COF_{Core,dry}(T) = 0.002036T + 0.8163 \quad (2)$$

$$COF_{Clad,dry}(T) = 0.002222T + 0.1478 \quad (3)$$

$$COF_{Teflon}(T) = 0.0006803T + 0.1294 \quad (4)$$

3 Numerical Model

3.1 Constitutive Models

In order to accurately model the warm forming process, the effect of temperature and strain rate on flow stress must be considered in the constitutive model used to simulate the mechanical properties of the brazing sheet. As shown previously through the material characterization study by Verma *et al.* [73], the stress-strain curves of the brazing sheet decreased as the temperature increased and as the strain rate decreased. In current work, the material was assumed to be isotropic since the R-values could not be determined; thus, a Von Mises yield surface was used. Two phenomenological hardening models, referred to as the Voce hardening [82] and Extended Nadai models [83], were considered as potential candidates to describe the hardening behavior. These models will be validated by performing tensile simulations in the next section.

3.1.1 Voce Hardening Model

The Voce hardening model is a widely used phenomenological model developed by Voce [82] which accounts for the flow stress saturation hardening behavior exhibited by aluminum alloys. The original Voce model was not a function of temperature and strain rate. Therefore, the strain rate effect was incorporated by including a logarithmic strain rate term. The temperature effect was accounted by fitting the model at each temperature condition since the temperature stays constant during each forming experiment. The Voce hardening model is as follows:

$$\sigma = \left(\sigma_{sat} + \left(\sigma_y + \sigma_{sat}\right)e^{\left(\frac{\varepsilon_p}{\varepsilon_c}\right)}\right)\left(1 + A\log\left(\frac{\dot{\varepsilon}}{\dot{\varepsilon_0}}\right)\right) \quad (5)$$

Where, σ_{sat} is the saturation stress, σ_y is the yield stress, ε_c is the strain constant controlling the rate of saturation, ε_p is the plastic strain, A is the strain rate parameter, $\dot{\varepsilon}$ is the strain rate and $\dot{\varepsilon_0}$

is the reference strain rate. The experimental tensile stress-strain curves were used to obtain the model parameters through non-linear regression using MATLAB for two temperature conditions of 25°C and 250°C. The model parameters are listed in Table 3.

Table 3: Voce hardening model parameters

Material Temper	Temperature (°C)	σ_{sat} (MPa)	σ_y (MPa)	ε_c	A	$\dot{\varepsilon_0}$ (s^{-1})
O	25	168.9	65.9	17.8	-0.00388	0.002
O	250	57.3	43.03	40.4	0.236	0.002
H22	25	178.3	151.7	36.8	0.000503	0.002
H22	250	86.4	82.3	585.4	0.223	0.002
H24	25	237.9	206.2	17.3	0	0.002
H24	250	106.6	103.6	404.7	0.233	0.002

The extrapolated flow stress curves (true stress versus effective plastic strain) for the three tempers are plotted against the experimental tensile data up in Figure 34 through Figure 39. The measured data is shown to ultimate tensile strength since necking occurs after this point and the stress state is no longer uniaxial.

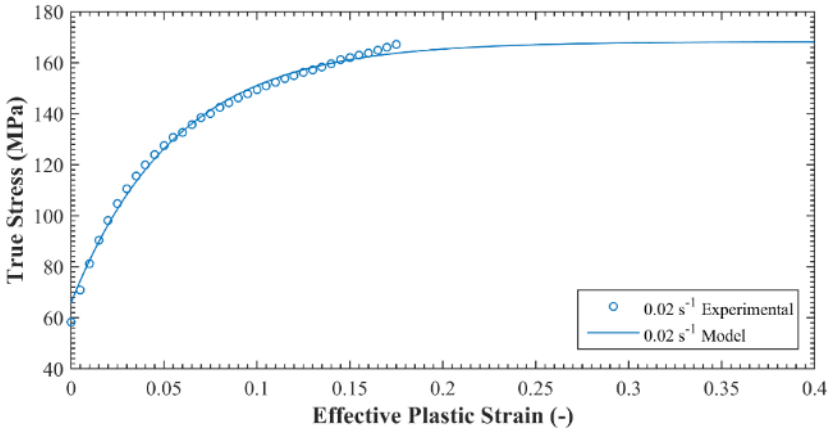

Figure 34: Voce hardening model for O-temper at 25°C. Measured data due to Verma [73]

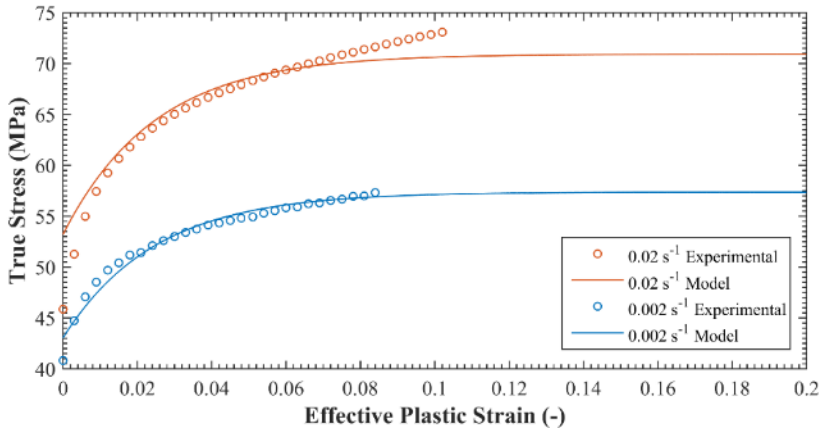

Figure 35: Voce hardening model for O-temper at 250°C. Measured data due to Verma [73]

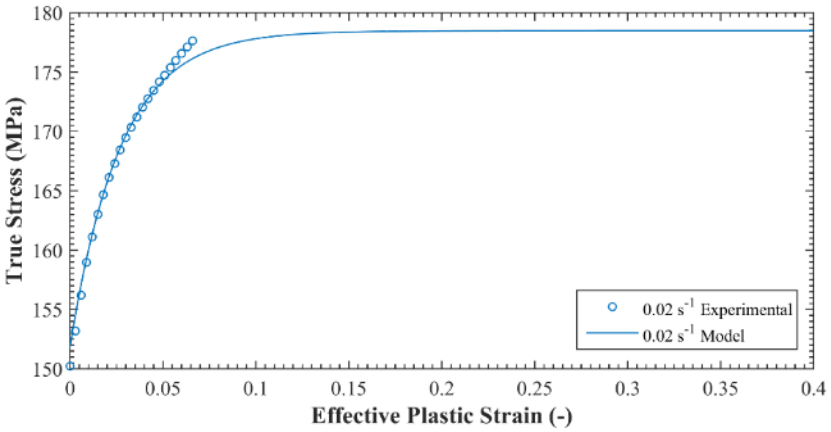

Figure 36: Voce hardening model for H22-temper at 25°C. Measured data due to Verma [73]

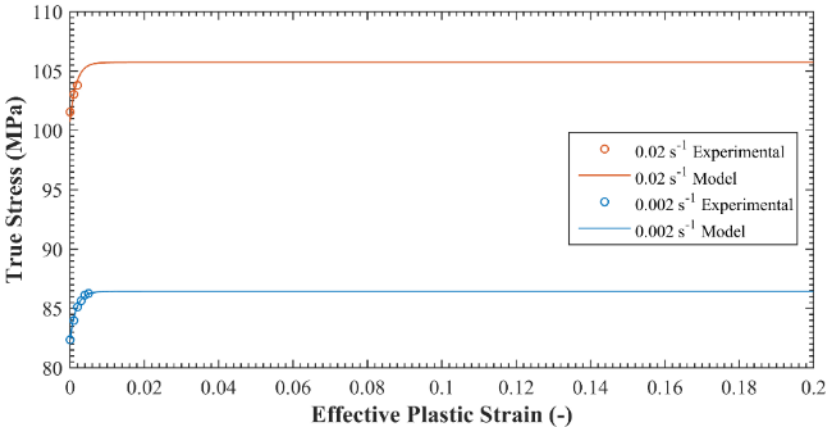

Figure 37: Voce hardening model for H22-temper at 250°C. Measured data due to Verma [73]

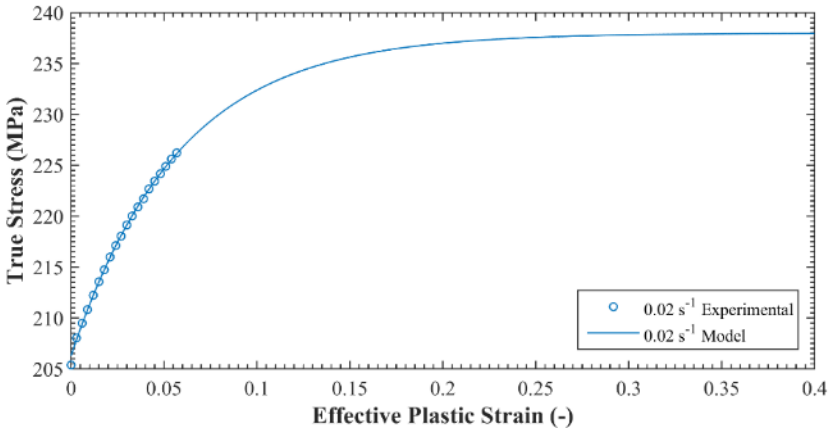

Figure 38: Voce hardening model for H24-temper at 25^{o}C. Measured data due to Verma [73]

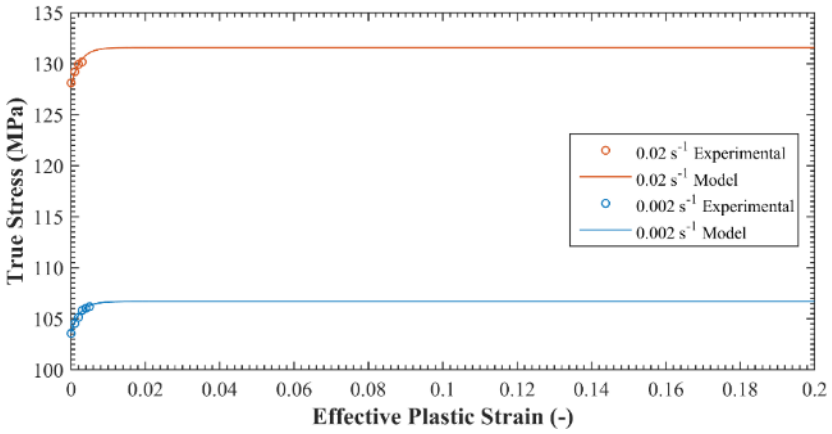

Figure 39: Voce hardening model for H24-temper at 250^{o}C. Measured data due to Verma [73]

The Voce hardening model captured the initial hardening and saturation behavior relatively well for all three tempers at room temperature condition. However, the harder tempers at 250^{o}C displayed only a very small amount of hardening prior to ultimate tensile strength which limited the range of data used in the non-linear regression. This could potentially produce inaccurate flow behavior which will be assessed in Section 3.2 through comparison between tensile simulations using the constitutive fits to the measured tensile data.

3.1.2 Extended Nadai Model

Another model considered in the numerical simulations is the very well-known phenomenological model based on the Nadai hardening law with strain rate and temperature effects [83].

$$\sigma = C(\varepsilon_p + \varepsilon_0)^n \left(\frac{\dot{\varepsilon}}{\dot{\varepsilon}_0}\right)^m \tag{6}$$

For the extended Nadai model, parameters C, n and m are functions of absolute temperature as follows:

$$C(T) = C_0 + a_1 \left[1 - \exp(a_2 \frac{T - 273}{T_m})\right] \tag{7}$$

$$n(T) = n_0 + b_1 \left[1 - \exp(b_2 \frac{T - 273}{T_m})\right] \tag{8}$$

$$m(T) = m_0 \exp(c \frac{T - 273}{T_m}) \tag{9}$$

Where $\dot{\varepsilon}_0$ is the reference strain rate and T_m is the melting temperature in Kelvin. The rest of the parameters are identified by performing non-linear regression on the experimental data. The model was slightly modified as the power law strain rate dependency resulted in non-physical and extremely high flow behavior for higher strain rate conditions. Therefore, the strain rate term was replaced with a logarithmic strain rate term with temperature dependence as shown below:

$$\sigma = C(\varepsilon_p + \varepsilon_0)^n \left(1 + B \log\left(\frac{\dot{\varepsilon}}{\dot{\varepsilon}_0}\right)\right) \tag{10}$$

$$B(T) = B_0 + c_1 \left[1 - \exp(c_2 \frac{T - 273}{T_m})\right] \tag{11}$$

The following Table 4 to Table 6 contain the model parameters obtained through non-linear regression in MATLAB by simultaneously fitting different strain rate and temperature conditions for the three tempers.

Table 4: Extended Nadai Model parameters for O-temper

$T_m\ (K)$	800	a_1	4751	b_2	-0.717
$\dot{\varepsilon}_0\ (s^{-1})$	0.002	a_2	0.137	B_0	0.000994
ε_0	0.000994	n_0	0.272	c_1	-0.506
$C_0\ (MPa)$	289.4	b_1	-0.843	c_2	1.32

Table 5: Extended Nadai Model parameters for H22-temper

$T_m\ (K)$	800	a_1	-905.1	b_2	-3.110
$\dot{\varepsilon}_0\ (s^{-1})$	0.002	a_2	-0.642	B_0	-0.0287
ε_0	0.0104	n_0	0.105	c_1	448.1
$C_0\ (MPa)$	239.8	b_1	-0.218	c_2	-0.00122

Table 6: Extended Nadai Model parameters for H24-temper

$T_m\ (K)$	800	a_1	-460.5	b_2	-4.76
$\dot{\varepsilon}_0\ (s^{-1})$	0.002	a_2	-2.51	B_0	-0.0171
ε_0	0.0617	n_0	0.1806	c_1	894.4
$C_0\ (MPa)$	335.5	b_1	-0.342	c_2	-0.000735

Conventionally, only the experimental data prior to ultimate tensile strength could be used to obtain the material model parameters as deformation is no longer uniform and diffuse and localized necking occur. At elevated temperatures, aluminum alloys exhibit improved uniformity of strain distribution due to increased positive strain rate sensitivity that prevents localized necking [8,9]. The mechanism behind warm forming, strain rate hardening, strongly delays the onset of localized necking increasing the diffuse necking regime. As shown by the tensile test results, the high temperature specimens immediately entered the diffuse necking regime due to lack of strain hardening at elevated temperatures but localized necking did not occur until a significant amount of strain has accumulated. According to Ghosh [84], a very small amount of strain gradient is maintained in the diffuse necking stage and necking may not be visually apparent until a significant amount of strain has accumulated, thus the deformation is quasi-stable in nature and practically uniform. It was also observed during the tensile test that significant necking did not occur. In diffuse necking, the extension of the neck is often similar to the specimen width [85]. Since the width of the specimen (0.5") is similar to the length of the gauge (0.75"), the majority of the gauge section is in the diffuse necking regime resulting in a small strain gradient within the gauge. Therefore, it was assumed that the tensile data for harder tempers after ultimate tensile strength are practically uniform and data up to 10% strain were used to fit the Extended Nadai Model. The

following Figure 40 to Figure 42 show the flow stress prediction of the Extended Nadai Model for the three tempers at different temperatures and strain rates.

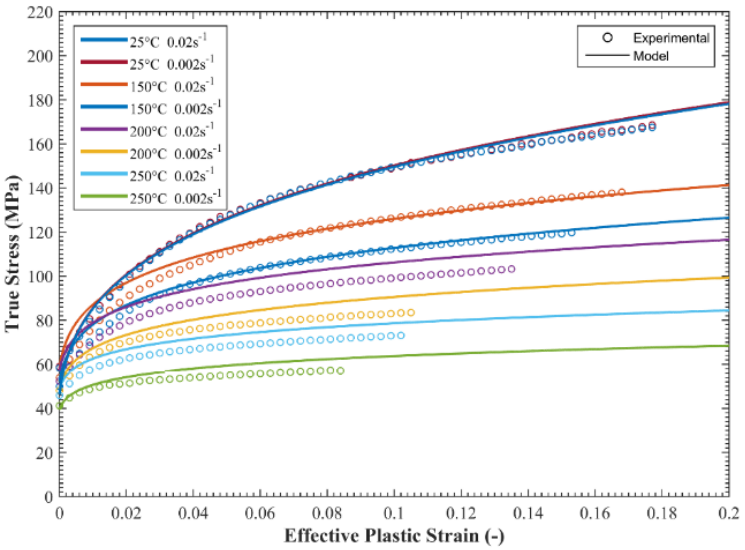

Figure 40: Extended Nadai Model for O-temper at different temperatures and strain rates. Measured data due to Verma [73]

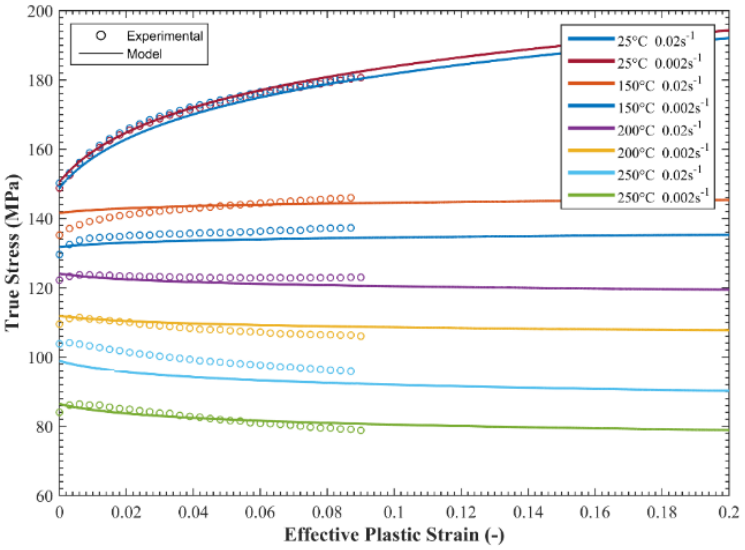

Figure 41: Extended Nadai Model for H22-temper at different temperatures and strain rates. Measured data due to Verma [73]

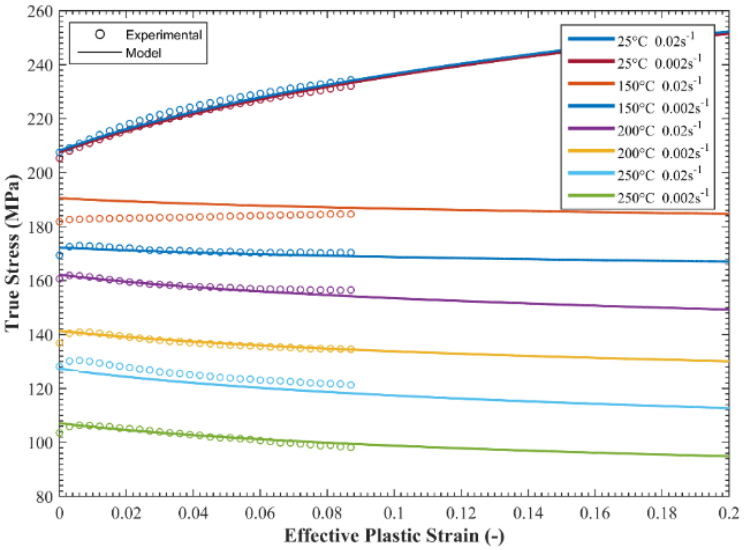

Figure 42: Extended Nadai Model for H24-temper at different temperatures and strain rates. Measured data due to Verma [73]

The model represented the hardening behavior quite well for different temperature and strain rate ranges for all of the tempers. Also, the model was able to capture the negative hardening effect that was observed for harder tempers at elevated temperatures. The largest discrepancy between the experiment and model occurred when the temperature was at 150°C for H22- and H24-tempers as the temperature was an intermediate value at which the transition in hardening behavior from positive to negative occurs.

3.2 Tensile Simulations

In order to validate the material models, tensile simulations were performed and compared with the experimental results of Verma [73].

3.2.1 Tensile Model Set-up

The tensile simulations were performed using the non-linear implicit dynamic formulation within the LS-DYNA [86] commercial finite element code. The tensile specimen used in the characterization experiment was meshed using Type 2 selective reduced integrated solid elements.

The gauge section was meshed with elements with a length of 0.3 mm and four elements were meshed through the thickness. The overall mesh is shown in Figure 43.

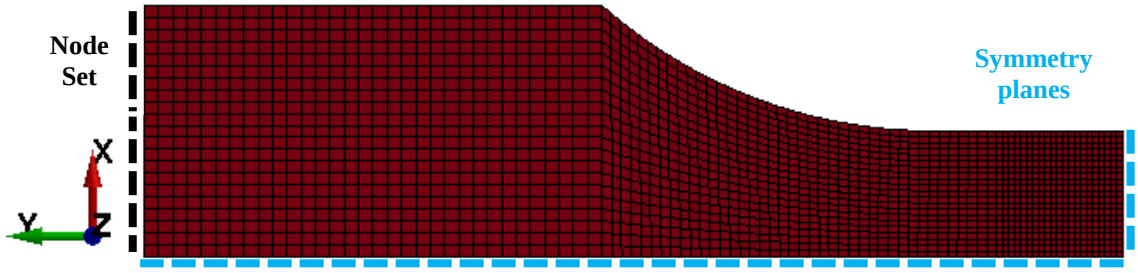

Figure 43: Tensile specimen mesh

Only one-quarter of the model was simulated with symmetry boundary conditions prescribed along the x-z and y-z planes. A velocity boundary condition was imposed on the node set at the gripped end of the specimen (Figure 44) to pull the specimen towards the positive y-direction while the displacement in the other two directions (x and z) were constrained. The tensile load was obtained by summing the nodal reaction forces for the node set. Since LS-DYNA material library does not contain built-in Voce hardening and extended Nadai models, the piecewise linear plasticity material model (*MAT-24) was used for the simulations. This material model is a simple isotropic model that uses von Mises yield criterion and takes an arbitrary stress *versus* strain curves as input. The constitutive hardening behaviors predicted by the Voce hardening and extended Nadai models were simply entered as point-wise stress-strain curves for each strain rate and temperature. The software then performs a linear interpolation between curves to account for local strain rate. The simulations are isothermal, so interpolation based on temperature was not necessary. A typical input set of stress-strain curves for the material model is shown in Figure 45.

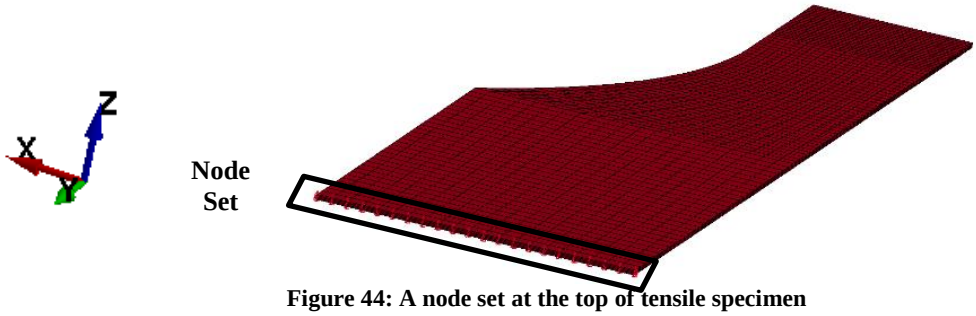

Figure 44: A node set at the top of tensile specimen

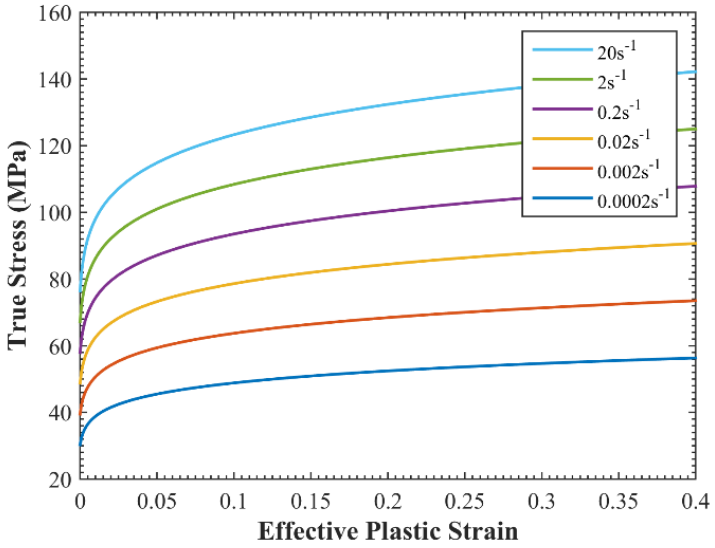

Figure 45: Typical input curves for piecewise linear plasticity model. O-temper behavior predicted with the extended Nadai model at 250°C at different strain rates

The material model accepts a set of true stress *versus* effective plastic strain curves for a range of different strain rates. The hardening behaviors at strain rates outside of the experimental range (0.002 s^{-1} and 0.02 s^{-1}) are captured by extrapolating the material models developed in the previous section. It is important to capture the strain rate effect outside of the experimental range as local strain rates in tensile and metal forming simulations could be outside of the range. The flow stress at intermediate strain rates are evaluated by interpolating between the set of curves. Simulations were performed for each temperature condition in which different sets of stress-strain curves were used as input.

3.2.2 Voce Hardening Model Results

The tensile simulation results for the Voce Hardening Model are summarized in Figure 46, Figure 47 and Figure 48 for the O-, H22- and H24-tempers, respectively.

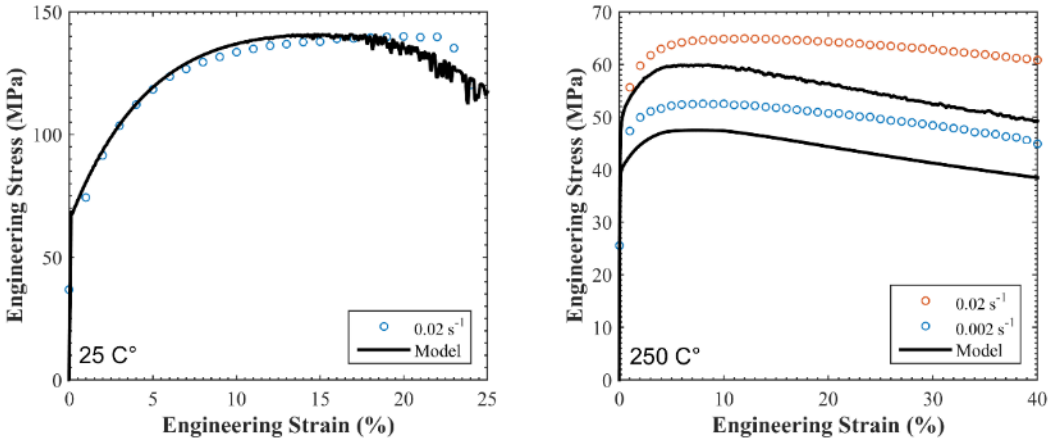

Figure 46: Voce hardening model tensile simulation results for O-temper

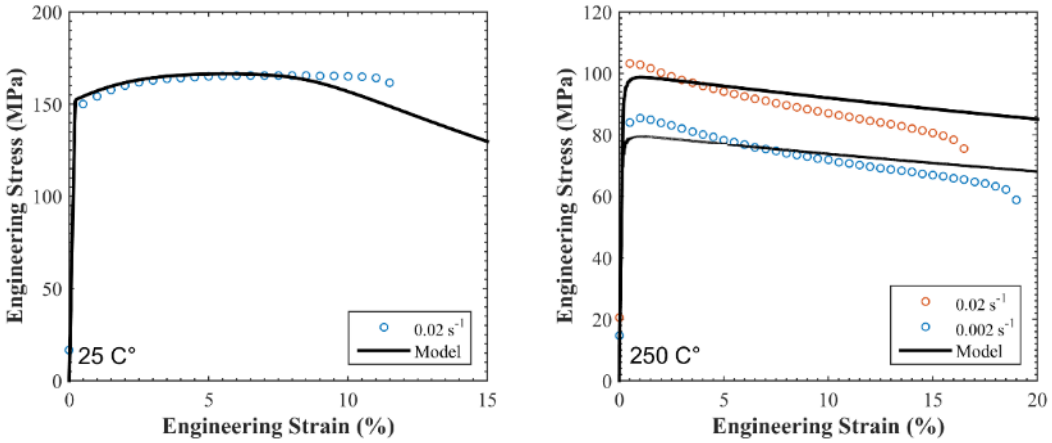

Figure 47: Voce hardening model tensile simulation results for H22-temper

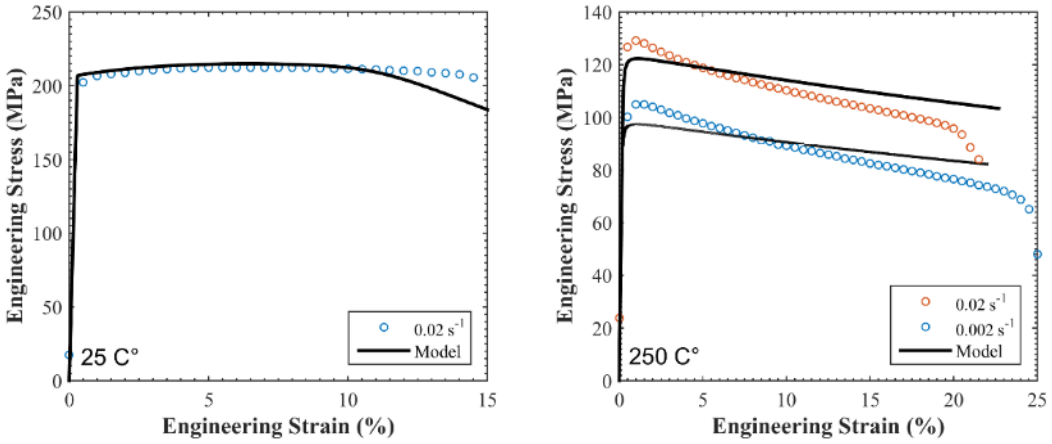

Figure 48: Voce hardening model tensile simulation results for H24-temper

For the O-temper condition, the model under-predicted the experimental results at room temperature. However, the response was greatly under-predicted at elevated temperatures due to the model predicting the flow saturation prematurely.

For the harder temper materials, the response was under-predicted at room temperature but over-predicted at elevated temperature. It was concluded that the flow stress saturation behavior of the model is not adequate to capture the negative hardening behavior of the material. Overall, the model did not predict the tensile response of the experiment accurately for all three tempers.

3.2.3 Extended Nadai Model Results

The stress-strain curves of experimental and simulated tensile tests using the Extended Nadai model are shown in Figure 49 to Figure 51 for the three tempers. The predictions using the Extended Nadai model were able to accurately capture the tensile response of the three tempers at different temperature and strain rate. Also, the model was capable of capturing the negative slope of the stress-strain curves at elevated temperatures. There was still a slight over-prediction in the slope of the hardening response of the harder tempers at 250°C. Figure 52 shows the maximum principal strain of the tensile gauges of H24-temper at 25°C and 250°C at a crosshead displacement of 7mm. The room temperature condition shows shear localization while the elevated temperature condition shows a uniform strain distribution in the majority of the gauge section. This result shows that the model captured the strain rate hardening effect which is the main driving mechanism serving to stabilize the material during warm forming. Overall, the Extended Nadai model performed considerably better than the Voce hardening model thus it was adopted in the subsequent forming and springback simulations.

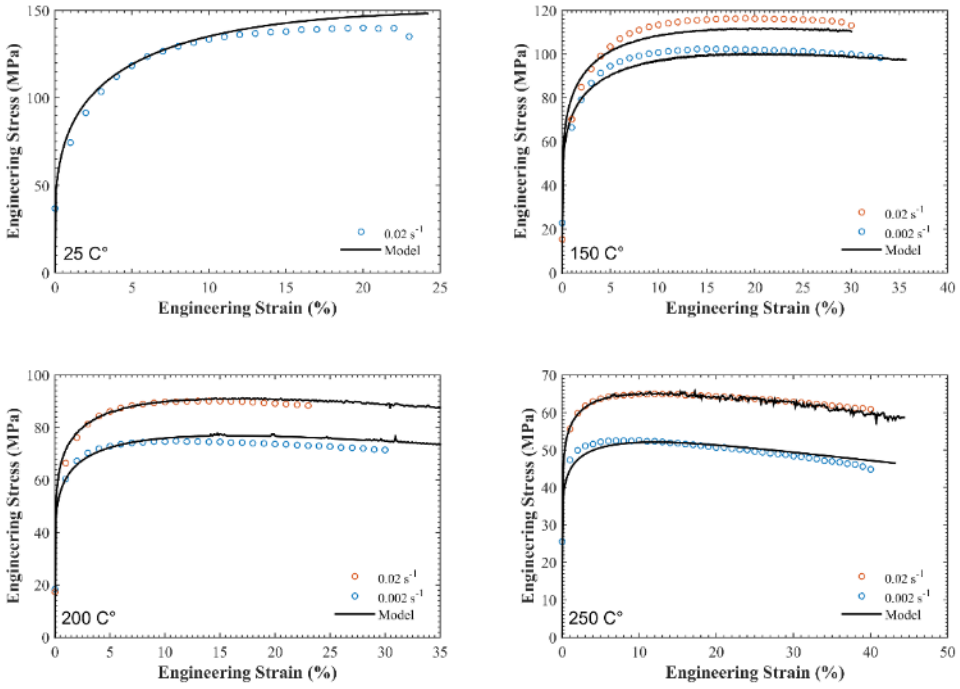

Figure 49: Extended Nadai model tensile simulation results for O-temper

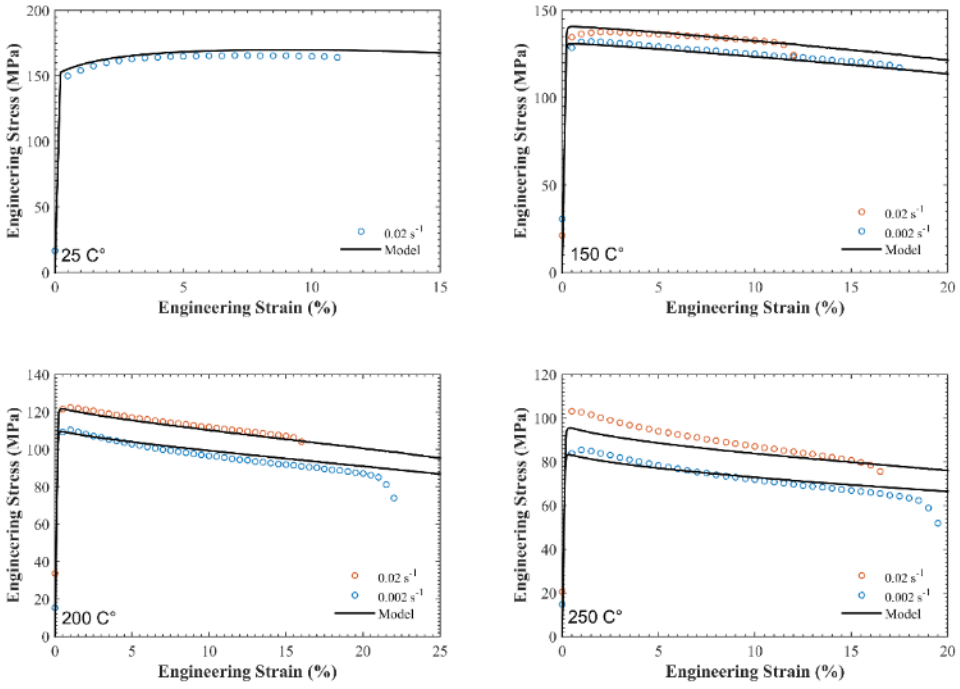

Figure 50: Extended Nadai model tensile simulation results for H22-temper

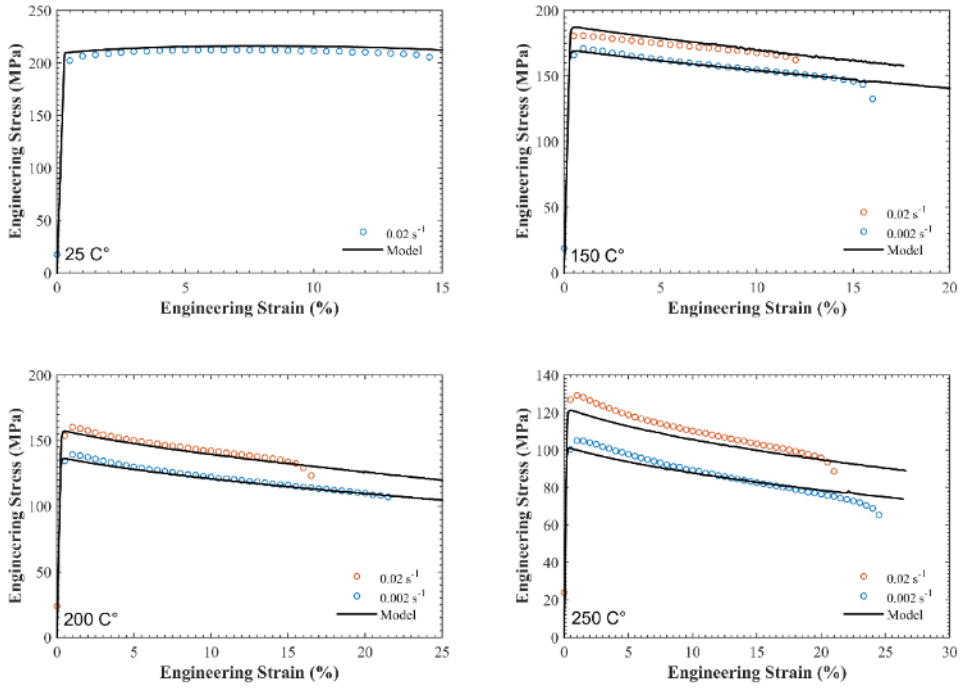

Figure 51: Extended Nadai model tensile simulation results for H24-temper

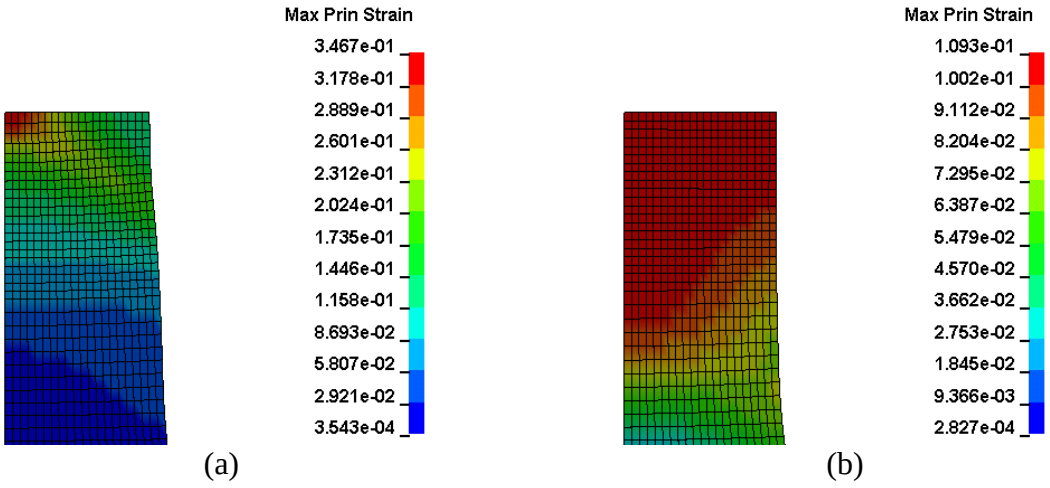

Figure 52: Maximum principal strain at 7mm displacement for H24 at (a) 25°C (b) 250°C

3.2.4 Dynamic Explicit vs Implicit Scheme

The tensile simulations were performed with an implicit time integration scheme since the time step size of a dynamic explicit scheme is limited by the Courant criterion which implies that the

time step size must be smaller than the time for a stress wave to travel across the smallest element in the finite element mesh. Since the element size in the tensile mesh is extremely small (0.05 mm), the computation time would be too large to use an explicit scheme. The implicit scheme is not bounded by the Courant criterion thus a much larger time step size can be used which decreases the total computation time required. However, typical forming simulations are performed with a dynamic explicit scheme to avoid convergence problems with the implicit scheme associated with the strong level of non-linearity due to contact and material softening. Forming simulations often implement mass scaling, which arbitrarily increases the density of the mesh to increase time step size for reduced computation cost. Therefore, a tensile simulation was performed with the explicit dynamic scheme with a mass scaling factor of 10^7 to assess the resulting accuracy. The tensile simulation results are shown in Figure 53 and which serve to demonstrate that the explicit dynamic formulation with mass scaling produces the same result as the implicit formulation.

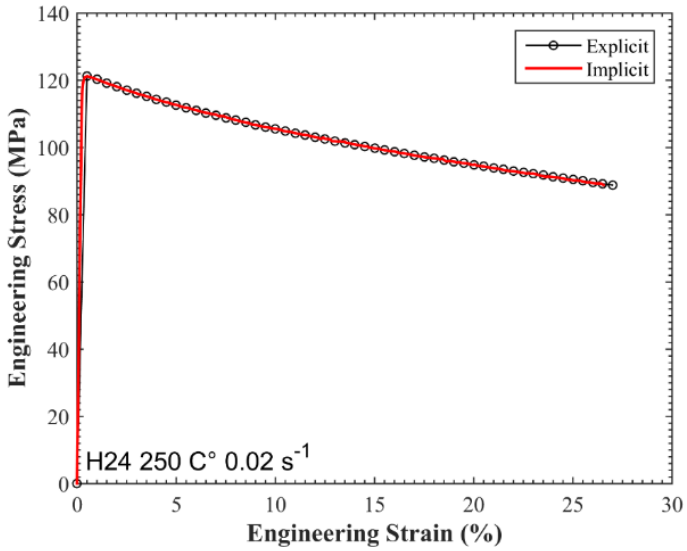

Figure 53: Tensile simulation performed with dynamic explicit *versus* implicit schemes

3.3 Forming Simulation Models

The forming simulations were run with the non-linear dynamic explicit formulation in LS-DYNA. The blank material is 0.2 mm thick and modeled with 4-node quadrilateral shell elements (Type16 fully integrated) [86] with four in-plane and seven through-thickness integration points (Gaussian quadrature). The tooling was modeled as rigid quadrilateral shells; therefore the mesh only had to be dense enough to capture the local curvature of the tooling; thus it was ensured that each radius

feature was traversed by at least 6 elements. Since the experiment was done under isothermal conditions, a regular structural analysis without a thermal (heat transfer) component was sufficient. The single-stage forming simulation (TC1 and TC4) consisted of three components which are the punch, die and blank, as shown in Figure 54 and Figure 55.

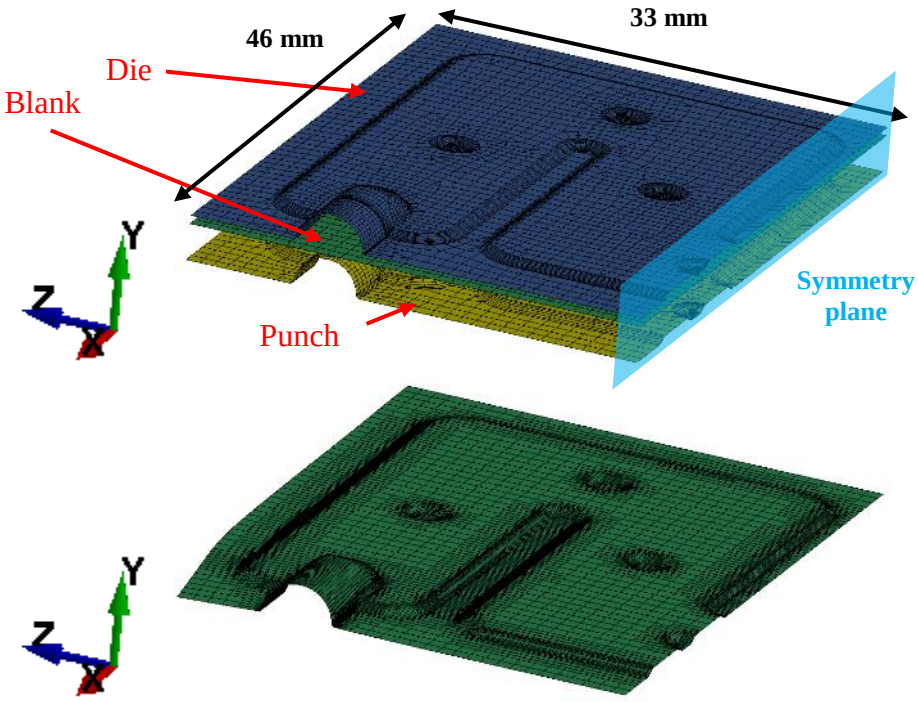

Figure 54: TC1 model. Initial mesh (top) and deformed mesh at the end of the simulation (bottom)

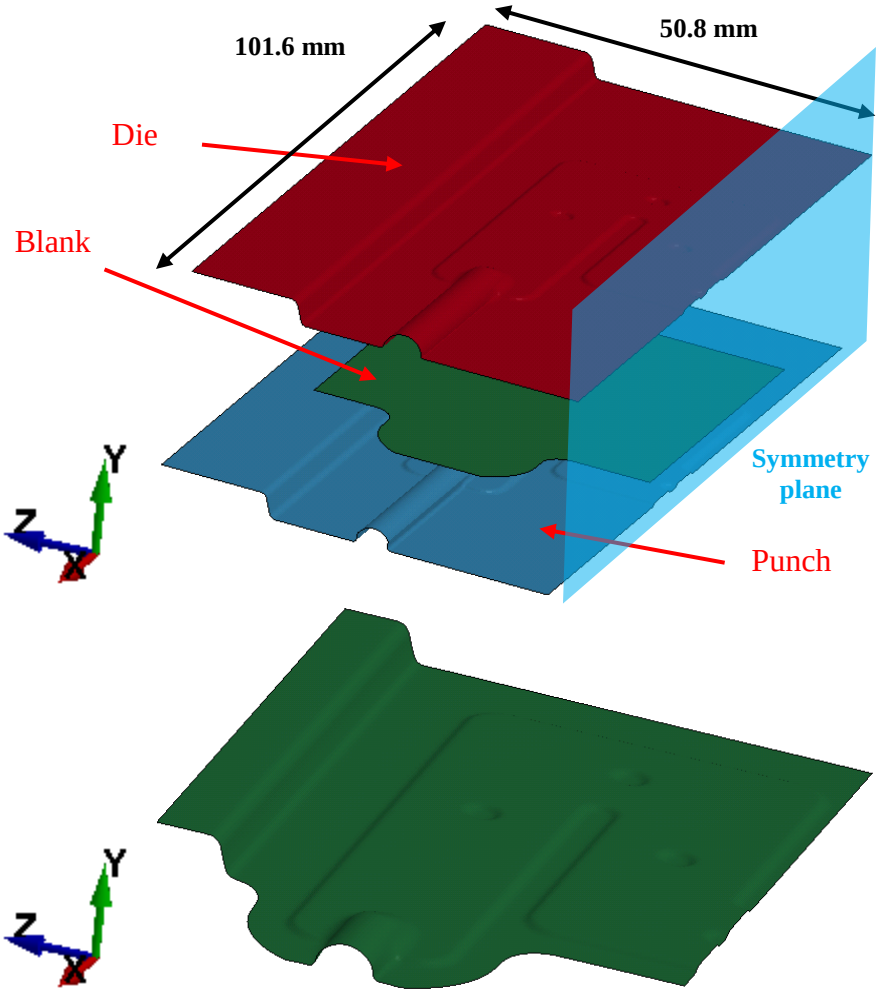

Figure 55: TC4 model. Initial mesh (top) and deformed mesh at the end of the simulation (bottom)

The multi-stage forming simulations (TC2 and TC3) have an additional die and punch for the first stage of the forming process, as shown in Figure 56 and Figure 57. In the multi-stage forming, the deformed mesh and predicted stresses, strains and thickness reductions from the first stage are used to initialize the second stage forming simulation. For the TC2 and TC3 forming simulations, the second stage tooling mesh is identical to that used for the tooling in the TC1 single stage forming simulation.

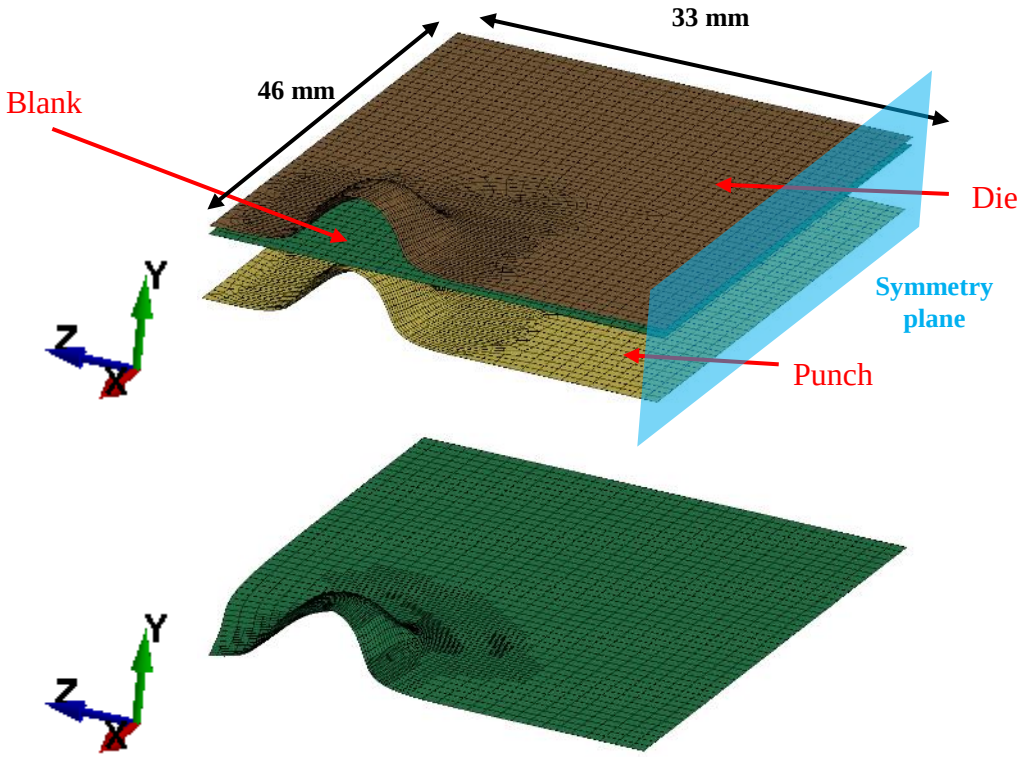

Figure 56: First stage of TC2 model. Initial mesh (top) and deformed mesh at the end of the simulation (bottom)

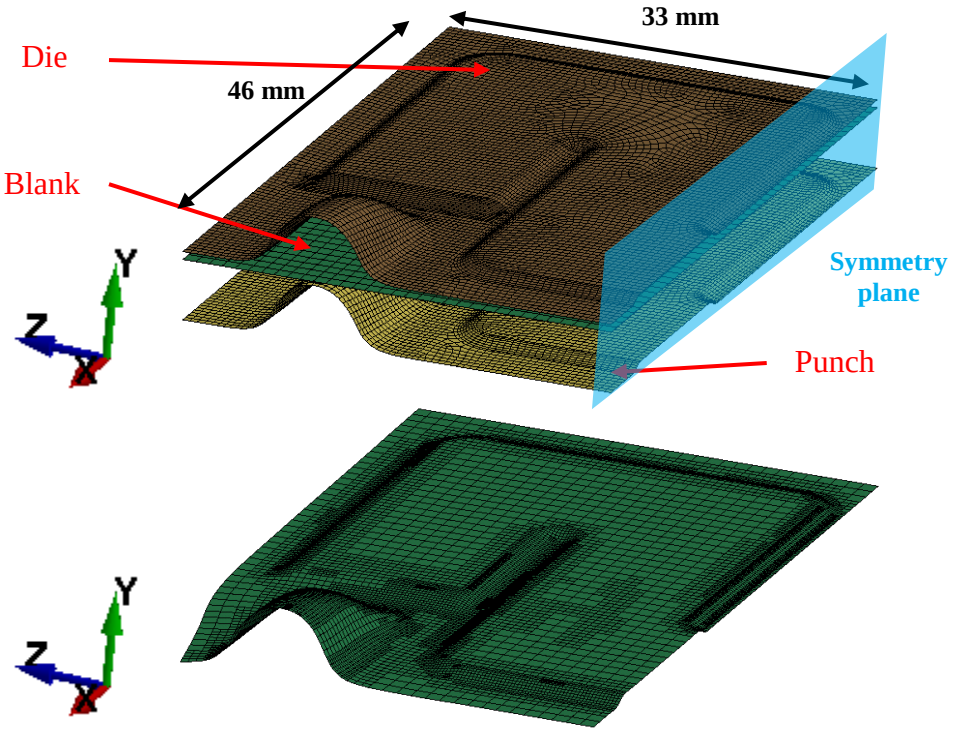

Figure 57: First stage of TC3 model. Initial mesh (top) and deformed mesh at the end of the simulation (bottom)

The blank was initially meshed with a 1 mm element size but adaptive meshing was utilized during the simulation. The adaptive meshing automatically refines the mesh to smaller sized elements based on the local sheet curvature. Elements are refined locally when the total angle change relative to surrounding elements exceeded 5 degrees. This feature reduces the computation time as only the regions that require high mesh density are meshed with small element sizes. The curvature-based adaptivity approach detects proximity to local sharp tooling features at which strain gradients tend to be high, requiring finer meshing. The highest refinement reduced the element size down to 0.0625 mm from the initial 1 mm, which corresponds to five levels of local refinement. For TC4, due to irregular shape of the blank (Figure 26), adaptive meshing was not implemented to have better control on discretization. Instead, the blank was meshed with a 0.15 mm element size.

For TC1 to TC3, the extended Nadai model developed in the previous section was not available at the time of tooling development. Therefore, a previously developed material model due to Ghavam *et al.* [33] for aluminum brazing sheet was utilized instead. This material model was implemented within a User Defined Material Model (UMAT) subroutine created for O-temper brazing sheet with a thicker gauge of 0.5 mm. The material model implemented the Bergstrom hardening model [22] and Barlat Yld2000 yield criterion [34]. For simulation of the TC4 tooling for springback analysis, the UMAT was abandoned since it only considered O-temper sheet and the extended Nadai model, presented in Section 3.1.2, was adopted.

There were several different boundary conditions imposed on this model. Only one-half of the model was simulated due to the symmetry boundary condition along the x-y plane. Since the springback behavior might be asymmetrical, a full model was simulated when the springback result was required. The punch was constrained in all directions except translation in the y-axis. The die was constrained in all directions. A sinusoidal velocity motion with a peak velocity of 1 mm/s was imposed on the punch for a displacement in the positive y-direction until the gap between the punch and die is equal to the thickness of the blank (0.2 mm). The sinusoidal wave form was used to minimize inertial effects when initial contact is made between the blank and tooling. If the effect of punch load had to be considered, the punch was displaced further and the forming simulation was terminated when the required punch load was achieved. Two penalty-

based surface-to-surface contact boundary conditions were imposed between the blank and two tooling components (die and punch). Both the static and dynamic coefficients of friction between the blank and the rest of tooling were defined as the value obtained in the friction characterization. The coefficient of friction was approximated as a linear function of temperature according to Equation (2), (3) and (4) and summarized in Table 7

Table 7: Coefficients of friction for core and clad layers at dry condition and Teflon lubricant at different temperatures

Temperature	25°C	250°C	300°C	350°C
Core (dry)	0.87	1.32	1.43	1.53
Clad (dry)	0.20	0.70	0.81	0.93
Teflon lubricant	0.15	0.30	0.33	0.37

In order to reduce computation time, the forming simulations utilized the mass scaling technique with a factor of 10^7. Simulations were also run using mass scaling factor of $10^4$and no differences were observed as shown in Table 8.

Table 8: Effect of mass scaling

	Model 1	Model 2
Mass Scaling Factor	10^7	10^4
Run Time (Hours)	9	306
Kinetic Energy (N-mm)	0.514	0.139
Internal Energy (N-mm)	3404	3282
Maximum Von Mises Stress (MPa)	244.3	245.2
Maximum Effective Strain	0.318	0.328

The kinetic energy, internal energy and external work were also monitored to ensure that dynamic effects were negligible within the simulations. If the kinetic energy is significantly small compared to the internal energy and external work, then mass scaling is considered acceptable in the simulation.

4 Forming Process Development

This chapter presents the numerical and experimental results used to develop the warm forming process and describes the procession of different tooling configurations considered to improve part formability and limit springback. This chapter focuses primarily on the formability improvements, while Chapter 5 addresses springback control. Formability of the Surrogate Heat-exchanger Component (SHC) is assessed primarily in terms of visible cracking in the experimentally formed parts and visual assessment of the degree of wrinkling. In the corresponding models, excessive thinning was used to indicate potential for onset of cracking and wrinkling was often evident in the deformed part geometry. For TC4, the forming limit curves developed Jain [43] were also considered in assessing part formability.

4.1 Tooling Configuration 1 (TC1)

4.1.1 Model Predictions

For TC1, a single operation was considered to form the SHC using the tooling shown in Figure 24. Numerical simulations were performed to assess the formability of the SHC at both room temperature and 250°C for O-temper condition brazing sheet (Figure 58). The numerical simulations revealed a formability issue around the input/output (I/O) port due to tight radii as seen in Figure 59 and Figure 60 for forming at 25°C and 250°C, respectively. The models predicted localization at the radius and associated excessive thinning as is evident in the figures.

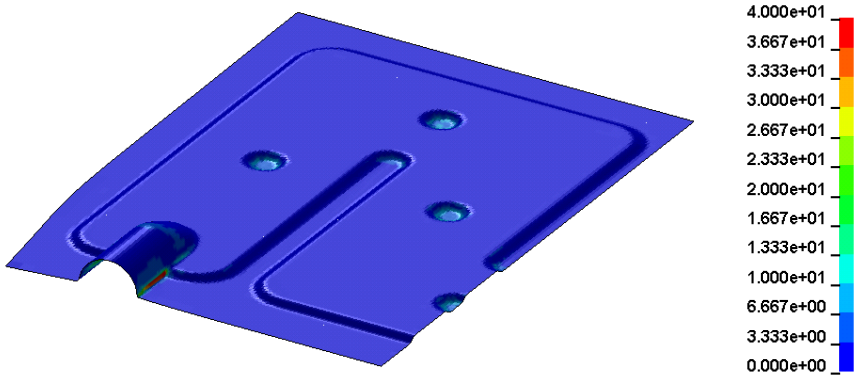

Figure 58: Macro contour plot of percent thickness reduction for TC1: O-temper, 25°C forming temperature

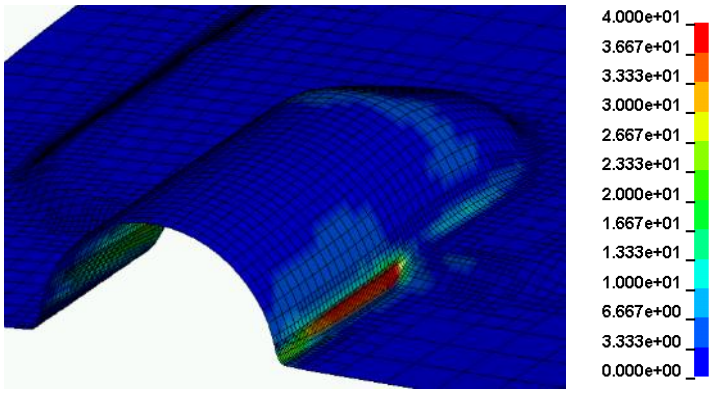

Figure 59: Contour plot of percent thickness reduction for TC1: O-temper, 25°C forming temperature

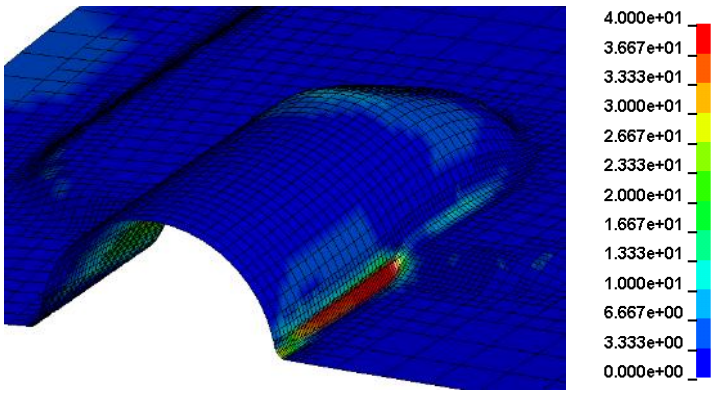

Figure 60: Contour plot of percent thickness reduction for TC1: O-temper, 250°C forming temperature

The I/O port feature remained a formability challenge even at elevated temperatures and it was likely that warm forming alone would not be sufficient to form the I/O port in a single step. This issue was intensified when the harder H22- and H24-tempers are introduced.

4.1.2 TC1 Experimental Results

The simulation results were validated by performing a forming experiment with the experimental parameters shown in Table 9. The experiment was conducted with the softest and hardest material tempers at 25°C and 250°C with three lubrication conditions. The results for the forming experiment using the TC1 arrangement is also summarized in Table 9 and formed parts are shown in Figure 61.

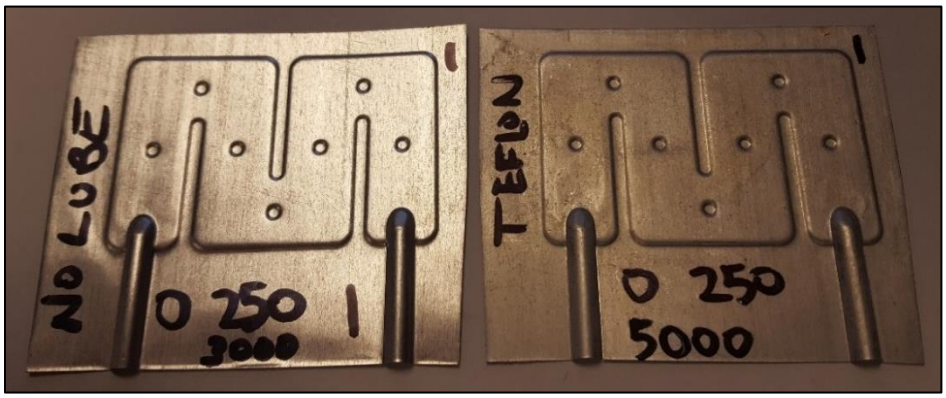

Figure 61: TC1: O-temper formed at 250°C at dry condition (left) and with Teflon (right)

As predicted by the simulations, the SHC could not be formed under any of the conditions, even with the softest temper since fracture occurred at the tight radii at the I/O port, as shown in Figure 62. It was concluded that modifications to the tooling configuration and/or the forming process are necessary in order to overcome the formability challenges associated with the SHC.

Table 9: TC1 forming experiment results (O = formed successfully X = fracture occurred)

Material Temper	Temperature	None	Teflon	Fuchs
H24	RT	X	X	X
	250	X	X	X
O	RT	X	X	X
	250	X	X	X

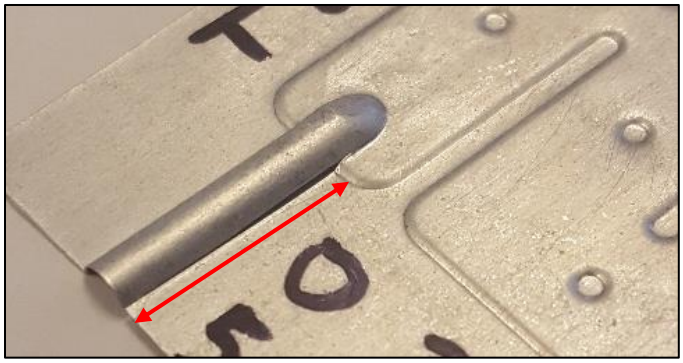

Figure 62: TC1: O-temper formed with Teflon lubrication at 250°C. A fracture runs along the I/O port radius, parallel to the red line drawn on the image.

4.2 Tooling Configuration 2 (TC2)

4.2.1 Geometry Selection

In order to improve the part formability, a two-step forming process in which the majority of the I/O port is formed in the first step and then the rest is formed in the second step, was developed as shown in Figure 63. The pre-form (PF) profile is formed first as a large protrusion with large feature radii. The pre-form operation serves to "gather material" around the I/O port feature and distributes the strain across the entire section of the initial curvature rather than promoting high localized strains around the tight radii in the final form (FF) profile. In the final form operation, the pre-form profile is compressed into the final shape of the I/O port. Both PF and FF profiles are designed to have a similar arc length thus most of the stretching is accomplished in the PF stage and only bending occurs in the FF stage.

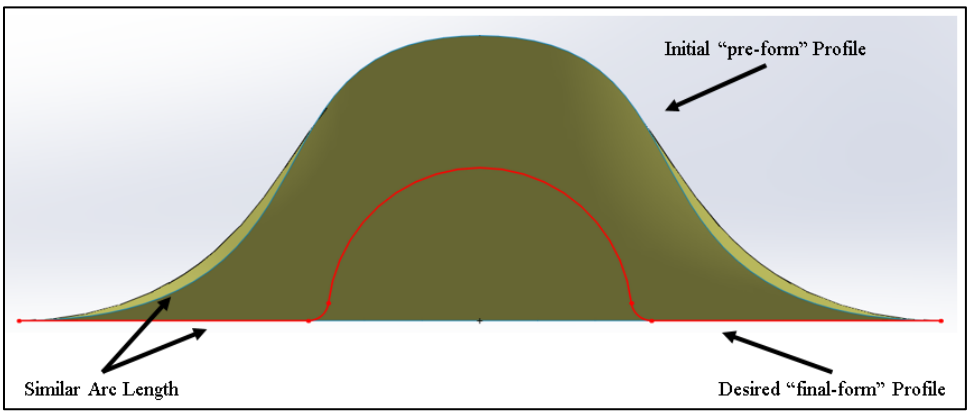

Figure 63: Multi-stage forming schematic

Initially, several different PF geometries were simulated to assess the effect of the multi-stage forming approach. It was important to ensure that the thickness reductions in both stages are low to ensure that fracture does not occur. Figure 64 shows two distinct PF geometries in which geometry A is more aggressive with larger curvatures and arc length compared to geometry B.

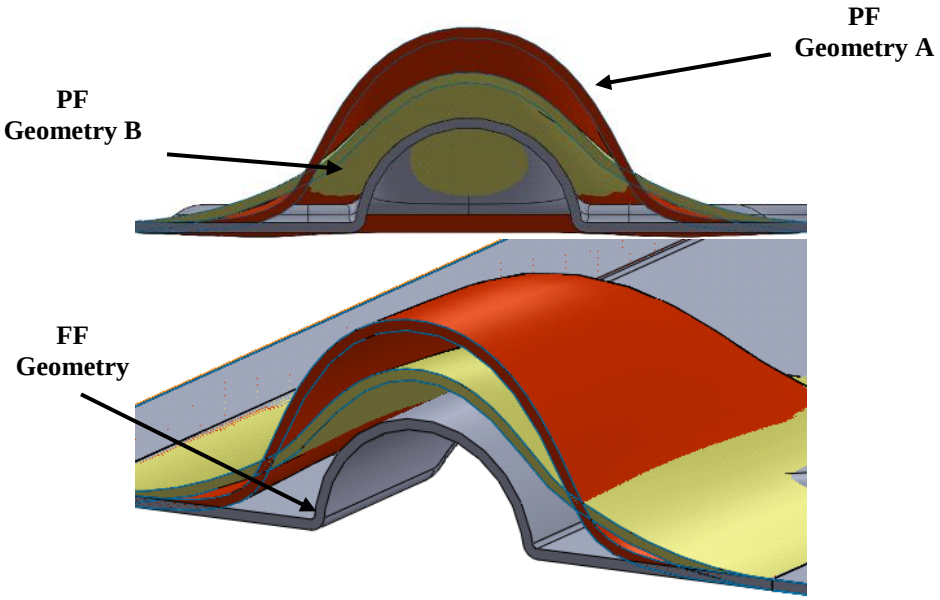

Figure 64: PF geometry A (red) and B (yellow) and FF geometry (grey)

The simulation results for the two PF geometries are summarized in Figure 65 and Figure 66. The PF geometry had significant impact on the formability of the FF operation. The general trend observed was that lower strains during the PF stage tended to promote higher strain in the FF stage. For geometry B, the maximum thickness reduction in the PF stage was only 2.5%; however, severe sheet thinning of 42% resulted during the FF stage. For geometry A, the PF geometry had adequate deformation (10% thinning) such that both the PF and FF stages contributed to moderate thickness reduction. It became apparent from the simulations that there is a finite amount of strain to be distributed between the two forming stages and that fracture occurs when high strains were required in the FF stage. Therefore, the design approach was to apply as much strain as possible in the PF stage without fracture.

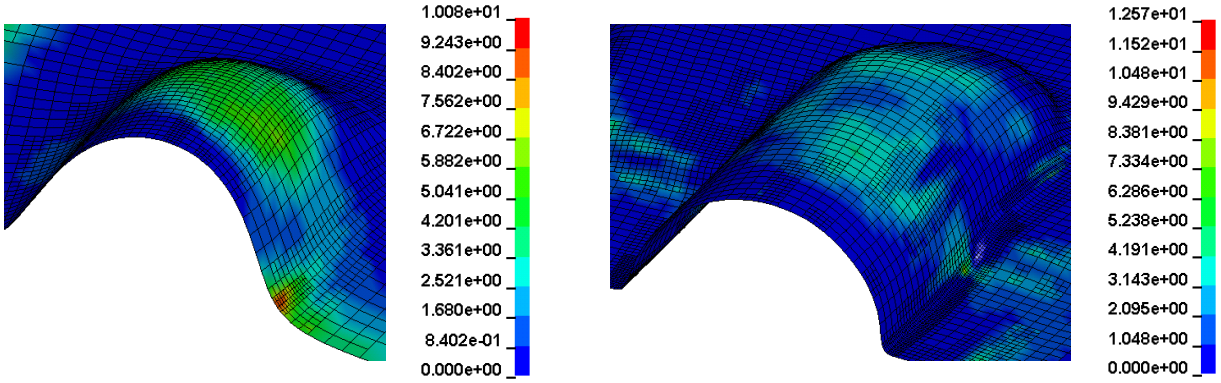

Figure 65: Contour plot of percent thickness reduction for TC2 using geometry A: O-temper, 250°C forming temperature. PF (left) and FF (right)

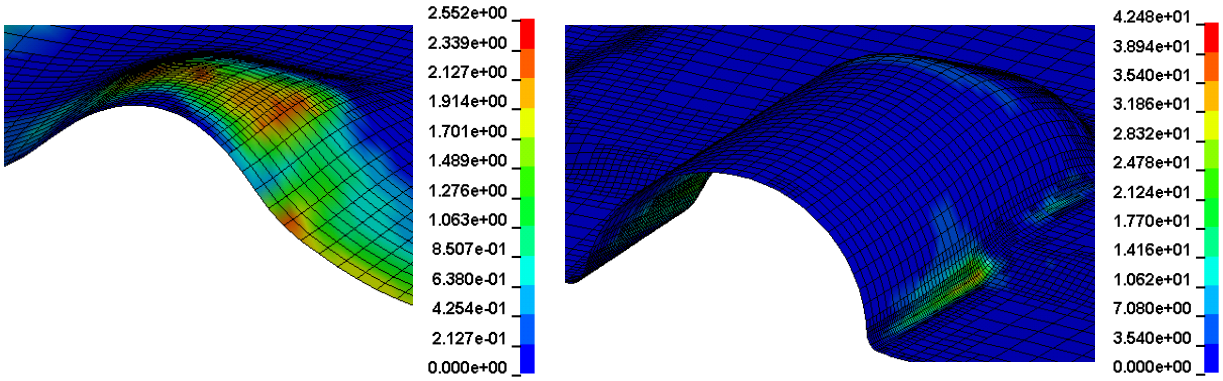

Figure 66: Contour plot of percent thickness reduction for TC2 using geometry B: O-temper, 250°C forming temperature. PF (left) and FF (right)

Furthermore, the thickness reduction behavior was found to a strong nonlinear function of the forming history. Two different geometries with a similar thickness reduction in the PF stage could have totally different thickness reductions after the FF stage. For example, two similar PF geometries C and D in (Figure 67) had a similar thickness reduction values of 5.92% and 5.97% in the PF stage as shown in Figure 68 and Figure 69. However, their final thickness reduction values in the FF stage was completely different with values of 34.1% and 13.2%. This again shows that the final thickness reduction value depends very heavily on the PF geometry and the forming history.

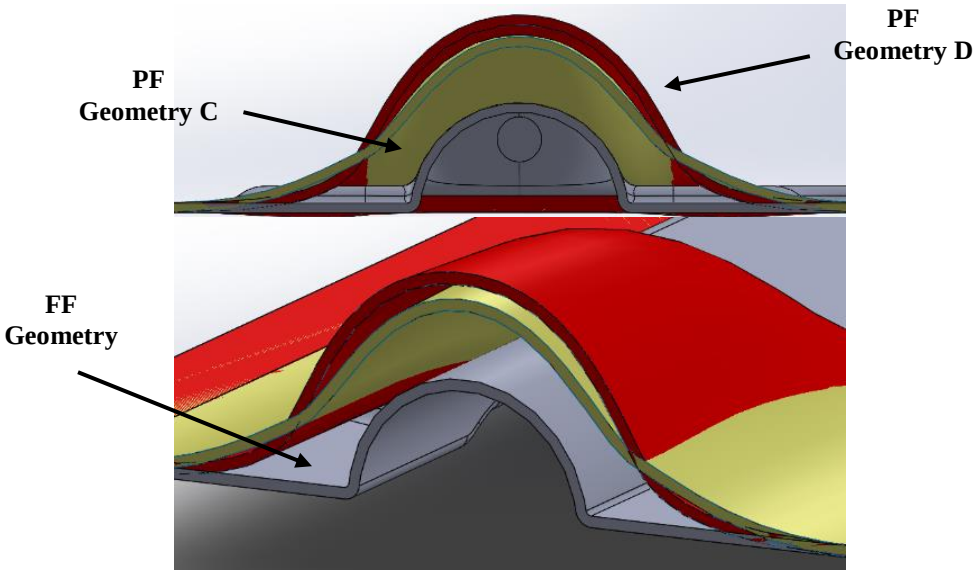

Figure 67: PF geometry C (yellow) and D (red) and FF geometry (grey)

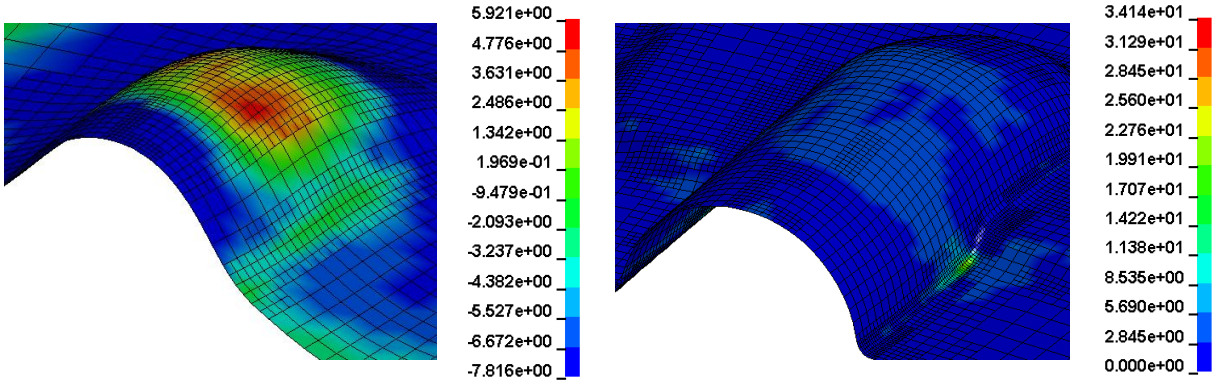

Figure 68: Contour plot of percent thickness reduction for TC2 using geometry C: O-temper, 250°C forming temperature. PF (left) and FF (right)

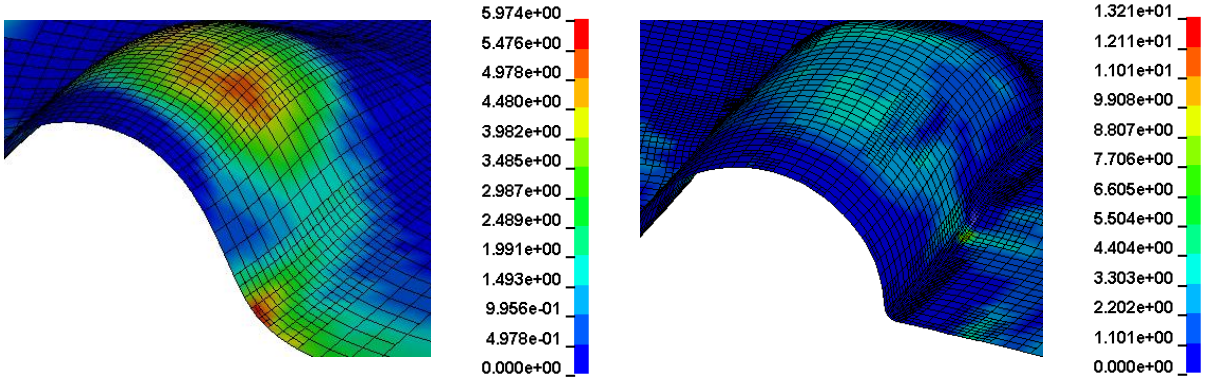

Figure 69: Contour plot of percent thickness reduction for TC2 using geometry D: O-temper, 250°C forming temperature. PF (left) and FF (right)

After a set of trial-and-error simulations, a PF geometry with the best formability performance was selected as a baseline geometry. The purpose of the baseline geometry was to serve as a reference against which the formability improvement can be assessed in a simple parametric/systematic study. For this study, the PF geometry is defined by a surface generated from three curvature profiles, as shown in Figure 70. The three profiles were created using thirteen geometrical parameters (Figure 70) defined within SolidWorks CAD program. Each profile was defined relative to the FF geometry with parameters comprising the vertical offset distance and location of the inflection point, as shown in Figure 70**.** The curvatures were generated by utilizing splines which are commonly used to create complex curves and controlled by tangency weight and direction as shown in Figure 72 and Figure 73.

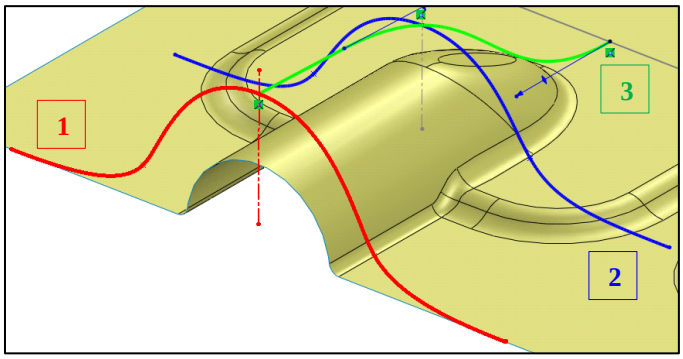

Figure 70: CAD of the three curvature profiles generating the PF geometry surface, defined relative to the FF geometry

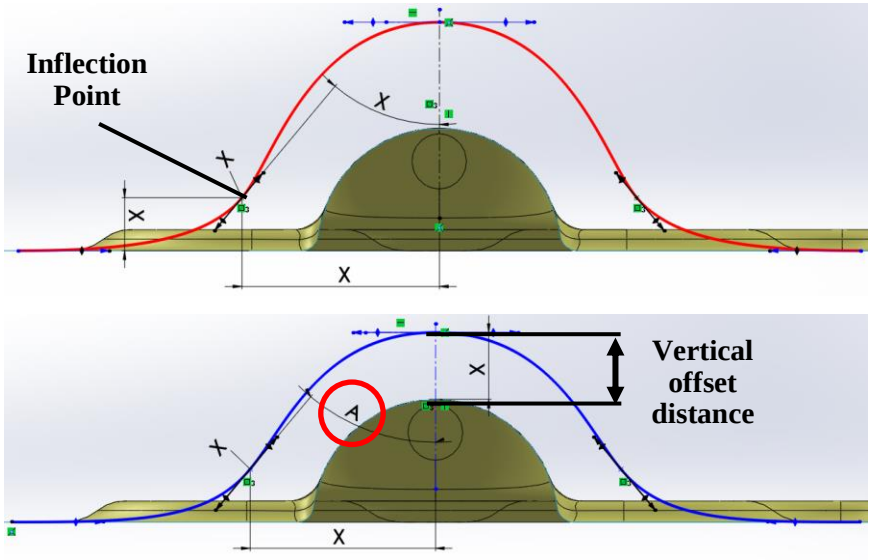

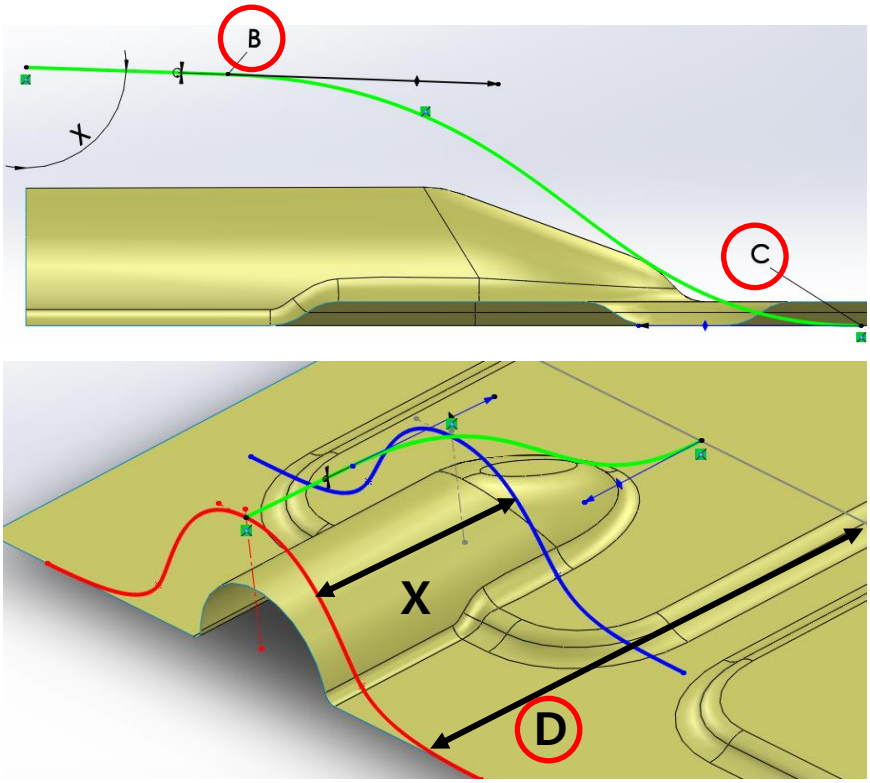

Figure 71: Thirteen geometrical parameters defining the three curvature profiles and four chosen parameters (A, B, C, and D)

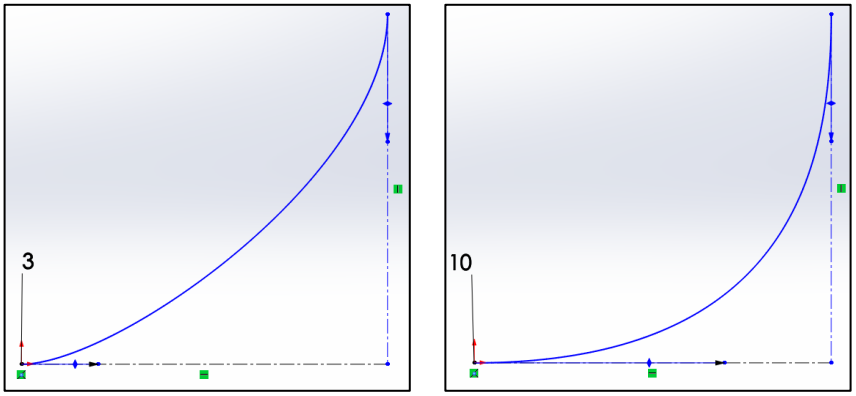

Figure 72: Effect of tangency weight on spline

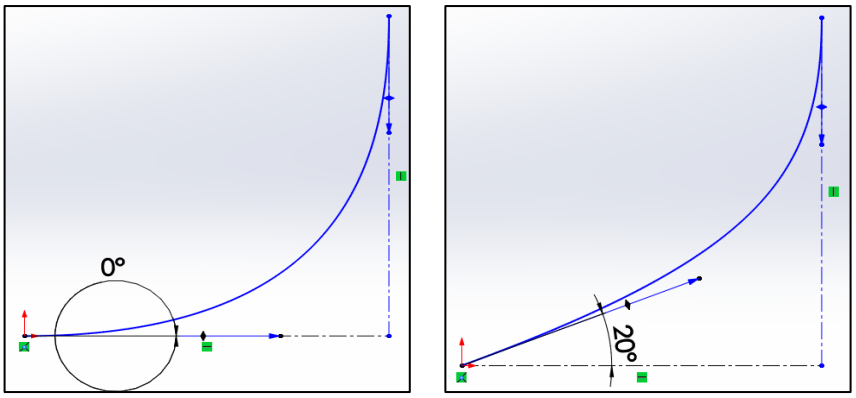

Figure 73: Effect of tangency direction on spline

The selection procedure consisted of varying each parameter to three different design levels (low, mid and high) and evaluating the thickness reductions at both the PF and FF stages. In order to simplify the selection process, four parameters (herein denoted as A, B, C and D) with the most influence on the thickness reduction were selected for a full factorial study. The four chosen parameters and their design levels are shown in Figure 71 and Table 10.

Table 10: Design levels for the four chosen parameters

Parameters	Low	Mid	High
A	40°	45°	50°
B	15 mm	17 mm	19 mm
C	14 mm	15 mm	16 mm
D	12 mm	14 mm	16 mm

Parameter A controls the angle of the side wall in the curvature profile 2, B and C control the top and bottom tangency weights of the curvature profile 3, and D controls the overall length of the PF geometry, respectively. In total, there were 3^4 design iterations as there were three design levels for each of the four parameters. The effects of the four chosen parameters on the thickness reductions of PF and FF at the different design levels are shown in Figure 74.

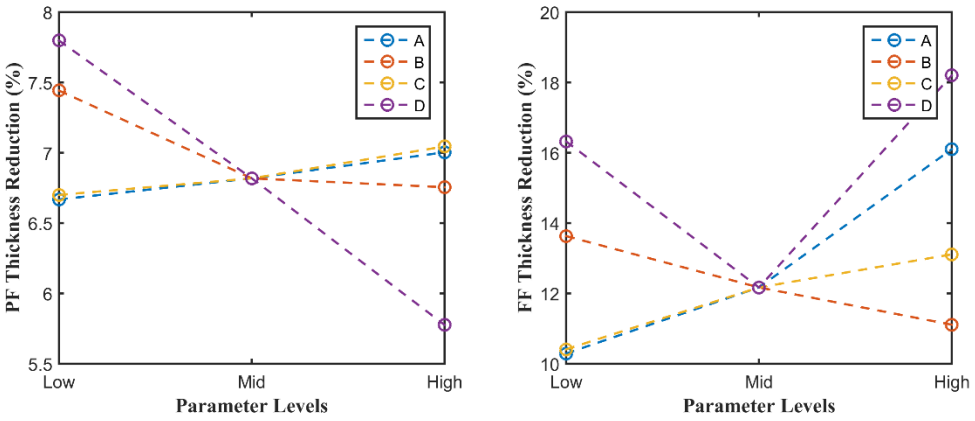

Figure 74: Effect of the four selected parameters on PF and FF thickness reduction %

The factorial study revealed that the minimum thickness reductions occurred at: A at low, X2 at mid, X3 at low and X4 at mid-parameter levels. Through the factorial study, the maximum thickness reductions were changed to 7.0% and 10.3% for the PF and FF stages, respectively,

which represents an improvement compared to the thickness reduction predicted for the baseline geometry (6.8% and 12.2% thickness reduction for the PF and FF stages, respectively).

4.2.2 TC2 Experimental Results

4.2.2.1 Formability

New tooling was fabricated (referred to as the TC2 configuration, shown in Figure 24) using the selected PF geometry and the SHCs were formed again. The experimental results for the O-temper material are summarized in Table 11. The O-temper material exhibited excellent formability and fracture did not occur. The O-temper material formed successfully for both the PF and FF geometries at every condition considered including the dry (no lubricant) room temperature condition due to its high ductility. The as-formed O-temper samples are shown in Figure 75 and Figure 76.

Table 11: O-temper experimental results for TC2 (O = formed successfully X = fracture occurred)

Preform				Final form			
	None	Teflon	Fuchs		None	Teflon	Fuchs
RT	O	O	O	RT	O	O	O
				250	O	O	O
250	O	O	O	RT	O	O	O
				250	O	O	O

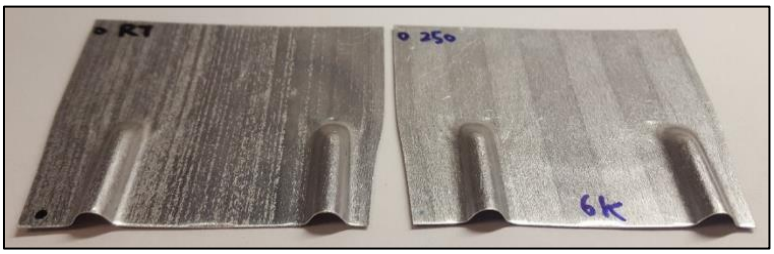

Figure 75: O-temper PF without lubrication at 25°C (left) and 250°C (right)

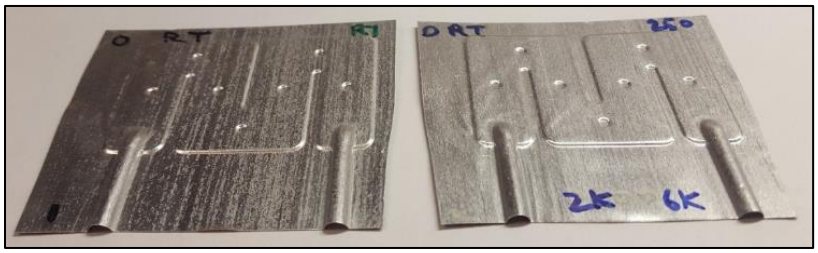

Figure 76: O-temper FF without lubrication at 25°C (left) and 250°C (right)

The initial experiments revealed that the thickness reduction in the PF stage was severe and caused fracture when the die sets were fully closed for harder temper materials, regardless of the forming temperature and lubrication condition. (Recall that the simulations for TC1-TC3 only considered O-temper sheet.) To alleviate this issue, the dies were only partially closed by limiting the punch load to a range of values in order to test different levels of strain in the PF stage. In the subsequent FF stage, the die sets were fully closed for all conditions. The fully closed position was determined by examining the force-time plot of the PF geometry as shown in Figure 77. Due to very thin gauge of the material, the punch load required to form the PF geometry was relatively low. At around 6 kN, the component was fully formed and the dramatic increase in punch load is attributed to the compression of the formed component within the dies.

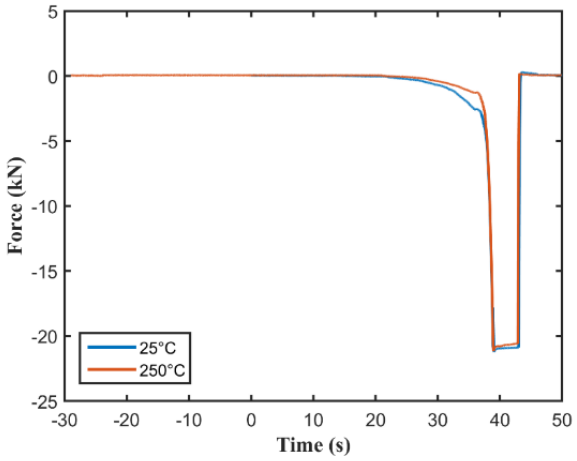

Figure 77: Force-time plot of PF geometry for H24-temper

The experiment results for the H24-temper material are summarized in Table 12 and Table 13. The H24-temper material failed to form the PF geometry at high punch load conditions including the fully closed condition regardless of the temperature and lubrication conditions. However, the PF geometry successfully formed at room temperature at lower punch force conditions with lubricated conditions having higher tolerable punch force. For elevated temperature conditions, the attainable punch load before fracture was much lower compared to room temperature which was expected due to thermal softening of the material. The maximum attainable punch loads without fracture during preforming were 3000N and 1250N for room temperature and elevated temperature conditions, respectively. The FF geometry only formed at these specific PF punch load conditions since the strain level in the PF was either too large or too small for other punch load conditions.

Table 12: H24-temper experimental results for TC2 at 25°C (O = formed successfully X = fracture occurred)

H24	Preform				Final form			
Load		None	Teflon	Fuchs		None	Teflon	Fuchs
6000	RT	X	X	X	RT			
					250			
4000	RT	X	X	X	RT			
					250			
3000	RT	X	O	O	RT		O	O
					250		O	O
2000	RT	X	O	O	RT		X	X
					250		X	X
1500	RT	O	O	O	RT	X	X	X
					250	X	X	X
1000	RT	O	O	O	RT	X	X	X
					250	X	X	X

Table 13: H24-temper experimental results for TC2 at 250°C (O = formed successfully X = fracture occurred)

H24	Preform				Final form			
Load		None	Teflon	Fuchs		None	Teflon	Fuchs
2000	250	X	X	X	RT			
					250			
1500	250	X	X	X	RT			
					250			
1250	250	X	O	O	RT		O	O
					250		O	O
1000	250	X	O	O	RT		X	X
					250		X	X
750	250	X	O	O	RT		X	X
					250		X	X
500	250	O	O	O	RT	X	X	X
					250	X	X	X

The H24 PF profiles formed at different loads at each temperature can be seen in Figure 78. As the punch load increased, the blank formed a shape closer to the PF geometry. For the elevated temperature condition, the PF geometry was formed at a lower punch load hence the reason why the maximum load before fracture is lower at elevated temperatures. At the punch load of 4000N and 1500N for 25°C and 250°C respectively, the blanks start to resemble the fully-formed PF geometry at which point fracture occurs due to a high level of stretching. At room temperature and a punch load of 2000N and below (1000N and below for 250°C), the blanks did not undergo sufficient deformation thus severe stretching still occurred in the FF stage which led to fracture.

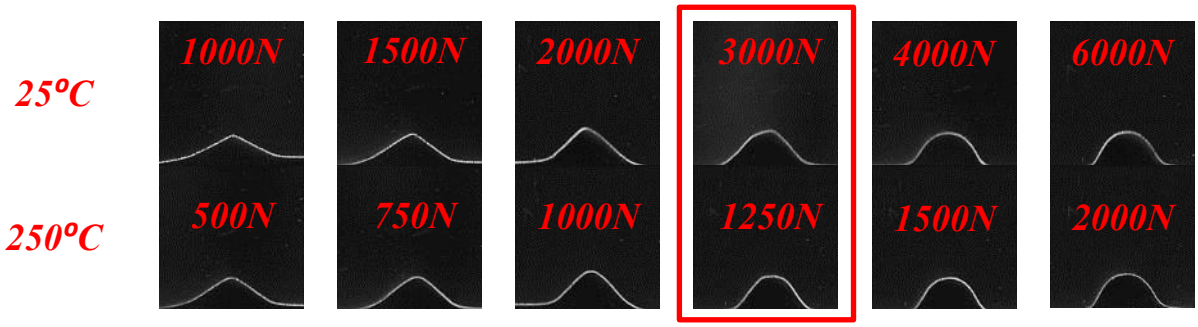

Figure 78: PF profile formed at 25°C and 250°C at different punch loads. Note that the FF was only successful for the PF geometry formed with 3000N and 1250N loads, respectively.

The two PF geometries formed at room temperature and 250°C using loads of 4000N and 1500N, respectively, are compared in Figure 79. These cases correspond to the minimum load at each temperature for which the as-formed shape conforms well to the tooling geometry (Figure 78). It is observed that the crack in the PF geometry formed at elevated temperature was noticeably larger than that formed at room temperature. In addition, the forming temperature in the FF stage for load levels which did not result in cracking during the PF stage, did not have much effect on the formability. From these two observations, the benefit of warm forming is not particularly evident in terms of formability of the SHC. However, the effect of multi-stage forming was clearly demonstrated as the SHC formed successfully when it failed to form with the single-stage forming process at every condition with TC1. For both room temperature and 250°C, the formability window at which both the PF and FF form successfully were identified (3000N and 1250N for 25°C and 250°C respectively). The SHCs formed in this formability window have sheet thinning that is well-balanced between the two forming stages rather than having concentrated thinning in one of the stages.

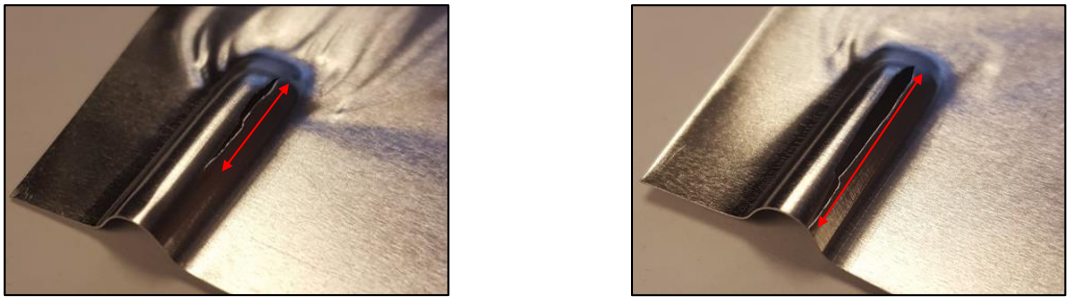

(a) (b)

Figure 79: PF geometry formed with (a) 4000N at 25°C (b) 1500N at 250°C at dry condition

Both lubricants, Teflon and Fuchs, had similar performance and it was concluded that lubricant is important to ensure a successful forming operation as shown in Table 12 and Table 13. Under the same forming conditions, the lubricated parts formed while the unlubricated parts fractured. The effect of lubrication was clearly observed with the size of cracks decreasing with the use of Teflon lubricants as shown in Figure 80 and Figure 81. Through this experiment, the importance of coefficient of friction in metal forming was emphasized again.

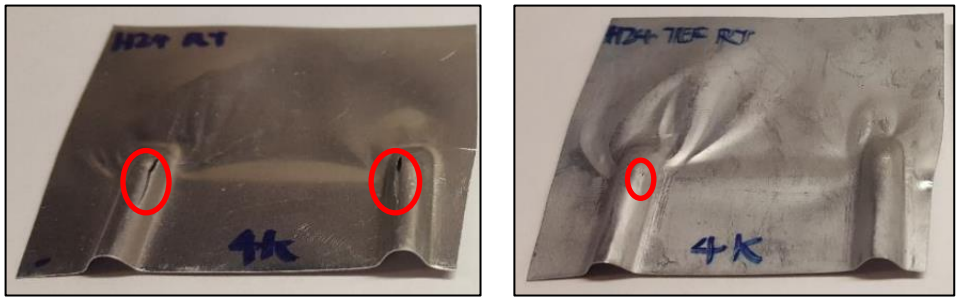

Figure 80: H24-temper: 4000N punch load, 25°C forming temperature, unlubricated (left) Teflon (right)

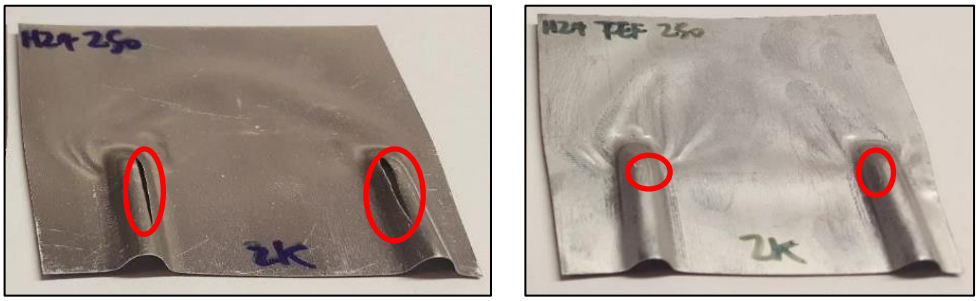

Figure 81: H24-temper: 2000N punch load, 250°C forming temperature, unlubricated (left) lubricated (right)

4.2.2.2 Springback

Although formability did not improve with increasing temperature, qualitative observations showed an improvement in springback at elevated temperature conditions as shown in Figure 82. The SHC formed at 250°C had higher flatness compared to that formed at 25°C which had an upward concave curvature.

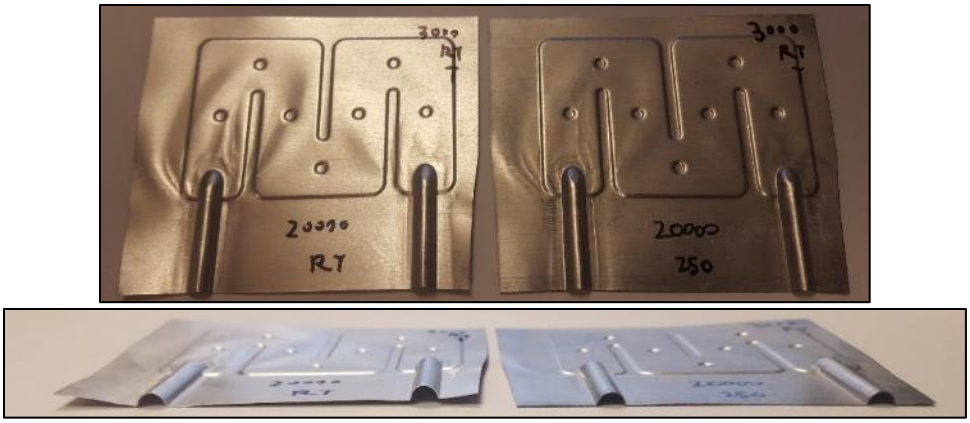

Figure 82: Effect of FF forming temperature on springback in the FF stage. 25°C (left) and 250°C (right). PF forming temperature is 25°C for both specimens

Figure 83 shows the effect of forming temperature in the PF stage on the final SHC component. It was observed that as long as the FF stage is formed at elevated temperatures, the temperature at which the PF is formed has very little effect on the final springback. This observation suggests that most of the geometrical features that contribute to the springback are formed in the FF stage.

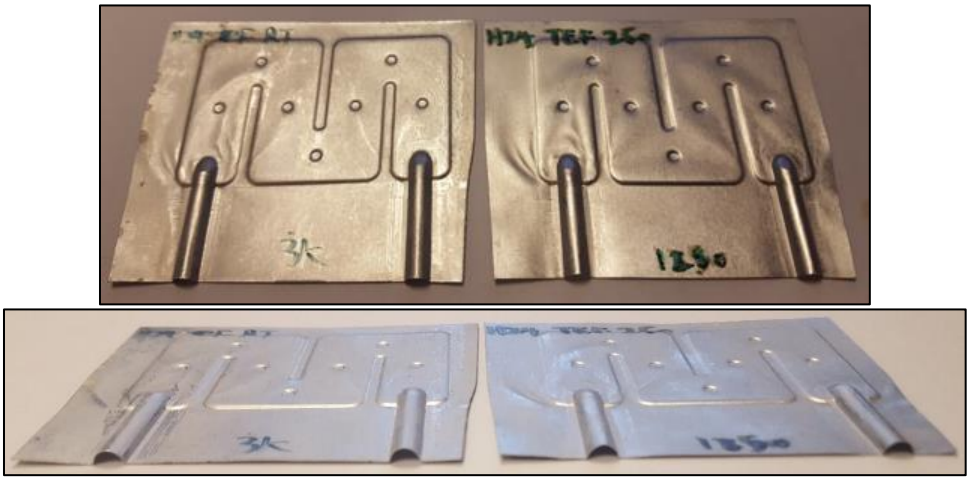

Figure 83: Effect of PF forming temperature on springback in the FF stage. 25°C (left) and 250°C (right). FF forming temperature is 250°C for both specimens

Figure 84 shows the SHCs formed with O-temper sheet at room temperature and with H24-temper sheet at 250°C. It is shown that the degree of springback for the H24-temper material which was formed under warm forming conditions is comparable to the O-temper material that was formed at room temperature. This comparison indicates that the battery plates formed with the H24-temper material utilizing the warm forming process can achieve comparable dimensional accuracy and

component flatness as that of the O-temper material. Thus, the warm forming process is promising from the perspective of enabling the development of more durable, higher performance and lower cost battery plates that cannot be mass produced today due to forming and springback constraints.

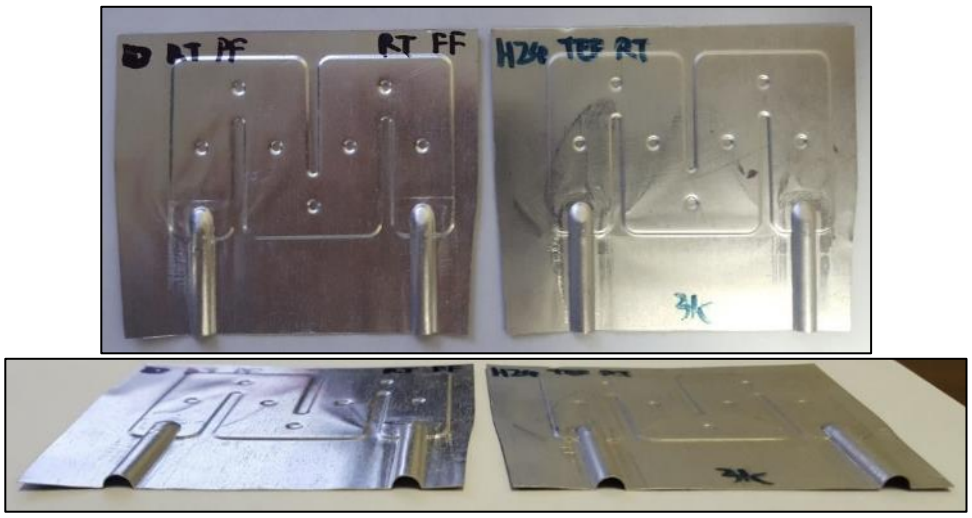

Figure 84: Effect of material temper on springback in the FF stage. O-temper formed at RT (left) and H24 formed at 250°C (right)

4.2.2.3 Wrinkling

One issue encountered with TC2 was significant wrinkling introduced during the PF stage caused by forming the initial I/O feature adjacent to the flat area of the blank, as can be observed in Figure 85. Wrinkling is a phenomenon of compressive instability and is considered a major defect in sheet metal forming [87]. In the PF operation, sheet material is pulled into the sides of the initial I/O feature pre-form geometry, which puts the flat material at the end of the I/O feature into a severe state of compression which triggers wrinkling. Wrinkling was also visible in the numerical simulations, as shown in Figure 86. Components with wrinkling are scrapped in industry as they do not meet the part design and dimensional requirements, and could also result in wear or damage to the dies. The wrinkles were still visible in the final component since the FF stage was not sufficient to flatten the wrinkles, as shown in Figure 85.

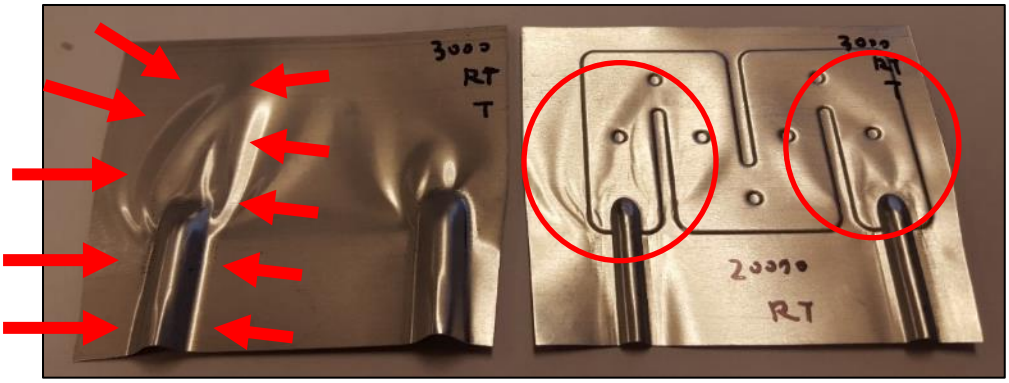

Figure 85: TC2: Wrinkles after PF formed at 25°C (left) and subsequently formed to FF at 25°. H24-temper and lubricated with Teflon

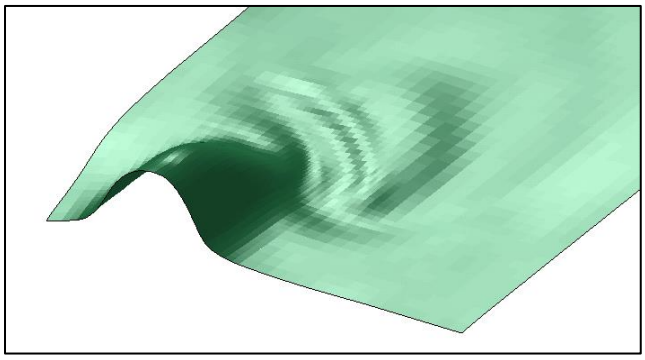

Figure 86: Wrinkles after PF stage in TC2 numerical simulation. O-temper, 250°C forming temperature.

4.3 Tooling Configuration 3 (TC3)

For the third tooling configuration, TC3, several changes were made to the pre-form tooling geometry. In order to reduce the extent of wrinkling, the PF geometry was modified to pre-form the channels as well, as can be seen in Figure 87. The motivation to pre-form the channels is to impart more tensile straining within the previously flat regions of the PF geometry, thereby reducing compressive stress and wrinkling tendency. In addition, by forming the cooling channels, the PF part will have higher stiffness which should also improve part flatness. Both effects were expected to prevent or reduce the tendency for wrinkling within the PF operation. Through more trial-and-error simulations, the I/O port geometry was changed to reduce thickness reductions to 4.3% and 13.4% for the PF and FF stages, respectively from TC2 (7.0% and 10.3% thickness reduction for the PF and FF stages, respectively). Although there was more thinning in the FF operation, there was an overall improvement in thickness reduction (39% less thickness reduction in PF stage *versus* 30% more thickness reduction in FF stage).

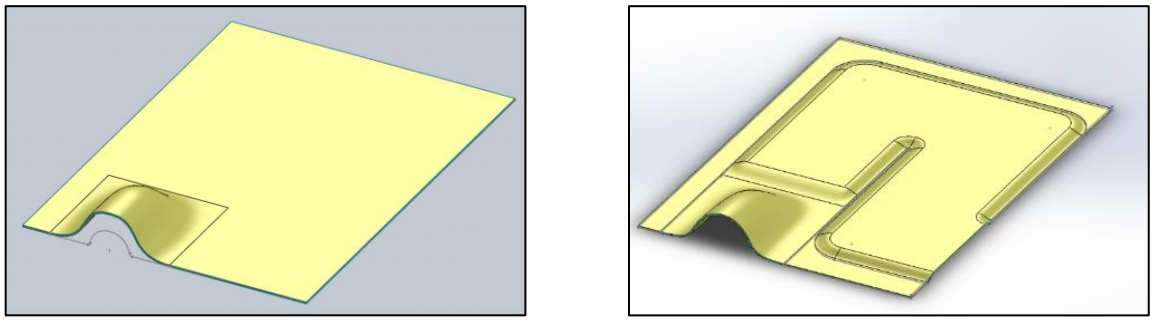

Figure 87: TC2 (left) and TC3 PF geometry (right)

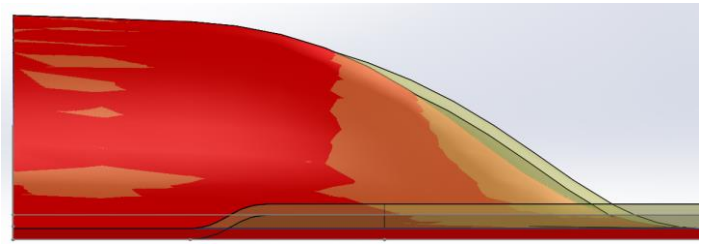

Figure 88: TC2 (red) and TC3 (yellow) I/O ports

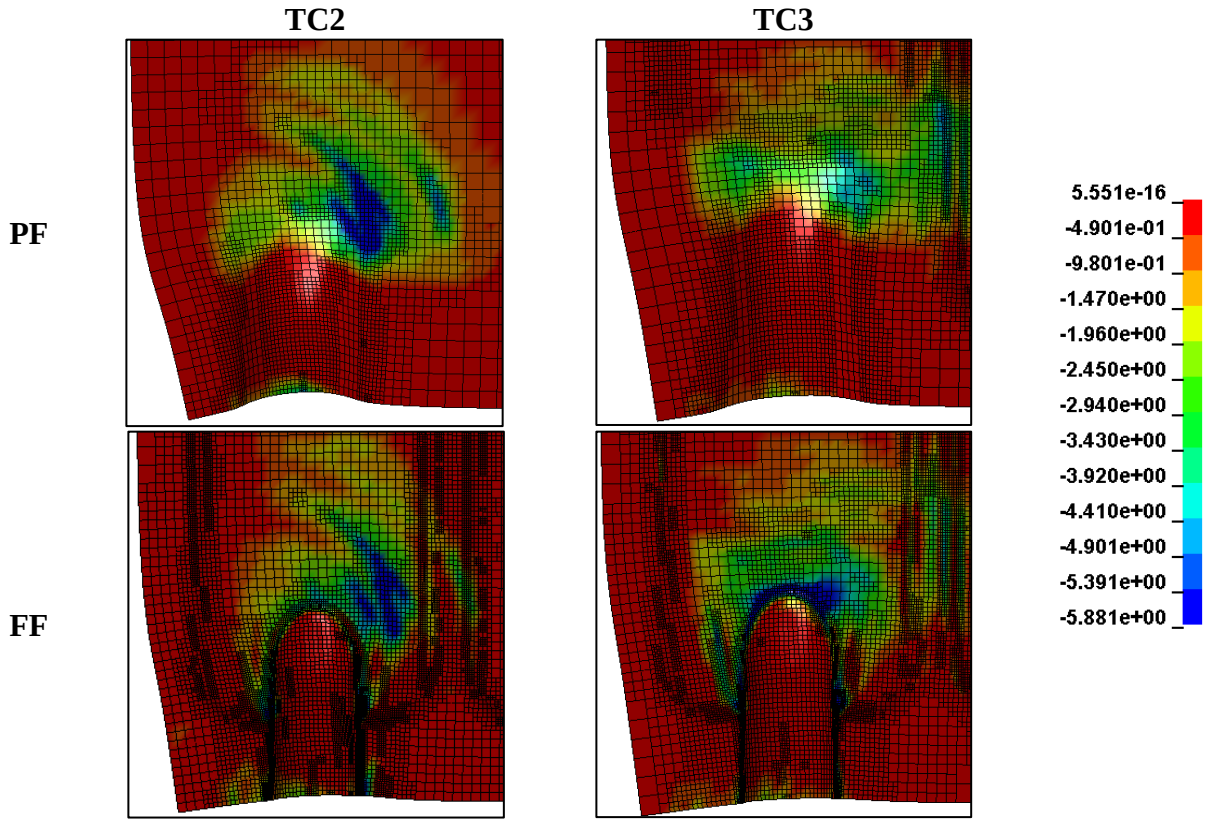

Figure 89: Contour plot of percent thickness reduction for TC2 (left) and TC3 (right) for PF geometry and subsequent FF geometry. O-temper, 250°C forming temperature. Note that negative thickness reduction implies thickness increase.

Numerical simulations were performed to evaluate the potential for the TC3 design to reduce the wrinkling behavior. The tendency to wrinkle for a particular tooling model was examined in the models based on predicted thickness change (Figure 89). Regions with predicted thickness increase were considered more likely to wrinkle since wrinkling is caused by the compression of the blank. The thickness contour plots of the TC2 and TC3 PF geometries and also the resulting FF geometries are found in Figure 89. In accord with the experimental observations, the simulations also showed more wrinkling tendency (larger thickness increase shown by blue regions) in the TC2 PF geometry and the subsequent FF geometry. It was shown that the TC3 PF geometry was able to reduce the severity and affected area of the wrinkling behavior. The introduction of the channel geometry into the PF stage effectively prevented the wrinkles from propagating throughout the sheet reducing the maximum thickness increase from 9.3% to 5.8% in the PF stage.

4.3.1 TC3 Experimental Results

4.3.1.1 Formability

The experimental results for the TC3 tooling configuration are summarized in Table 14. Similar to the TC2 results, both the PF and FF geometries formed without any challenges using the O-temper material. Due to the I/O port geometry optimization, the PF geometry also formed without fracture with the H24-temper material even when the dies were fully closed but only for the lubricated and room temperature conditions. Figure 90 shows the PF geometry formed at room temperature and 250°C without any lubrication. The specimens fractured under both conditions but the size of the crack on the specimen formed at 250°C was larger which indicated worse formability. It was not known why the warm forming condition exhibited lower formability. The same trend was observed again in the lubricated condition, as shown in Figure 91. The PF geometry formed successfully with slight localization at room temperature while it fractured at 250°C.

Table 14: Experimental results for TC3 (O = formed successfully X = fracture occurred)

		PF				FF		
		None	Teflon	Fuchs		None	Teflon	Fuchs
H24	RT	X	O	O	RT		O	O
					250		O	O
	250	X	X	X	RT			
					250			
O	RT	O	O	O	RT	O	O	O
					250	O	O	O
	250	O	O	O	RT	O	O	O
					250	O	O	O

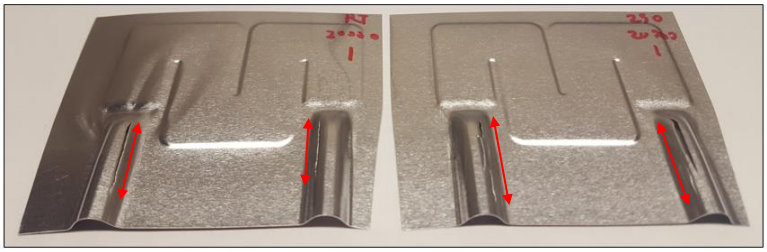

Figure 90: TC3 PF geometry formed with H24-temper sheet at 25°C (left) and 250°C (right) with no lubrication

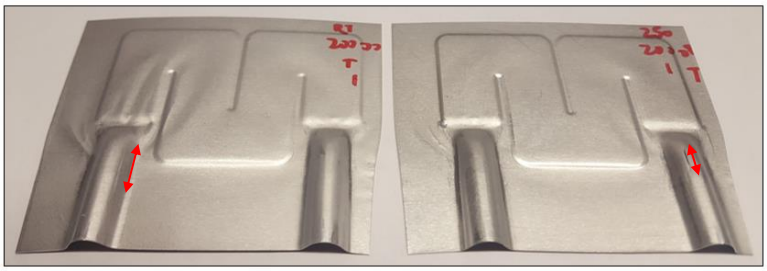

Figure 91: TC3 PF geometry formed with H24-temper sheet at 25°C (left) and 250°C (right) with Teflon lubrication

The effect of punch speed was examined to investigate whether the poor formability at elevated temperature can be attributed to a high punch speed, as shown in other previous studies [8], [12], [41]. Figure 92 shows the PF geometries formed at 250°C with the punch speeds of 0.25 mm/s and 4 mm/s. The negative effect of the punch speed was demonstrated by slightly larger cracks on the specimen formed with the higher punch speed of 4 mm/s. However, the effect was not thought significant enough that the punch speed alone would cause the specimen to fail under warm forming conditions.

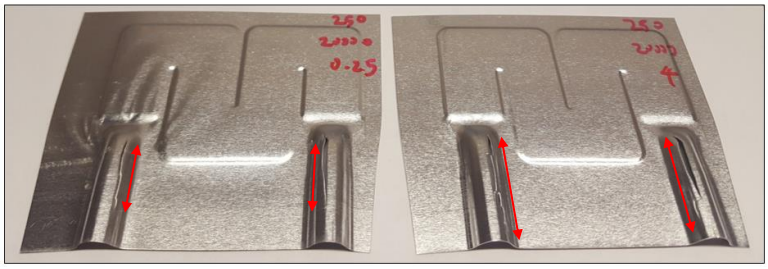

Figure 92: TC3 PF geometry formed with H24-temper sheet at 250C at 0.25 mm/s (left) and 4 mm/s (right)

4.3.1.2 Wrinkling

There was some improvement in the wrinkling behavior with the added channels in theTC3 PF geometry (Figure 93), but there was still a significant level of wrinkling being carried over to the FF geometry which might pose problems in subsequent brazing operations. It was concluded that the wrinkle improvement achieved with the latest tooling configuration was still inadequate.

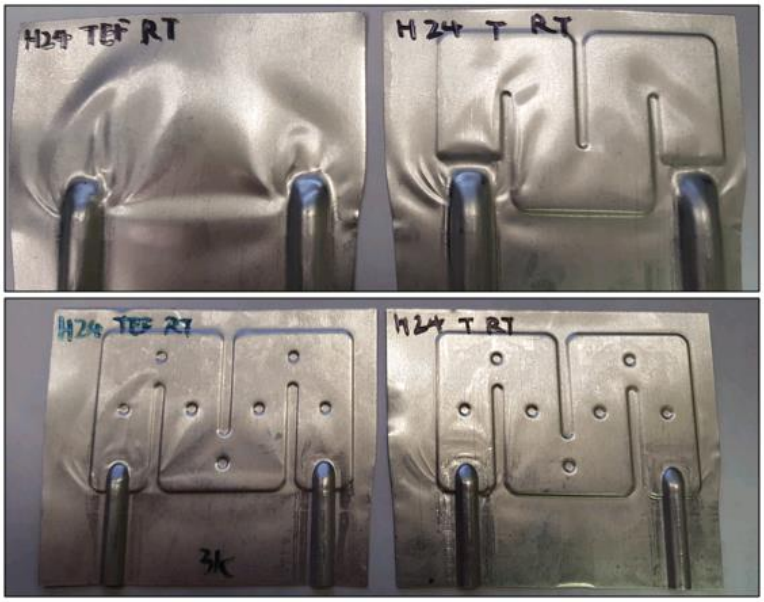

Figure 93: H24 wrinkling behavior for PF and FF geometries formed using TC2 (left) and TC3 (right). PF formed at 25°C and FF formed at 250°C,

4.3.1.3 Snap-through buckling

Another instability appeared on the formed part when the TC3 PF geometry was used as shown in Figure 94. A snap-through buckling, a type of buckling where a structure snaps from one state to

another different state [88], occurred due to high residual compressive stress in the sheet. The two stable equilibrium configurations are shown in the figure. The buckling effect was magnified due to the very thin gauge of the sheet leading to a very low critical load.

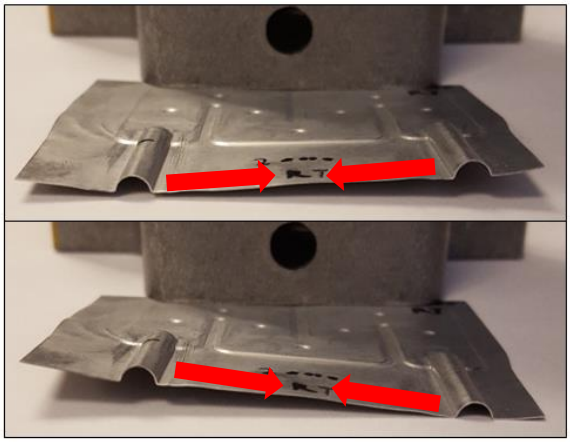

Figure 94: TC3 snap-through buckling of H24-temper formed at 25°C for both PF and FF. A high residual compressive stress in the area shown with red arrows is thought to cause this behavior.

The high residual compressive stress is thought to be caused by the difference in the arc length between the PF and FF I/O port geometries as illustrated in Figure 95. The arc length of the PF geometry was 19.62 mm while that of the FF geometry was 18.41 mm. Therefore, a longer length is compressed into a smaller length during the FF stage leading to high residual compressive stress.

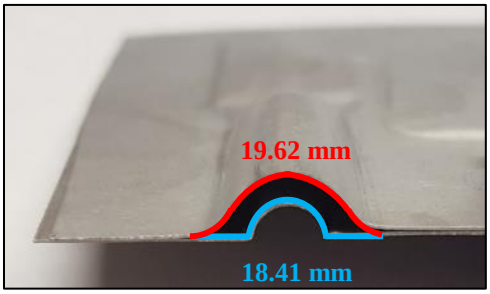

Figure 95: TC3 PF and FF I/O port geometry

This phenomenon was not present in the TC2 multi-stage forming experiments because there was better match of the arc length between the two tooling stages. In the previous experiments, the punch load was reduced due to formability reasons which effectively reduced the arc length of the sheet. Therefore, the residual compressive stress within the sheet after the FF stage was decreased.

In order to further investigate, the TC3 PF geometry was formed with a reduced punch load (3000N) and subsequently formed into FF geometry as shown in Figure 96. It was shown that SHC formed with reduced punch load in the PF stage resulted in less snap-through response.

Figure 96: TC3 PF formed with full punch load (left) and reduced punch load (right) at 25°C then formed to FF at 25°C

The compression effect during forming was also observed in the numerical simulations, as shown in Figure 97. When a trial PF geometry with an arc length of 17.85 mm was formed into FF geometry, the I/O port was stretched rather than compressed since the arc length of FF geometry is 18.41 mm. Therefore, there was no compressive residual stress (thickness increase) around the I/O port. However, the PF geometry used in TC3 has an arc length of 19.62 mm which is considerably larger and led to very high compressive stress around the I/O/ port, as reflected by an increase in the sheet thickness by 24%, which caused the instability problem.

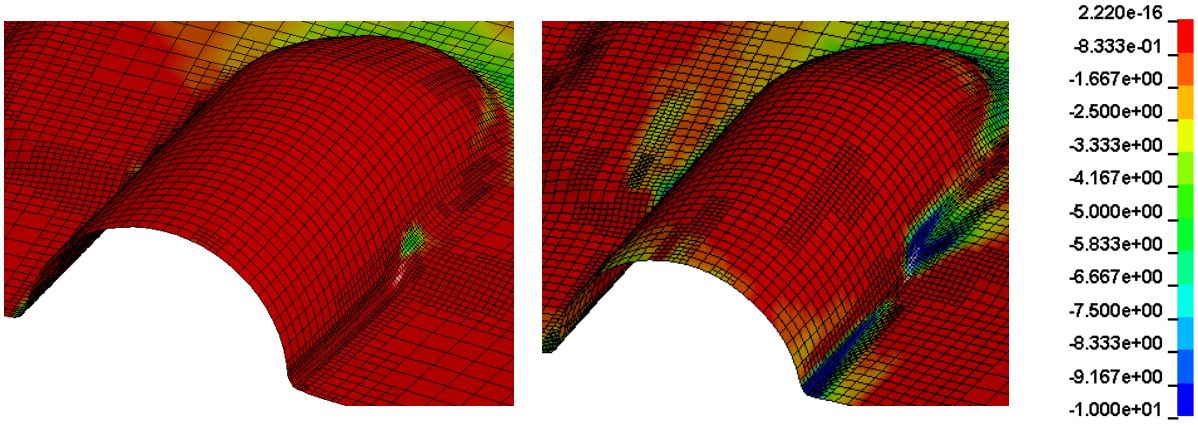

Figure 97: Contour plot of percent thickness reduction of FF geometry, formed after PF with arc length of 17.85 mm (left) and 19.62 mm (right). O-temper, 250°C forming temperature. Note that negative thickness reduction implies thickness increase.

The buckling behavior was no longer observed when the FF geometry was formed at elevated temperatures as shown in Figure 98. The warm forming condition reduced the flow stress and thus

decreased the residual compressive stress within the specimen. This improvement in net shape represents an important benefit of warm forming.

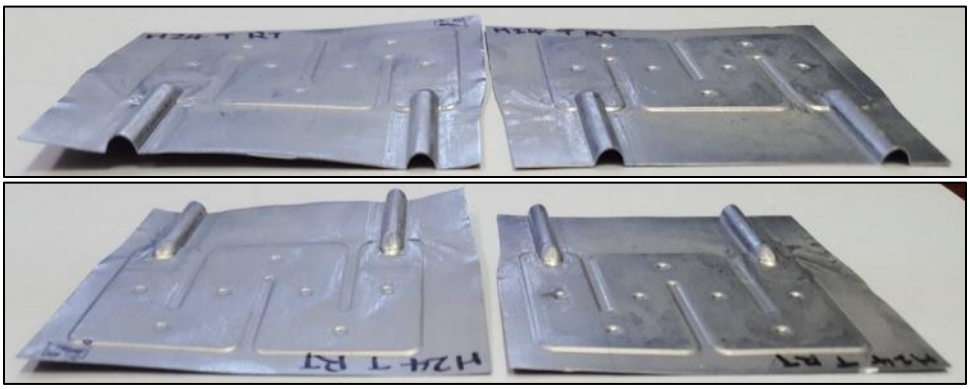

Figure 98: PF formed at 25°C then formed to FF at 25°C (left) and 250°C (right) using TC3

4.4 Tooling Configuration 4 (TC4)

The localization around the I/O port of the SHC is due to severe stretching of the sheet caused by the aggressive geometry, constrained material flow and relatively poor formability of the brazing sheet, particularly in the harder temper conditions. In order to further optimize the manufacturing process, modifications to the blank and tooling design were again considered, including modifications to the I/O port geometries. These improvements actually enabled a single-stage forming process to be performed. The simulation effort was also improved by introducing the constitutive properties presented in Section 3.1.2 for the O and H24-temper sheet, as well as the forming limit diagrams (FLDs) for the brazing sheet alloys developed by Jain [43]. The new property data and forming limit data, in conjunction with thickness reduction predictions, were applied to assess the formability of the surrogate heat-exchanger component (SHC) using TC4.

4.4.1 Preliminary Numerical Simulation

A technique used in industry is the incorporation of a "down-flange" or "dog leg" feature, as seen in Figure 99, to constraint the edge of the blank. This feature incorporates sharp bends along the outer edges of the blank, which resemble the shape of a dog leg, in order to restrict material flow similar to a lock bead. The purpose of this feature is to increase the stiffness of the sheet metal for

better handling and to aid in locating the sheet within the transfer system and progressive die tooling. This feature also locks the sheet during stamping which reduces springback and wrinkling by maintain high sheet tension.

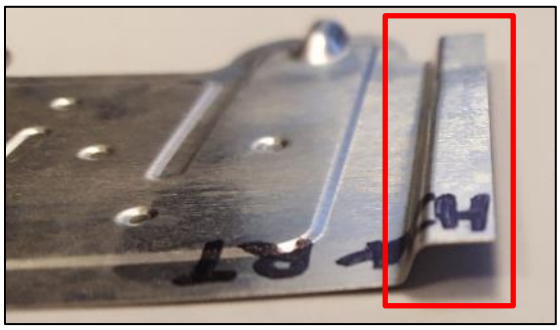

Figure 99: “down-flange” or "dog leg" feature shown in red box

In addition, slight modifications were made to the I/O port geometry to improve the formability while overall shape is maintained, as shown in Figure 100. These modifications are not thought to affect original design intent.

The initial I/O port radius was kept identical and then blended gradually to transition into the cooling channel. This local increase in radius reduced the bending severity during forming while still maintaining a sharp radius for sealing the I/O port joint during brazing at the opening of the I/O port. The formability was found to increase in the simulations as the key dimension, the length over which the I/O port radius is kept identical, indicated by the red arrow in Figure 100 decreased. However, one of the design constraints was to maximize this key dimension since a tight radius is required for the brazing operation in which two SHCs are brazed together with a metal tubing inserted in the I/O ports. It should be noted that the geometrical blending alone was not sufficient to form the part successfully as the feature was still too aggressive to be formed in a single forming step.

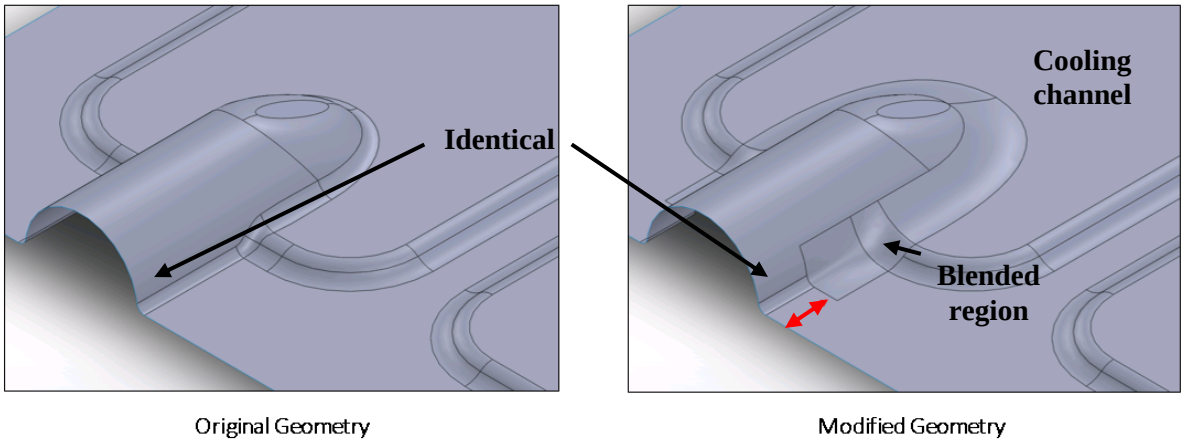

Figure 100: Modified I/O port geometry

Another option to locally increasing the material flow behavior in critical regions was explored by modifying the initial blank geometry. A developed blank geometry was introduce to prevent excessive stretching when the I/O ports are being formed. To do this, a new trim line was defined by offsetting a certain distance from the channels and I/O ports, as shown in Figure 101. The offset distance has to be large enough so that there is still sufficient surface area to be brazed after the material is pulled in during forming. The minimum flange length required after forming was adopted as approximately 1.3 mm, which is the distance between the two adjacent cooling channels as shown in Figure 102. As this length is adequate for the current brazing operation and pressure tests, it was assumed that it would be acceptable to use this length as the minimum criterion.

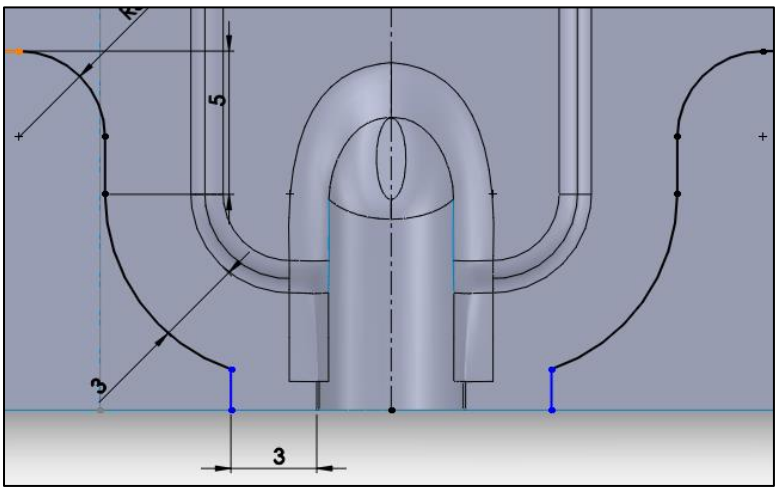

Figure 101: Initial blank geometry trim line with 3mm flange length (offset distance from features).

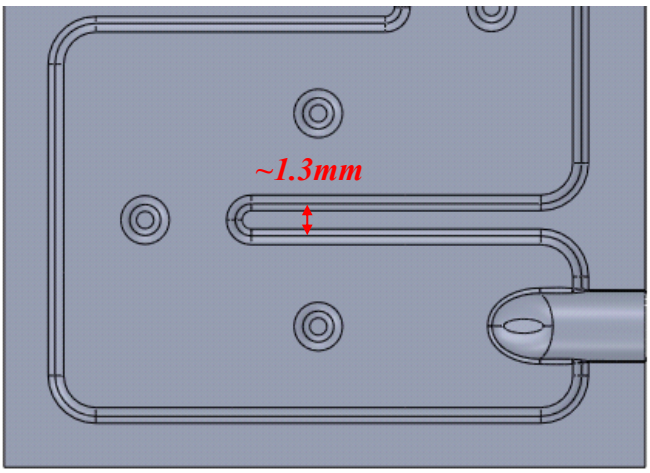

Figure 102: Braze width between two adjacent cooling channels used as minimum criterion for required flange length

Initial blanks with different offset distances were simulated to determine the optimal initial flange width, as shown in Figure 103. The forming limit diagrams are shown in Figure 104. Three different initial flange widths were considered, 2, 3 and 4 mm for which the final width after forming was approximately 0.8, 1.2 and 2.8 mm, respectively. The predictions show that as the initial flange width increased, the formability decreased (increase in thinning) due to the greater resistance to draw-in of the flange to form the I/O port feature. Also, the difference between the initial and final flange width stayed fairly constant at 1.2 mm. The forming limit diagrams predicted that the flange width of 2 and 3 mm would form successfully, while the flange width of 4 mm would fail to form. Although predicted to be safe, the strains in the 3 mm flange width case are in a close proximity of the forming limit curve thus the flange length should be no more than 3 mm.

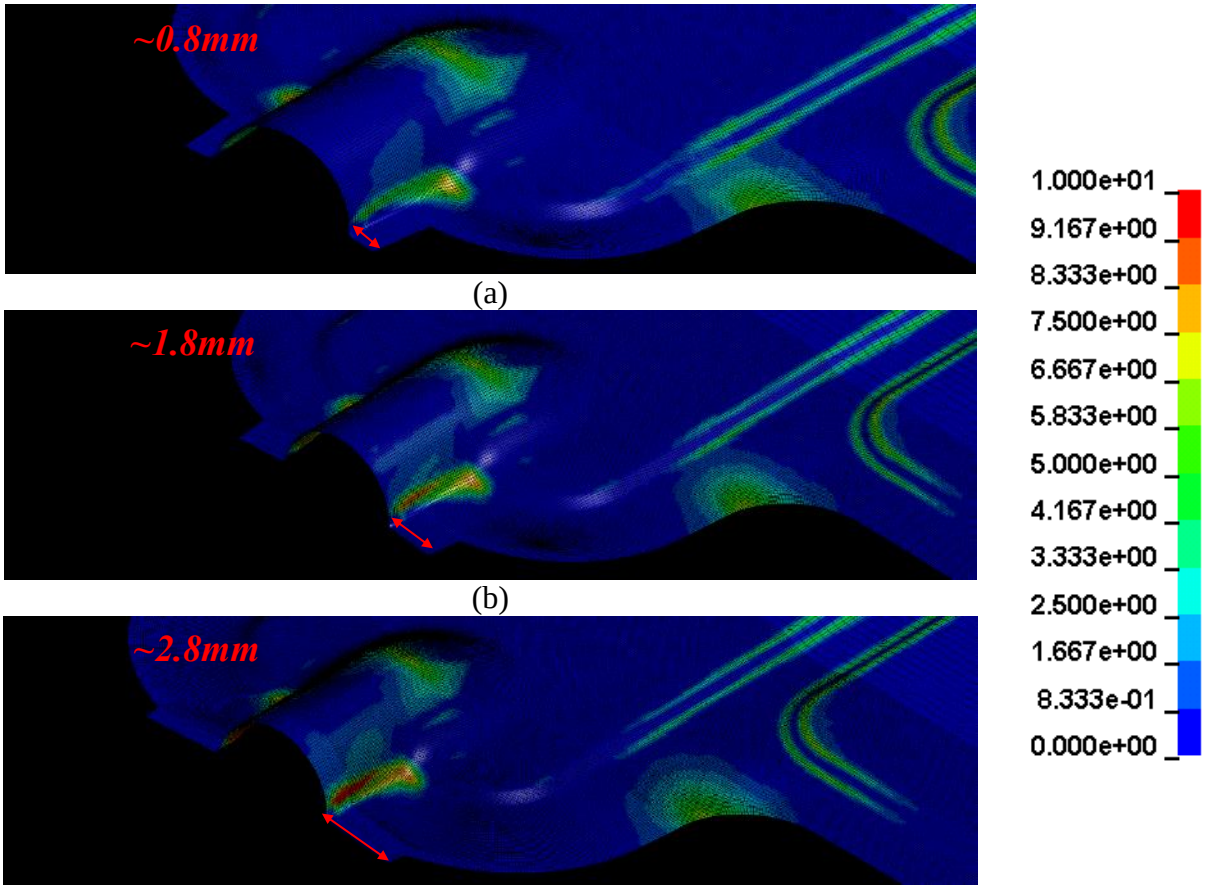

Figure 103: Contour plot of percent thickness reduction for TC4: H24-temper, 250°C forming temperature for initial flange length of (a) 2mm (b) 3mm (c) 4mm

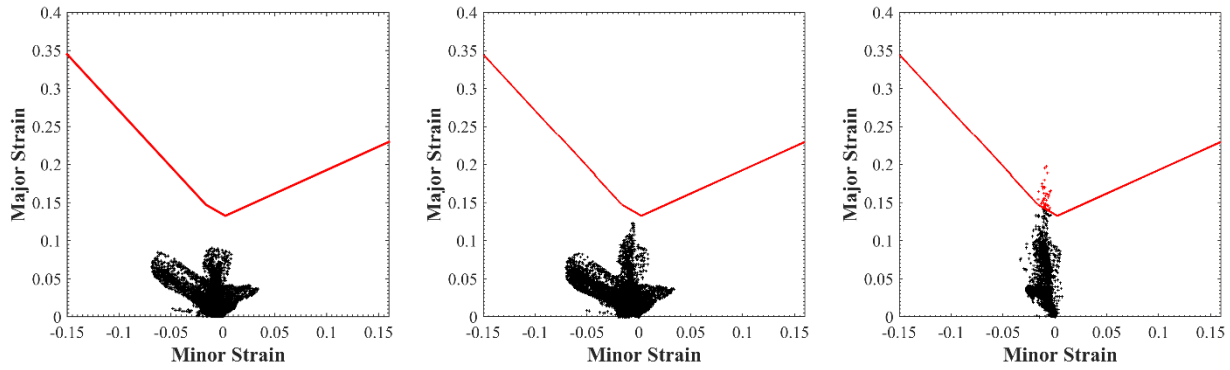

Figure 104: FLDs for TC4: H24-temper, 250°C forming temperature for initial flange length of (a) 2mm (b) 3mm (c) 4mm

Since the minimum final flange length required is 1.3 mm, in order to match the flange width in the interior regions of the SHC (Figure 102), and the flange is drawn in 1.2 mm during forming,

the minimum initial flange width required is 2.5 mm. Therefore, the initial flange width was chosen to be 3 mm in order to be conservative.

4.4.2 Experimental Set-up

The final developed blank geometry adopted in the experiments is shown in Figure 26. Sharp corners were removed to prevent stress concentration by adding fillets. The blank was produced using CNC machining with the aid of jig fixture shown in Figure 105. Approximately 5 to 10 rectangular blanks were stacked and then clamped to the jig surface, after which the final profile was machined.

Figure 105: Blank machining jig for TC4

The CAD of the TC4 dies are shown in Figure 106 and Figure 107. The TC4 forming die is very similar to the die used in the other tooling configurations. An additional feature included in the design was the dog leg feature explained previously. This feature comes in contact with the blank first, bends the sheet, and effectively locks it in place.

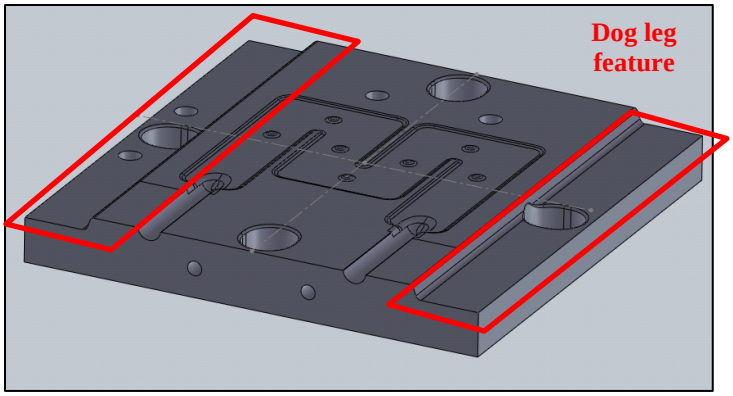

Figure 106: CAD of female die for the TC4

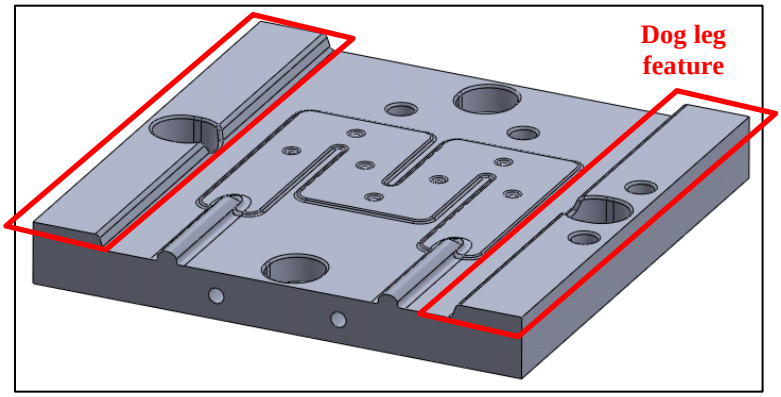

Figure 107: CAD of male die for the TC4

4.4.3 Experimental Results

The experimental results for the TC4 forming experiment are summarized in Table 15. The Fuchs lubricant was no longer considered as it had negligible performance difference from the Teflon spray which has a more consistent surface quality and greater ease of application.

Table 15: TC4 forming experimental results (O = formed successfully X = fracture occurred Δ = necked)

Temper	Temperature	None	Teflon
O	RT	O	O
	250	O	O
H22	RT	O	O
	250	Δ	O
H24	RT	O	O
	250	Δ	O

The SHC formed successfully in a single forming operation even with the hardest material, the H24-temper, as shown in Figure 108. With the TC4 I/O port geometry and blank geometry, the formability increased significantly enabling forming at room temperature without lubricant. In addition, the snap-through buckling observed in TC3 was no longer present.

Figure 108: SHC formed with H24-temper sheet at 25°C (left) and 250°C (right) using TC4

As seen previously, the issue associated with forming at elevated temperatures was observed again. The SHC formed at 250°C with the H22- and H24-temper material without lubricant had noticeable necking around the I/O port causing severe thinning, as shown in Figure 109. The component did not fracture completely but the severe thinning is unfavorable for component durability and corrosion resistance. The necking was not observed with the use of lubricant. The cause for this necking at elevated temperatures is suspected to be the increasing coefficient of friction with temperature as shown in Figure 33.

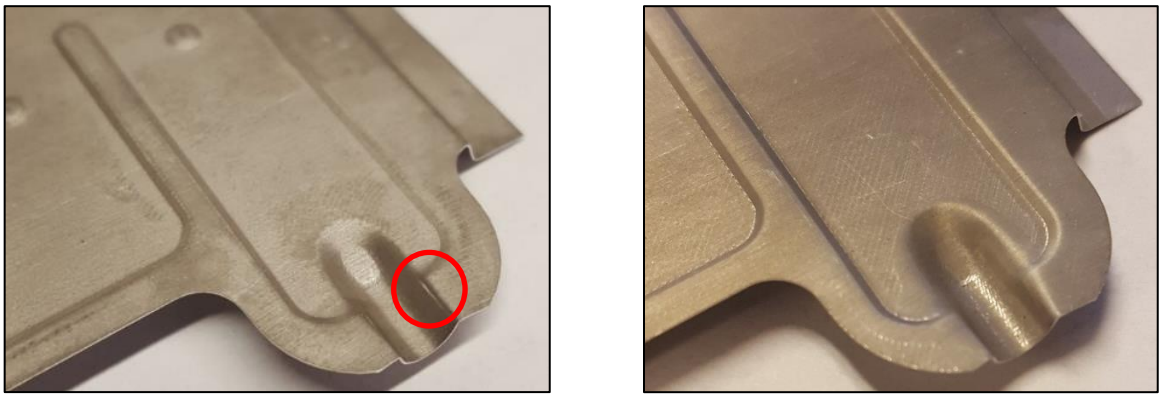

Figure 109: H24-temper material formed at 250°C without lubricant (left) with Teflon lubricant (right)

It was observed that the SHCs formed with the TC4 are superior in terms of formability and wrinkling behavior compared to the previous tooling designs. In addition, the ability to form these parts in a single forming step offers considerable process efficiency compared to multi-stage forming. Initially, the target warm forming temperature was aimed at 250°C as higher temperatures would increase the risk of adverse thermal effects on the strength of the material and coating integrity. The SHCs formed with TC4 at 250°C displayed some improvement in the springback behavior but the reduction was not high as anticipated. Therefore, the springback behavior at higher temperatures up to 350°C was further investigated. The high forming temperatures coupled with high punch loads resulted in significant reduction in springback. All of the subsequent in-depth springback analysis presented in this thesis was performed on the SHCs formed with the TC4 (see Chapter 5).

4.5 Summary

This chapter has presented the development process for warm forming tooling by combining numerical and experimental methods. Four different tooling configurations that incorporate various die designs and process parameters were developed in order to improve part formability and wrinkling behavior. Through TC2 and TC3, it was demonstrated that multi-stage forming is quite effective in distributing strains to prevent localization such as the one seen around the I/O port in TC1 that utilized single-stage forming. However, it was shown the multi-stage forming could potentially introduce part defects such as wrinkling and snap-through buckling. The first

stage of TC3 included channel geometries in attempt to reduce wrinkling but it was found to be ineffective. The greatest formability gain was achieved in TC4 due to the developed blank geometry that minimized material constraint and provided ease material flow into the I/O port. The developed blank prevented excessive stretching of the sheet while maintaining enough surface area to be brazed after the material is pulled in. In conjunction with the minor reduction in geometrical sharpness of the I/O port-cooling channel intersection, the SHC exhibited significant improvement in formability that allowed forming at room temperature without any lubricants in a single operation. The anticipated formability gain associated with warm forming was not observed and, in reality, the opposite effect was shown in which the parts exhibited more necking at elevated temperatures. The poor formability at elevated temperatures is speculated to be caused by the increase in coefficient of friction. Throughout all the tooling configurations, no observable evidences that support warm forming in terms of formability were found. However, the beneficial effect of warm forming was observed when the parts formed at elevated temperatures displayed reduced springback. More in-depth investigation regarding the effect of warm forming on springback is completed in the next chapter.

5 Springback

In order to fully characterize and to gain in-depth knowledge about the springback behavior, the effects of a wide range of experimental parameters on springback were considered, as shown in Table 16. These included both process and material dependent variables that could potentially influence springback. The effect and sensitivity of each parameter on the springback behavior was evaluated thoroughly. Note that the holding time is to the duration of time at which the formed component is held within the closed dies. The sheet direction refers to the sheet direction (rolling versus transverse) aligned with the length of the component during forming, as shown in Figure 110.

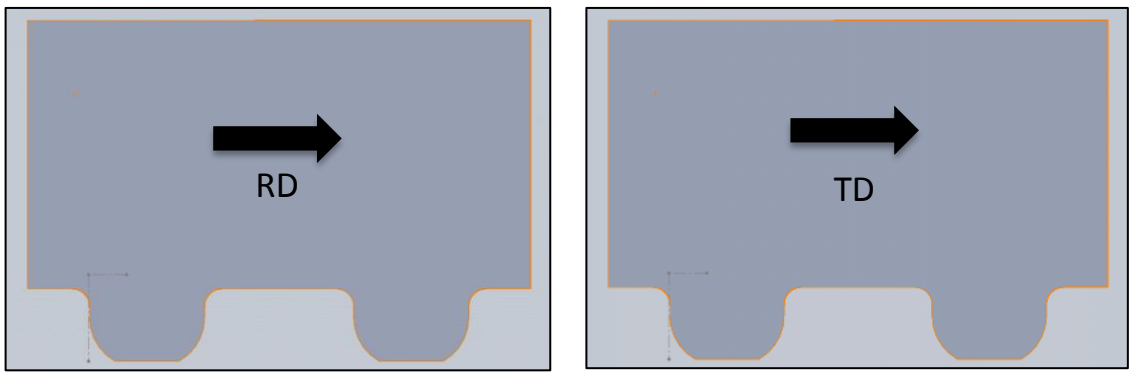

Figure 110: Rolling and transverse directions relative to blank

The normal and inverted sheet orientations refers to the SHCs formed with the core layer on top and bottom surfaces, respectively. As previously mentioned, only the SHCs formed with tooling configuration 4 (TC4) were used in the springback analysis. For all of the springback experiments, each test condition was repeated at least three times and the scatter bands correspond to one standard deviation.

Table 16: Single-stage springback experimental parameters

Material Temper	Temperature (°C)	Lubricant	Forming Speed (mm/s)	Punch Load (kN)	Holding Time (s)	Sheet Direction	Sheet Orientation
O	25, 250	None	1	10	2	RD	Normal
H22	275, 300	Teflon	10	30	30	TD	Inverted
H24	325, 350			80			

5.1 Springback Measurement

In order to analyze the springback behavior, a method to quantify springback had to be developed. Springback was characterized in terms of the out-of-plane displacement and curvature of the cross-section of the formed part. A simple jig (Figure 111) was designed and machined to fixture the component in a consistent manner to serve as a reference in measuring springback. It clamped down the SHC on the channel such that the clamped side of the component was horizontal. The jig constrained the part and removed any unnecessary degrees of freedom for meaningful and consistent measurements which would also be useful for validation of the springback numerical models. After the SHC is loaded on the jig, the edge of the as-formed parts were scanned on a flatbed scanner in a dark room to create a greyscale image with high contrast.

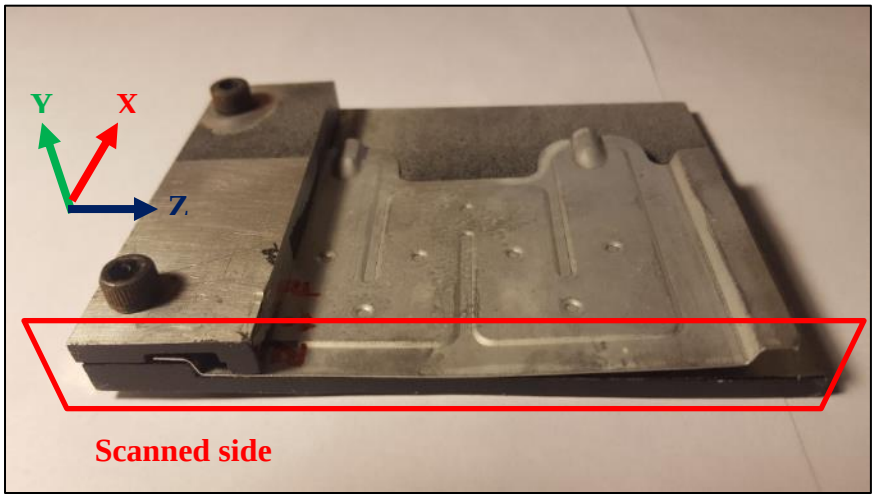

Figure 111: Springback measurement jig with SHC in position used for springback measurement

A MATLAB script was created that utilized image processing to automatically measure springback (y-displacement) and curvature of the component from the scanned greyscale images. Figure 112 shows the scanned and processed images of the part. The image processing consisted

of converting a greyscale image into a binary image and applying built-in filtering and morphological operations. The curvature of the component was obtained by fitting a circle to the cross-section excluding the side walls. The vertical displacement was defined as the distance from the intersection of the line segments fit to the side wall and the tangent to channel bottom tangent to a horizontal reference plane.

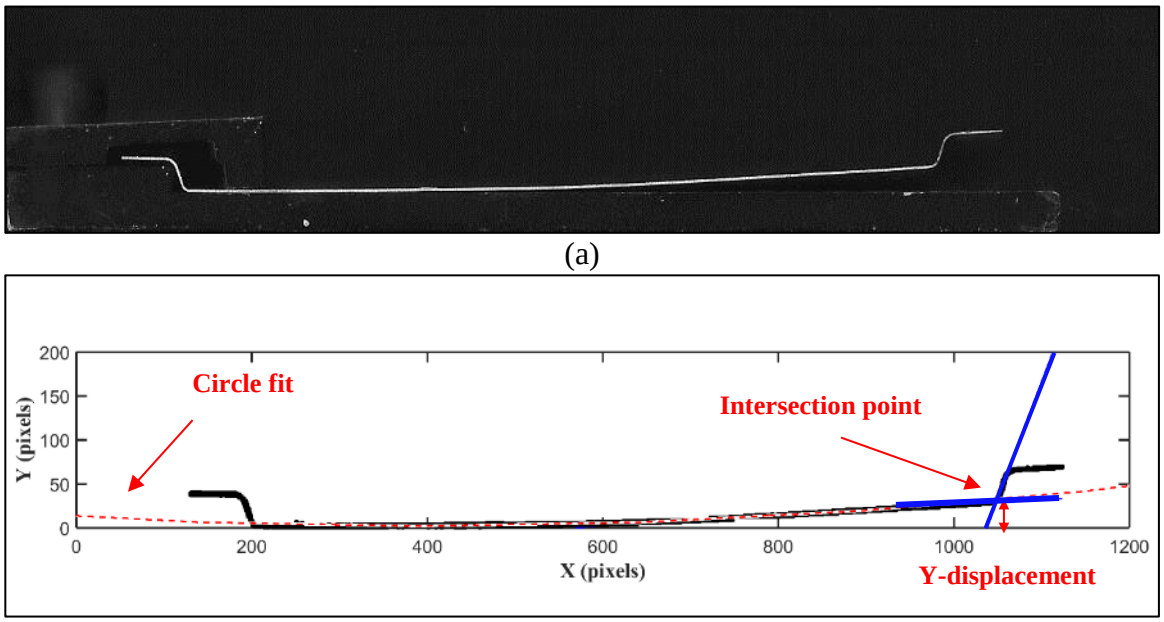

Figure 112: (a) Scanned raw image (b) Processed image with detected y-displacement and curvature

5.2 Measured Springback Behavior

5.2.1 Effect of Forming Temperature and Material Temper

The measured springback results for the three tempers at different temperatures are presented in Figure 113. The forming was done using a punch speed of 1 mm/s and an unlubricated condition. As noted before, slight necking occurred at the I/O port region for the parts formed at elevated temperatures, which should not affect the macro springback of the components. The red horizontal dashed line indicates the springback values for O-temper sheet formed at room temperature and serves as a reference against which the effect of forming temperature and material temper can be assessed.

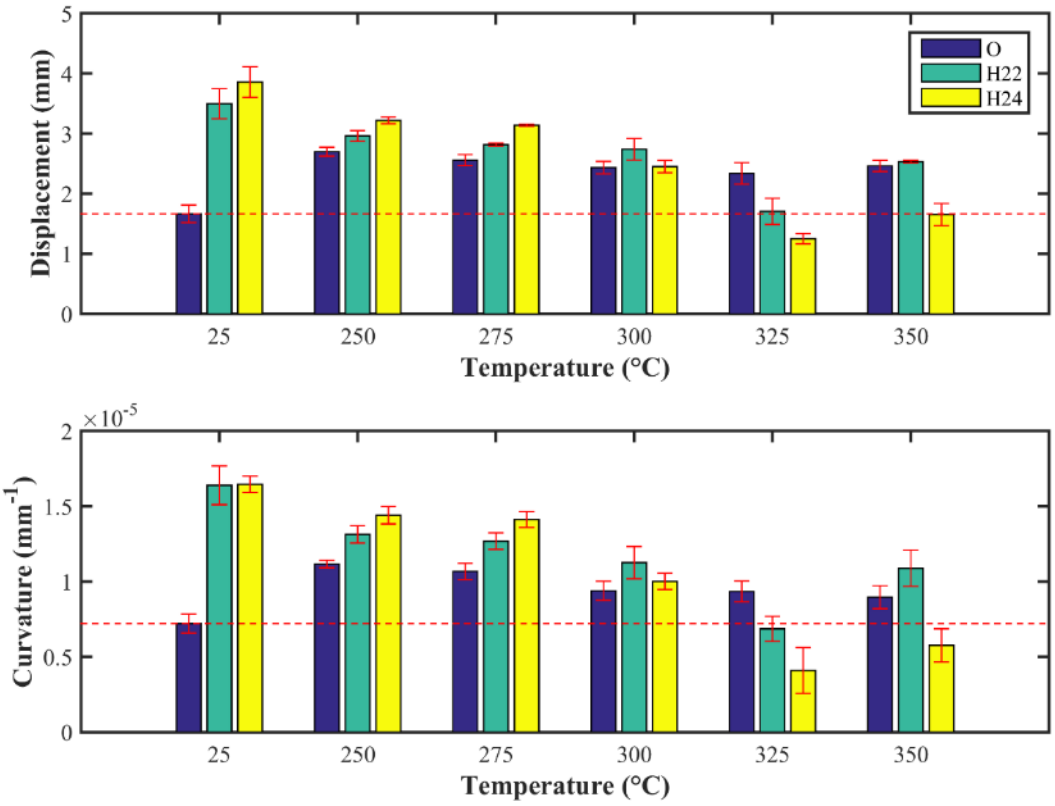

Figure 113: Effect of temperature and material temper on springback for TC4 with 10kN punch load and 2 second holding time at dry condition

The effect of temper is quite evident in the room temperature results which show increased deviation from nominal geometry (springback) as the temper (hardness) is increased. This can be attributed to the increased amount of work hardening, higher residual stresses and dislocation densities in the higher temper materials introduced during fabrication of the sheet. For the O-temper condition, the springback actually increased with elevated temperature for all of the temperatures considered. The increase in springback with temperature for the O-temper material was attributed to the decreasing elastic modulus. As temperature increases, the strength of the material is reduced but the elastic modulus is reduced as well. However, the O-temper material is already in the fully annealed condition hence the reduction in strength with increasing temperature is not as significant as for the harder tempers. Therefore, the reduction in elastic modulus was greater than the reduction in strength which caused an overall increase in springback which is proportional to the strength-to-elastic modulus ratio. The approximate strength-to-elastic modulus

ratios at different temperatures for the three tempers are shown in Figure 114. The yield strengths were obtained from the tensile tests by Verma [73] and elastic moduli were obtained from Omer [89]. It is observed that the ratios actually increase for O-temper while they decrease for harder tempers with increasing temperature, which agree with the springback results.

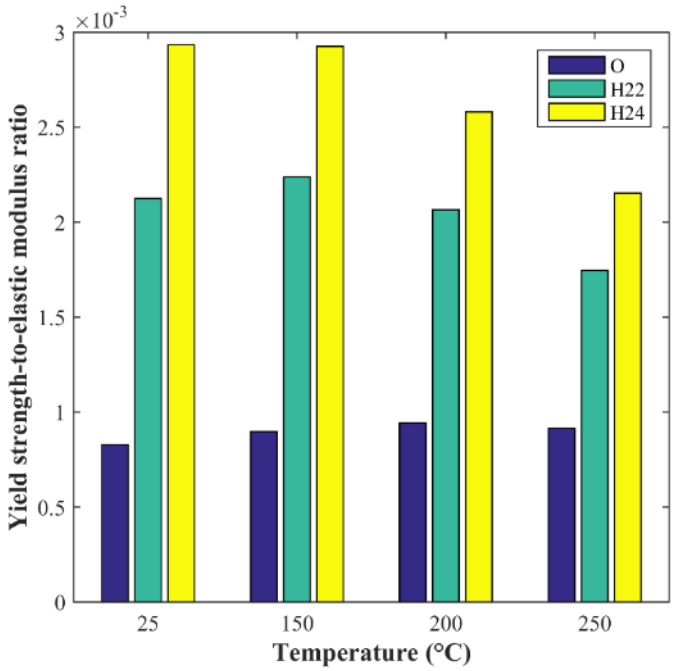

Figure 114: Yield strength-to-elastic modulus ratios for O-, H22- and H24-tempers at different temperatures

For the two harder tempers (H22 and H24), the increased forming temperature was beneficial and the results show a decrease in springback. The relative ranking of the springback exhibited by the three tempers is relatively constant up to 275^0C. For the highest forming temperatures considered ($300\text{-}350^0$C), the extent of springback is similar to that of the O-temper room temperature material.

5.2.2 Effect of Lubricant

The introduction of a lubricant had a minor adverse effect on the springback of the H24-temper at both room and elevated temperatures as shown in Figure 115.

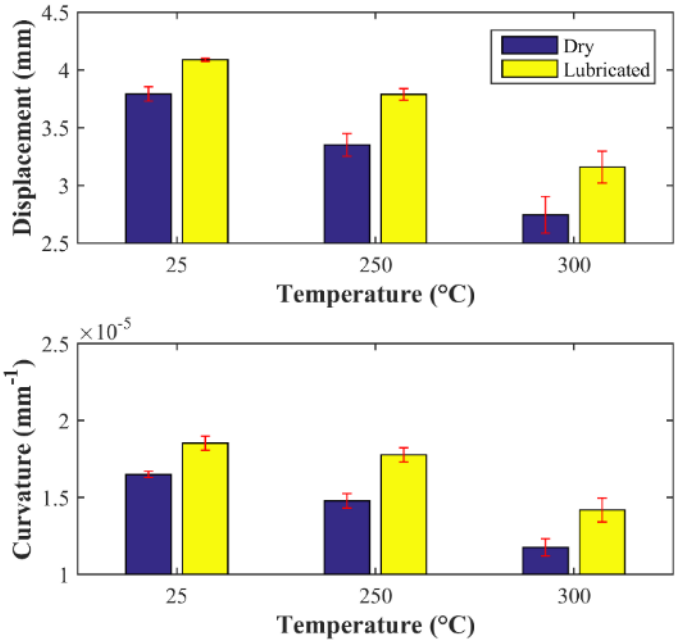

Figure 115: Effect of Teflon lubricant on H24 springback for TC4 with 10kN punch load and 2 second holding time

The difference in springback between the dry and lubricated conditions increases with temperature which is likely caused by an increase in coefficient of friction with temperature in the dry condition, shown previously through the friction characterization (Figure 33). Similar results are found in the literature as well [90]. A lower coefficient of friction tends to reduce membrane tension within the blank so that internal bending moments are higher, resulting in a mild increase in springback. However as shown in the previous chapter, the formability increase gained by the use of lubricant outweighs the minor increase in springback.

5.2.3 Effect of Forming Speed

Figure 116 shows the effect of forming speed on the H24-temper springback. As expected, the forming speed only affected the springback at elevated temperature due to the increased strain rate sensitivity (Figure 20), as shown previously in the tensile test results by Verma [73]. At low speed and elevated temperature, there is a reduction in springback relative to room temperature conditions, however, this benefit is reduced at higher punch speeds. Therefore, in order to minimize springback, the punch velocity should be kept low.

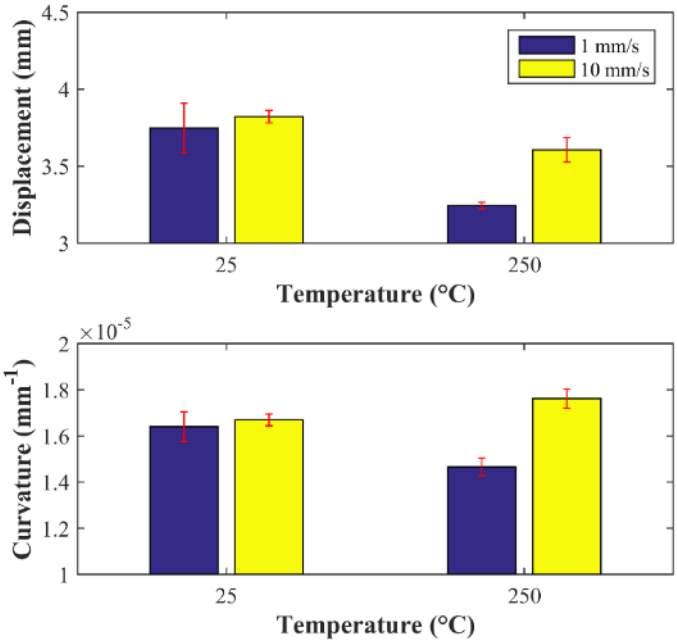

Figure 116: Effect of forming speed on H24 springback for TC4 with 10kN punch load and 2 second holding time at dry condition

5.2.4 Effect of Coil Set

Brazing sheet is delivered in the form of coils and, as a result, the blanks had an initial curvature known as coil set, as seen in Figure 117. Coil set is a phenomenon in which the metal strip retains a residual curvature even after the strip is removed from the coil. An apparatus called a sheet straightener, which applies mild cyclic bending and unbending deformation to the sheet to remove coil set, is usually used in industry.

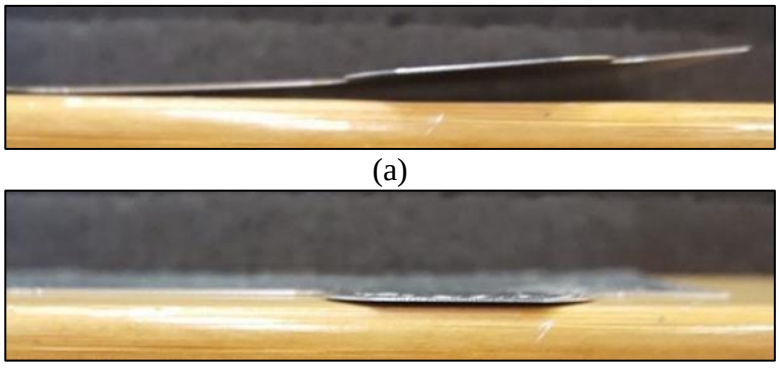

(a)

(b)

Figure 117: (a) As-received sheet (b) Straightened sheet

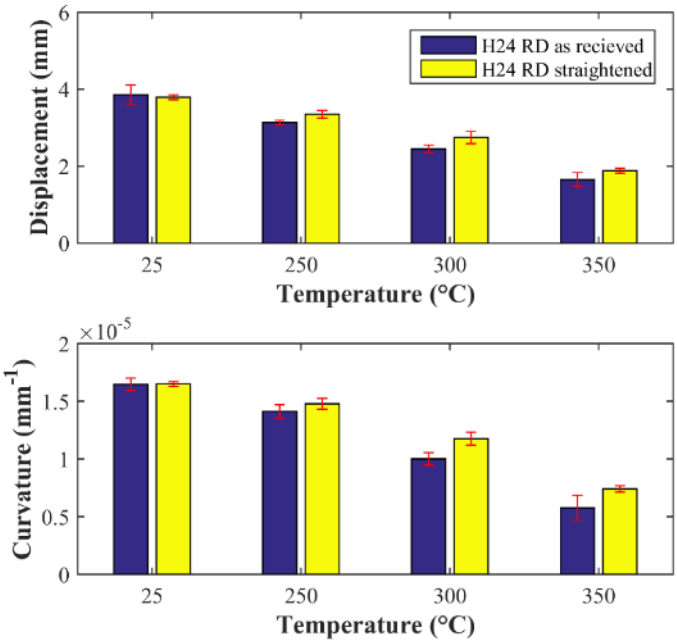

Figure 118: Effect of coil set on H24 springback (Dry conditions) for TC4 with 10kN punch load and 2 second holding time

In order to ensure that the initial coil set does not have an effect on the final springback, the springback was measured from the parts made with the sheets that were fed through a straightener. The results are presented in Figure 118 and demonstrates that the initial coil set has no effect on the final springback at each temperature condition considered. Due to the extremely thin sheet used in the current work, even a very small amount of residual stress and plastic strain can cause significant and exaggerated curvature. However, the stresses and plastic strains associated with the forming process are much higher than those associated with the coil set, such that coil set has a negligible impact on the final springback.

5.2.5 Effect of Sheet Direction

Due to the crystallographic texture induced by the rolling process, sheet metals can exhibit significant anisotropy. Therefore, the effect of sheet direction (anisotropy) was studied by forming the SHC in two different directions in which the length of the blank is aligned with either the rolling or transverse directions as shown in Figure 110. The springback results are summarized in Figure 119. It was observed that anisotropy has no effect on the room temperature springback and

only a very small effect at elevated temperature. This indicates that the particular brazing sheet used in the current study has only a mild degree of planar anisotropy. Thus, for the balance of the experiments in this thesis, the rolling direction is aligned with the length of the blank.

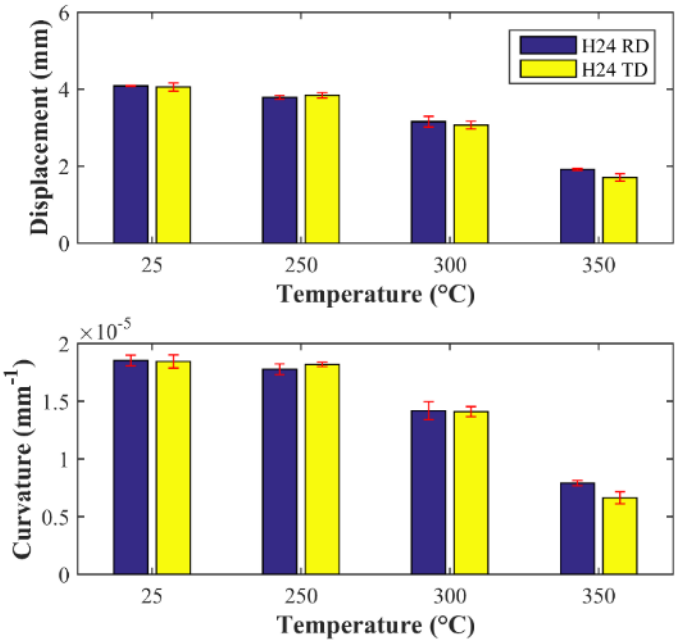

Figure 119: Effect of anisotropy on H24 springback (Teflon lubricated) for TC4 with 10kN punch load and 2 second holding time

5.2.6 Effect of Sheet Orientation

Normally, the SHC is oriented prior to forming such that the core side is located at the top surface of the component. It was observed that if the SHC was formed with the inverted sheet orientation (clad layer as top surface), there was a significant reduction in springback, as shown in Figure 120. Initially, the coil set was suspected to be the cause of the springback reduction as the curvature of the coil set works against the springback at the inverted orientation. However, it was concluded above that the coil set has negligible effect on the springback behavior. The friction gradient between the top and bottom surfaces was also considered as a potential cause, but the components formed with the use of lubricant still exhibited the same behavior. Another suspected cause was the strength gradient between the two layers. Due to the strength gradient, the neutral axis is no longer aligned with the sheet mid-plane thus the stress distribution after bending and springback would be asymmetrical with respect to the mid-plane. Therefore depending on the sheet orientation,

the springback behavior would be different. This effect is examined more closely in Section 6.1.1 in which a numerical model of springback is presented. The observations in Figure 120 are consistent with those of Hino *et al.* [91], who characterized the springback behavior of a sheet metal laminate consisting of aluminum and stainless steel. They found that the springback behavior is strongly affected by the strength difference between the laminate layers and the relative position of the layers.

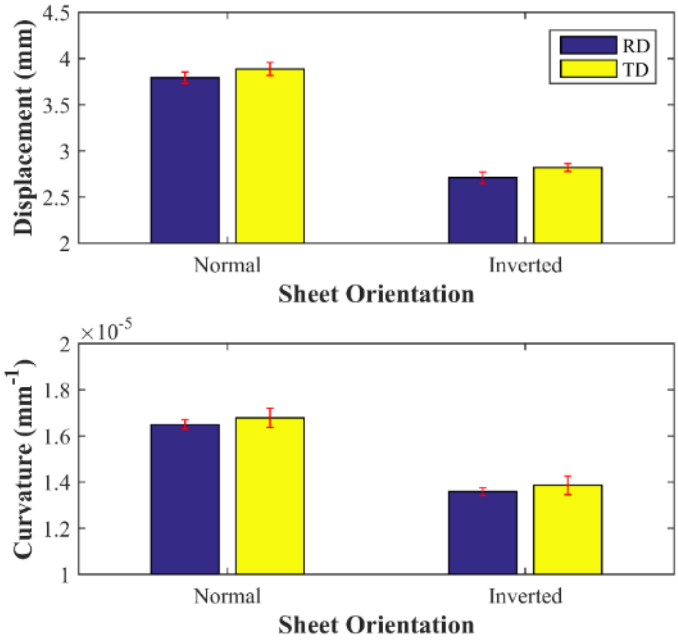

Figure 120: Effect of sheet orientation on H24 springback at 25°C (Dry condition) for TC4 with 10kN punch load and 2 second holding time

5.2.7 Effect of Punch Load and Holding Time

It was observed that as the punch load increased, the springback decreased significantly, as shown in Figure 121. The springback reduction was attributed to through-thickness deformation known as bottoming or coining. The through-thickness deformation leads to high localized compressive stress and plasticity in bend regions which reduces the residual bending stresses and resulting springback. A similar trend was observed in the studies done by Leu *et al.* [92] and Forcellese *et al.*[93].

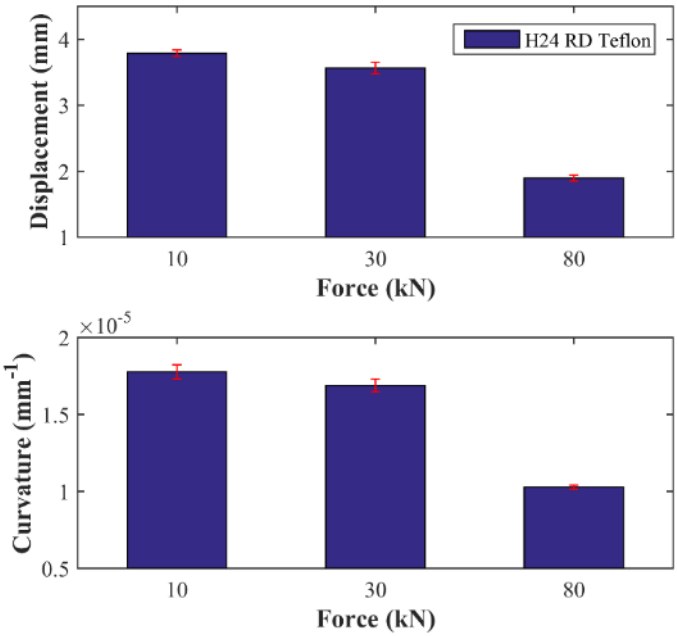

Figure 121: Effect of punch load on H24 springback at 250°C for TC4 with 2 second holding time and Teflon lubricant

The effect of punch holding time was investigated by holding the formed SHC under the punch load (10kN) for an extended duration. The springback decreased significantly and the effect seemed to saturate beyond a holding time of 30 seconds, as shown in Figure 122. Vickers micro-hardness tests were performed to determine whether recrystallization occurred due to the longer exposure to elevated temperatures. The results from the Vickers micro-hard tests (Figure 123) show that there was no permanent reduction in the material strength. It was speculated that the long exposure time to elevated temperature allowed for temporary dislocation movement and realignment which led to further stress relaxation from warm forming. Consequently, the elastic unloading after release from the die occurred at the lower stress level resulting in decreased springback and the strength was regained when the component cooled down to room temperature.

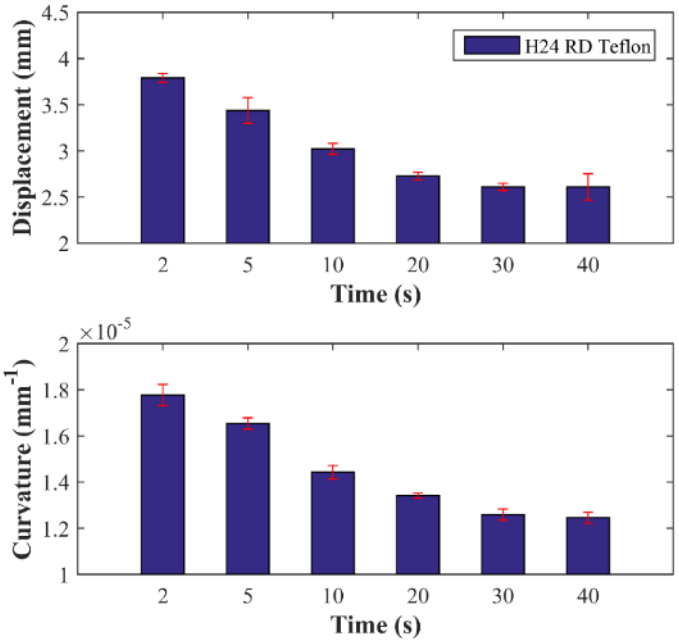

Figure 122: Effect of holding time on H24 springback at 250°C for TC4 with 10kN punch load and Teflon lubricant

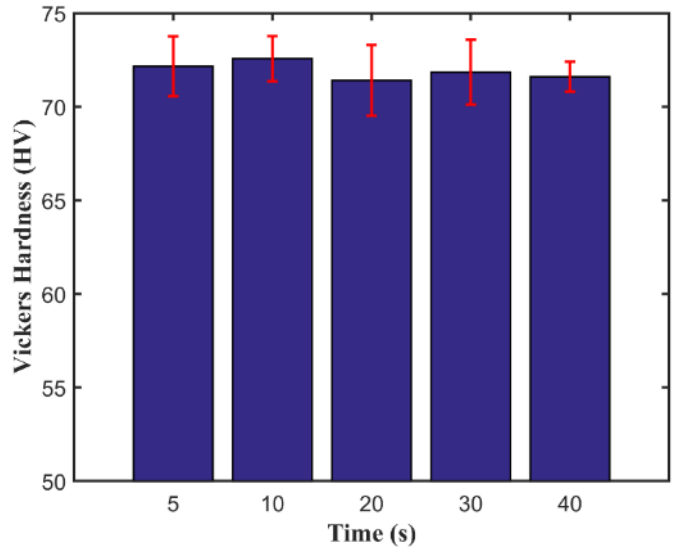

Figure 123: Effect of punch holding time on Vickers hardness for TC4 with 10kN punch load and Teflon lubricant

The final results that consider the combined effect of increased punch load and holding time are shown in Figure 124. The red dotted line indicates the springback values for O-temper at room temperature formed with 10 kN punch load. The red solid line represents the identical condition except it was formed under 80 kN punch load. These two red lines serve as a benchmark/control

measurement against which the effect of warm forming on harder temper materials can be compared. It is shown that punch load and holding time have significant impact in reducing springback, particularly at elevated temperatures. The effect of punch load is observed to be magnified with increasing temperature as thermal softening allows more coining to occur. The effect of holding time seems to be diminishing with increasing temperature as there was no difference in the springback values at 350°C between the two holding times. Furthermore, the holding time of 30 seconds would not be feasible in the actual industrial process since a low cycle time is essential. When the low punch load was used, the H24-temper obtained springback values that are similar to that of the O-temper if a sufficiently high forming temperature was used. However with the use of high punch load, the springback values for the O-temper decreased practically to zero thus, the H24-temper was no longer able to obtain similar springback results as the O-temper.

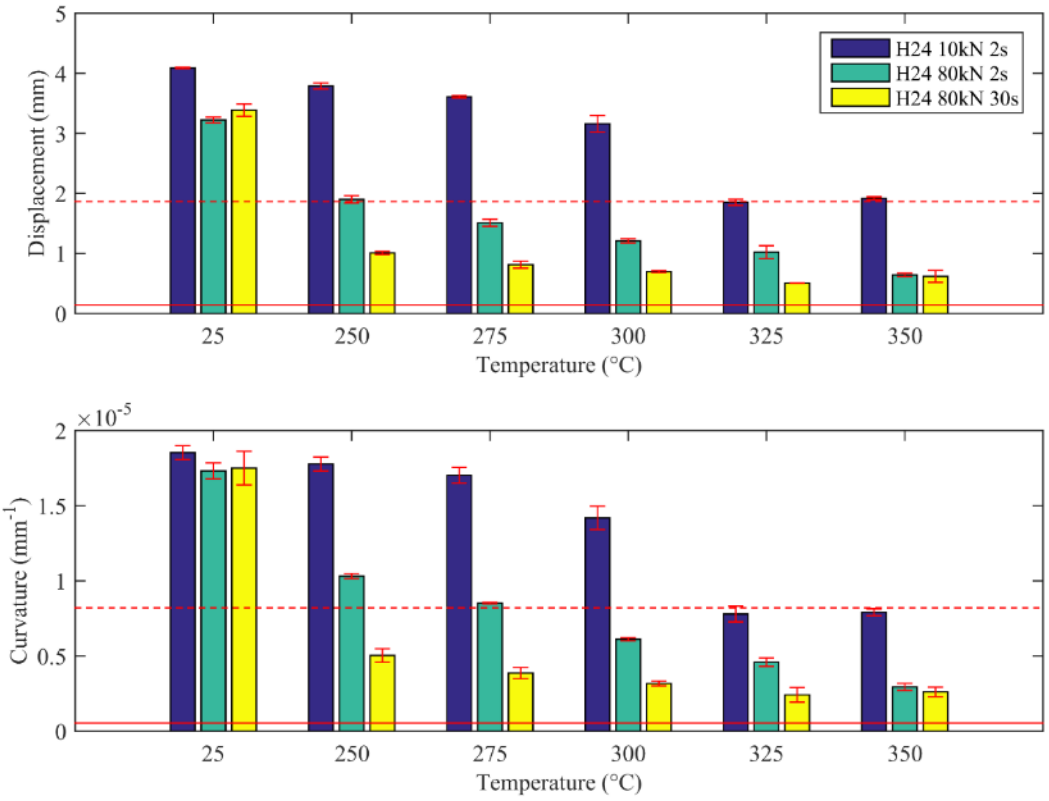

Figure 124: Effect of punch load and holding time on H24 springback (Teflon lubricated) for TC4. Red dotted line indicates O-temper formed at 25°C with 10kN punch load. Red solid line indicates O-temper formed at 25°C with 80kN punch load

Although the reduction in springback for the H24-temper was not able to surpass the O-temper springback results, it was shown that warm forming is still a very effective method in reducing springback. A maximum reduction of 88% was observed at 325°C when high punch load and holding time were used. Brazing tests will be performed in future work to determine the required reduction in springback for the SHCs that allows them to be brazed successfully.

5.2.8 Effect of Thermal Expansion Gradient

When the blanks were placed on the hot dies during the heating stage, a sheet curling effect was observed as shown in Figure 125. It was determined that this phenomenon is caused by a "bimetallic strip" effect. A bimetallic strip consists of two different metal strips with different thermal expansion coefficients bonded together. Therefore when the sheet is heated, one of the two metals expand at a higher rate causing the strip to bend or curl. The sheet studied in the current work also consists of two different aluminum alloys (AA3003 and AA4045) and their coefficient of thermal expansion are reported to be 23.2×10^{6} and 21.05×10^{6} K^{-1}, respectively [94]. These values are consistent with the observed behavior in that the sheet bends towards the clad side which has the lower coefficient of thermal expansion. The curling effect was no longer observed when the clad layer was removed (by polishing) which validates the source of the curling as differential thermal expansion gradient between the two alloys.

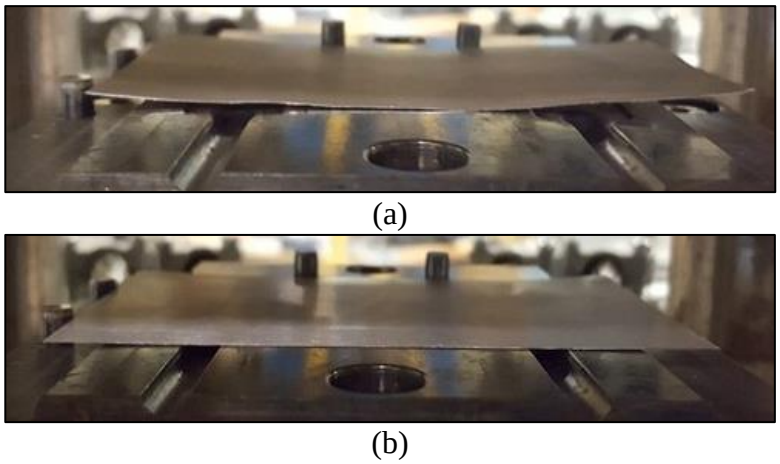

(a)

(b)

Figure 125: Thermal effect at 250°C for (a) brazing sheet with clad layer on top and (b) brazing sheet with clad layer removed

When the SHCs are formed at elevated temperatures and cooled down to room temperature, thermal contraction is observed as well. The thermal contraction adds to the part geometric distortion since the top of the component contracts more and causes the component to curl upwards. This effect is another reason why the SHCs formed with the inverted sheet orientation exhibit lower part geometric distortion (see Figure 120). With the inverted orientation, the clad side with the lower coefficient of thermal expansion is at the top of the component which decreases springback by curling downwards. The thermal expansion gradient must be accounted for in the numerical simulations to capture the expansion and contraction effects in order to accurately predict the final springback at room temperature (see Section 6.1.2).

5.3 Summary

This research presented in this chapter provides useful insight into different experimental/material parameters and their effects on springback. The effect of temper was evident since strength is directly correlated to springback. Temperature, the driving mechanism of warm forming, had somewhat lower than expected effect at intermediate temperatures (250-275°C) thus higher temperature were required. However, the effect of temperature coupled with increased punch load and holding time offered significant improvement in springback behavior even at 250°C, successfully demonstrating the potential of warm forming. The bi-metallic nature of the sheet had an interesting effect on springback through the differences in thermal expansion coefficients and strength between the two metal layers. The punch speed and lubrication had minor adverse impact on springback while sheet direction and coil set had no observable effect.

6 Springback Simulation

In an effort to develop predictive models of part springback after forming, springback simulations were performed considering the TC4 experiments using the non-linear static implicit formulation in LS-DYNA. In these models, the results of the forming simulation were used to initialize the springback model. Typically, the output of the forming simulation contains the deformed geometry, associated internal stresses, strains and thinning. The static implicit solver calculates the unloaded configuration that satisfies the force equilibrium conditions.

Two types of springback simulations were developed. The first utilized the shell-based forming simulations presented in Chapters 3 and 4. In addition, solid element-based models were developed in an effort to capture the through-thickness compression (coining) effects that were thought to be operative under the higher tooling load cases reported in Chapter 5 (Section 5.2.7). Solid element-based forming models are generally avoided whenever possible due to high computational cost (compared to shell element models), however, in this work, it proved difficult to capture coining using shells.

6.1 Springback Models

6.1.1 Material Model for Springback

For most springback simulation, the material behavior is purely elastic thus only Young's modulus and Poisson's ratio are required. Commonly, an elastic material model (*MAT_001) is used since the part is simply unloaded elastically and simulations are performed isothermally with constant elastic modulus at the temperature of interest. The elastic moduli at different temperatures were obtained from Omer [89] and approximated as a linear function of temperature. The elastic moduli used in the simulations are summarized in Table 17.

Table 17: Elastic moduli at different temperatures

Temperature	25°C	250°C	300°C	350°C
Elastic Modulus (MPa)	70,155	48,079	43,173	38,267

In the current warm forming work, several different phenomenon observed during the experiments had to be account for in an effort to accurately predict the springback behavior, including thermal expansion effects and the differences in strength between the core and clad layers.

One unusual aspect of the brazing sheet material studied herein is the different thermal expansion coefficient values associated with the AA3003 core versus the AA4045 clad layers. This effect led to the curvature changes in the sheet as the temperature went up or down during either insertion into the warm die or removal and subsequent air cooling. These thermal effects were captured by imposing different thermal expansion coefficients found previously in the literature [94], as specified in Section 5.2.8, for the elements that represent the core and clad layers.

In addition, to properly model springback of the clad later (AA4045), it becomes important to predict the stresses within that layer prior to springback which, in turn, requires a stress-strain curve for that layer versus the core layer. (The stress-strain data presented in Section 3.1.2 used for the forming models represents the aggregate or composite response of the core-clad brazing sheet.) Given that the clad layer has a nominal 0.02 mm thickness (the core layer is approximately 0.18 mm thick), direct measurement of the strain-strain response of the clad is quite difficult. In order to estimate the strength of the clad material, Vickers micro-hardness tests were performed, however, the indents could not be done on the edge of the clad layer since it is only 20 μm thick. Therefore, the tests were done on the surface (face) of the sheet with a very low force of 10 gf. In order to ensure that the indenter is not penetrating the clad layer, the indentation depth was calculated with the following formula:

$$h = \frac{d}{2\sqrt{2}\tan 68°} \tag{12}$$

where h is the indentation depth and d is the average diagonal length of the indent. The average diagonal length for the clad layer was 23 μm, which corresponds to the indentation depth of 3.3

μm. This indentation depth was much lower than the thickness of the clad layer and the hardness value was measured to be 36±1.6HV. In addition, similar hardness tests were performed on the core layer with the indents on both the sheet surface and edge to ensure that there is no difference between the two indentation locations/orientation. It was found that both locations yielded the same result of 71.9±2.6HV. Finally, the hardening behavior of the clad layer was approximated by scaling the flow curves for the core layer by one-half, the ratio between the hardness values. The resulting stress-strain curves are shown in Figure 126.

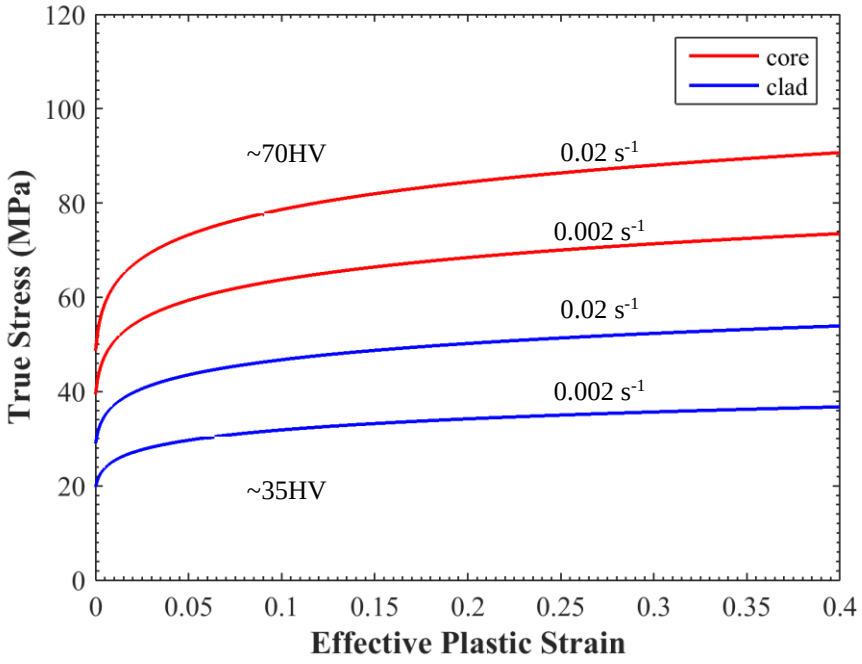

Figure 126: O-temper behavior predicted with the extended Nadai model at 250°C for core and clad layers

The stress-strain curves shown in Figure 126 were adopted for the majority of the springback simulations presented below. Note that the stress-strain curve shown for the core layer in Figure 126 is that used for the forming simulation studies presented in Chapter 4 and represents an average hardening response for the core-clad composite that comprises the brazing sheet.

6.1.2 Element Selection for Springback

Baseline springback simulations were performed using the shell element-based forming models presented in Chapter 3 and 4. As will be shown below, these models were able to capture the

influence of some of the important physical parameters (e.g. temperature) on degree of springback. However, the shell-based models were not able to capture the effect of punch load which was thought to produce through-thickness deformation known as coining or bottoming at higher load levels. This behavior cannot be captured with shell elements since they invoke a plane stress condition in which the stress in the thickness direction is zero. Therefore, coining effects cannot be captured with conventional sheet elements. A range of so-called "thick shell" element formulations, available in LS-DYNA, were investigated to capture the effect of though thickness stress, however, these attempts were unsuccessful (the models crashed).

As shown in the springback experiment, the bi-metallic nature of the sheet had strong influence on the springback behavior. Due to the difference in strength between the two layers, the sheet orientation at which the SHC is formed had an effect on the final springback. When the SHC was formed with the clad side up (inverted orientation), the springback was reduced compared to when the SHC was formed with the core side up (normal orientation). The difference in thermal expansion coefficient between the two layers also has an effect on springback. After the SHC is formed at elevated temperatures and cools down to room temperature, the part curls upwards as the top layer contracts more due to higher thermal expansion coefficient.

As an alternative approach, solid elements were considered to capture through-thickness deformation at high punch force. These elements introduce a high computational penalty since in explicit dynamic formulations, the time step is dependent upon the smallest element size and elements meshed through the thickness of a 0.2 mm sheet are very small. As a compromise, one approach that was adopted was to mesh the core region of the sheet using three solid elements and to use a single shell element to mesh the clad region, as shown in Figure 127. The location of the reference surface for the shell element was offset from the mid-plane to coincide with the surface of the solid element at the core-clad interface and these nodes were merged together. It is recognized that this approach is a gross simplification, however, use of a large number of solid elements throughout the thickness of the brazing sheet was not considered computationally feasible, particularly if the model were to be scaled to a full-size battery cooling plate (Figure 1).

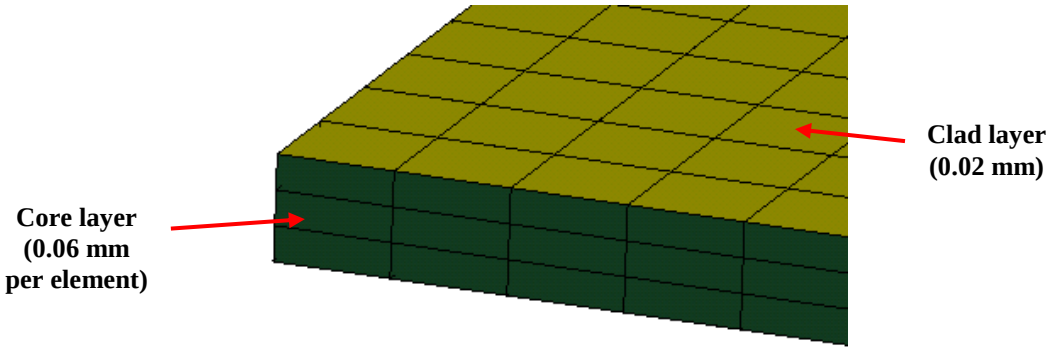

Figure 127: Blank mesh

The solid-shell discretization shown in Figure 127 was run for a number of forming and springback cases. For comparison purposes, a typical shell-based forming model (as presented in Chapters 3 and 4) required approximately 2.6 hours to run on an Intel Xeon E7-8870 cluster using 8 cores. The solid-shell model, with a 0.06 mm element size in the core, required 9 hours of computational time. A fully discretized solid element model, with one element in the 0.02 mm clad and six 0.03 mm elements in the core, was not attempted, but would require approximately 6-8 times longer to run based on the assumption of a 1/3 reduction in time step size and a corresponding 2 times increase in numbers of elements. It is recognized that the discretization shown in Figure 127 is likely too coarse to properly capture the residual stress distribution operative during springback after forming, however, this approach was adopted to study the effect of through-thickness deformation that cannot be captured using conventional thin shell elements.

6.1.3 Boundary Conditions for Springback Models

The forming models were run without the half-symmetry conditions considered in the formability studies (Chapters 3 and 4). Otherwise, all of the contact treatments and tooling motions in the formability studies were retained for the forming step in the springback simulations.

For the springback stage, the tooling is deleted and the part must be constrained to prevent all rigid body modes. Also the constraints should mimic the physical process used to measure springback so the simulation actually represents the physical process. The part was constrained the same way it was constrained in the experimental chapter in which a jig was used as shown in Figure 128. A

minimum number of nodes were used to prevent over-constraining the component which can result in a non-physical model.

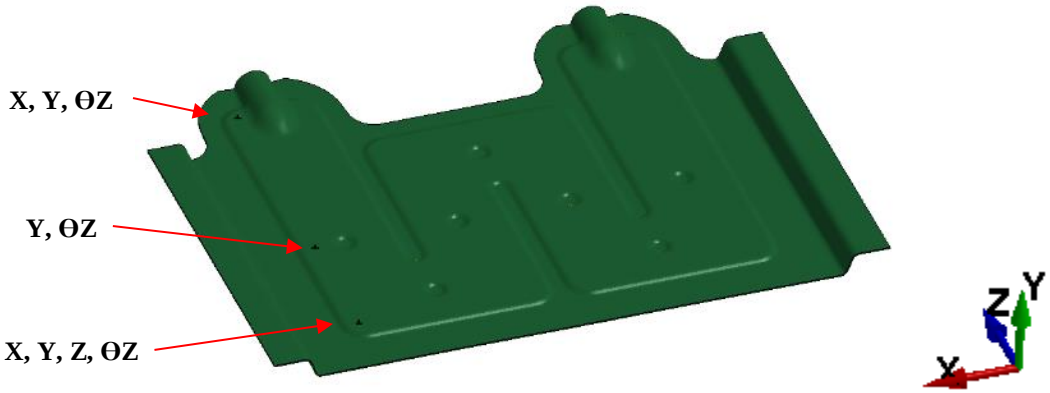

Figure 128: Forming simulation result and constrained nodes for springback simulation

Springback predictions were extracted from the numerical models in the same manner as they were measured in the experiments (see Figure 112). The x and y-coordinate data of the cross-section of the formed part were extracted after the springback simulation stage and used in the MATLAB script to calculate the y-displacement and curvature.

6.2 Forming Simulation Results

Since the effect of punch load has to be considered, the punch was displaced until the required punch load (10 or 80 kN) was achieved and then the forming simulation was terminated. The force-displacement results from the simulations are compared against the experimental results in Figure 129 and Figure 130. The force-displacement response at low punch load was predicted quite well for both temperature conditions. The simulated curves deviated very slightly at the end of the punch travel. At the high punch load condition, the simulation results deviated quite significantly for both temperature conditions as displacement increased. It was observed that the force response was greatly over-estimated and increased exponentially within very little displacement. The exact cause for this effect is unknown but some form of compression-related locking is suspected. The results also show that the two discretization methods, pure shell and solid-shell combination, produce similar responses.

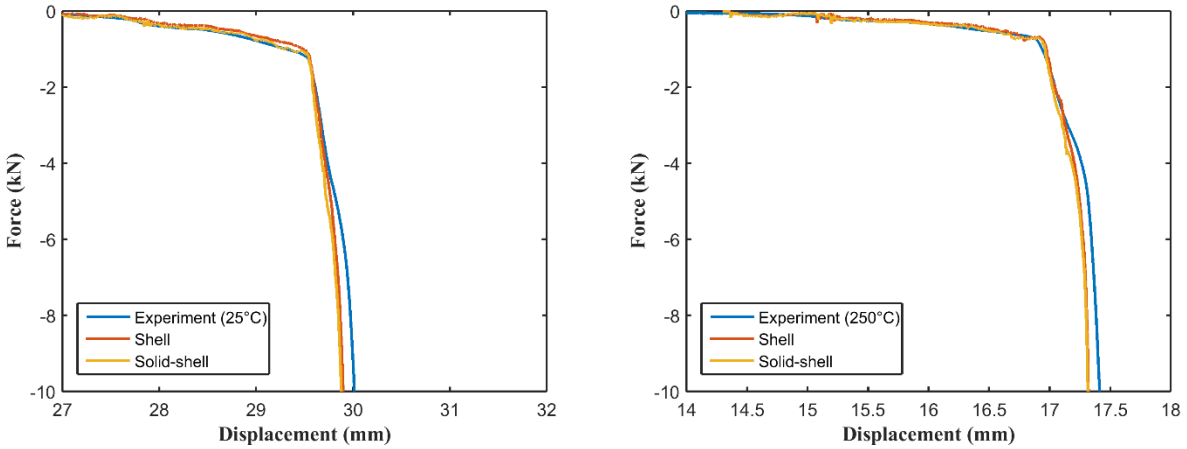

Figure 129: Experimental and predicted force-displacement curves at 10 kN punch load condition for 25°C (left) and 250°C (right) for H24 temper

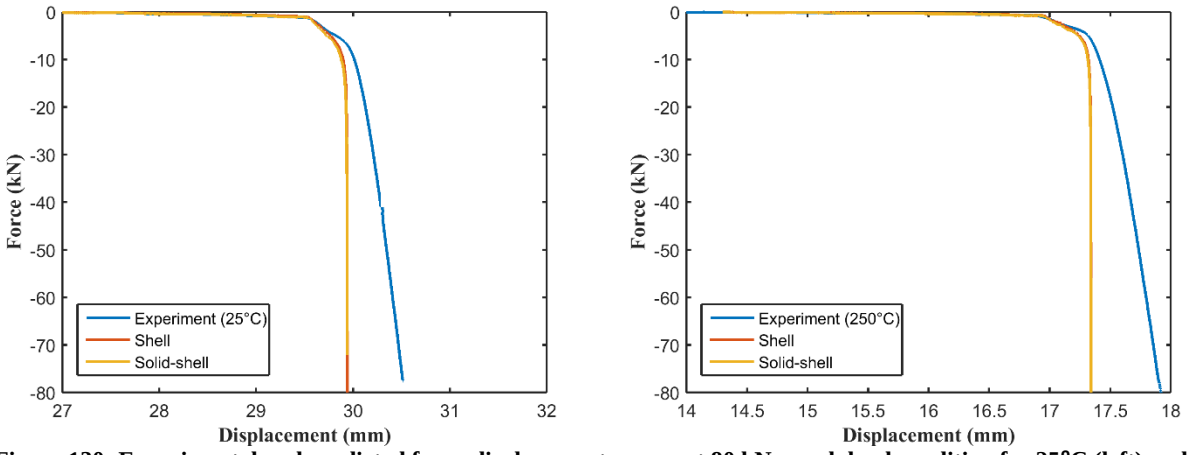

Figure 130: Experimental and predicted force-displacement curves at 80 kN punch load condition for 25°C (left) and 250°C (right) for H24 temper

The through-thickness strain distributions at the critical region around the I/O port (Figure 131) were measured to compare the two discretization methods and evaluate the effect of temperature and punch load on the strain distribution, as shown in Figure 132. The results show that the distribution was affected by the forming temperature but not the punch load for both mesh discretizations. Figure 133 compares the two discretization methods and shows that both predict similar trend in which the clad side has much higher strain compared to core. A slight deviation exists where the solid-shell mesh predicts higher strain on the core side.

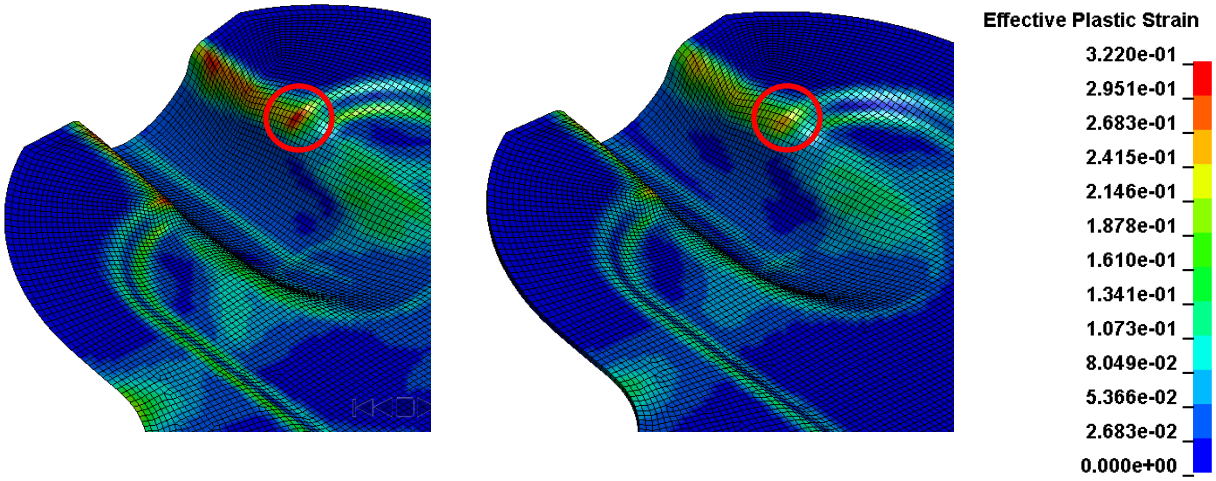

Figure 131: High strain element at which through-thickness strain distributions are obtained. Pure shell (left) and solid-shell (right) discretization

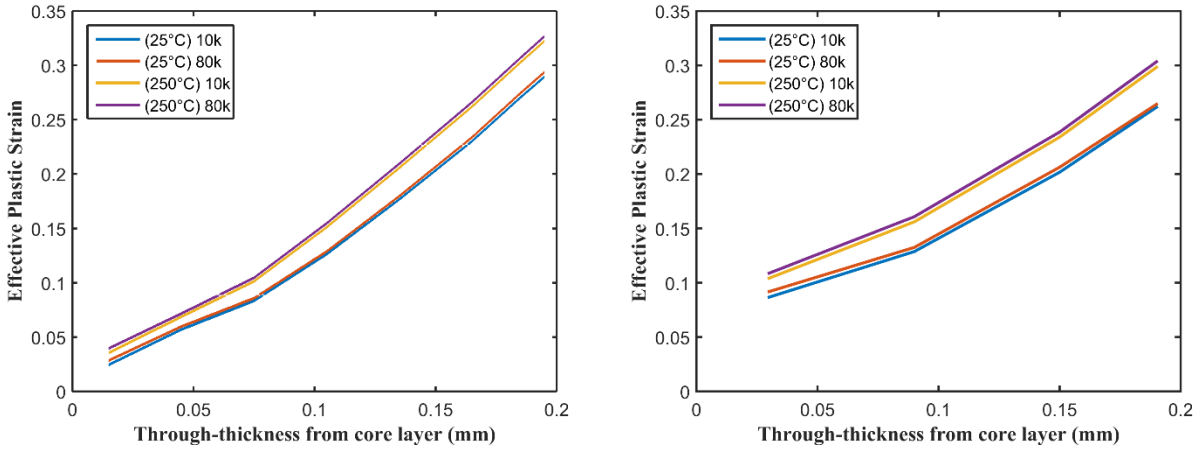

Figure 132: Through-thickness strain distribution for pure shell (left) and solid-shell (right) discretization

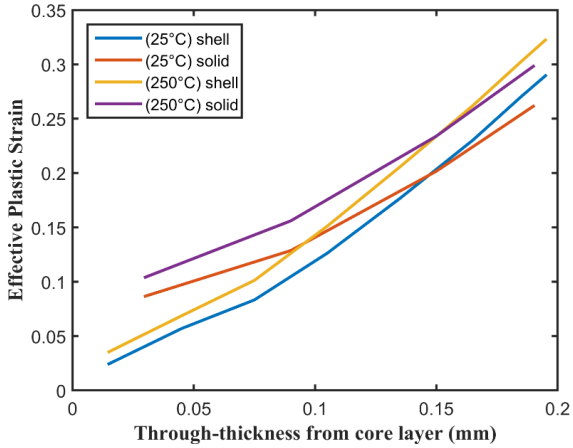

Figure 133: Through-thickness strain distribution for pure shell and solid-shell at 10kN load

6.3 Springback Simulation Results

Overall, the springback mode was predicted well in which one side of the SHC curled up as shown in Figure 134. It was demonstrated that the thermal expansion effect could be captured as shown below as the blue line which has more part deviation compared to the black line that does not consider the thermal expansion. However, due to lack of experimental measurements regarding this effect, it was not included in the subsequent springback simulations.

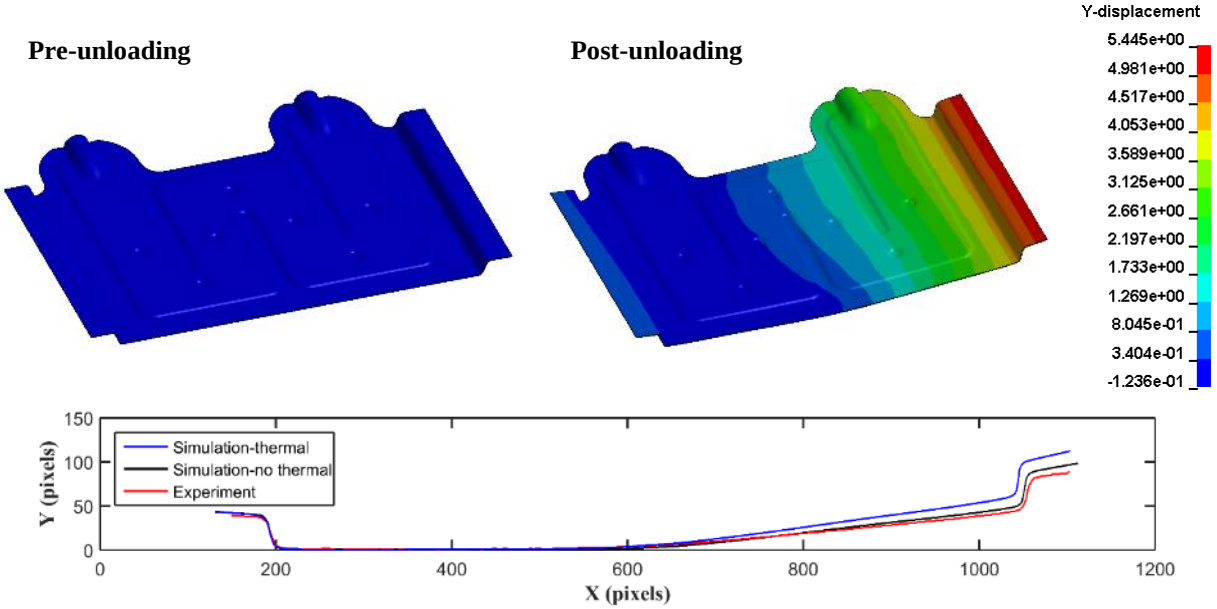

Figure 134: Springback simulation results (solid-shell model) for H24 formed at 250°C with Teflon lubricant

Figure 135 shows the comparison between simulation results predicted with blank meshed with shell elements and solid elements (Figure 127) for H24-temper formed with Teflon lubricant at different temperatures. The shell-based simulation results generally over-predicted springback and solid-based simulations had better correlation to the experimental results. Furthermore, the shell-based simulation would not be able to predict the coining effect on springback. The balance of the simulations in this thesis is performed with the solid-based blank mesh.

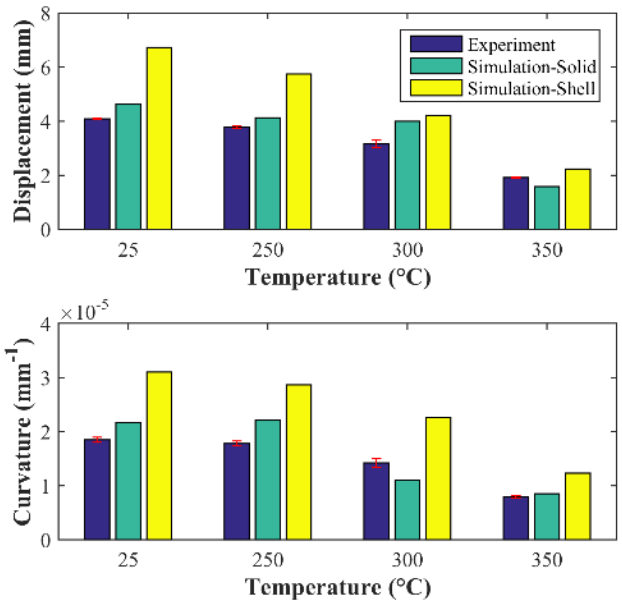

Figure 135: TC4: Experiment *vs.* simulation results for H24-temper formed with Teflon lubricant and 10kN punch load condition. A comparison between shell- and solid-based simulations.

Figure 136 to Figure 138 provide comparisons between the experiment and simulation results for the three tempers considered at dry conditions. For O-temper sheet, the simulations generally under-predicted springback (Figure 136). The under-prediction was more pronounced at higher temperature, probably due to the fact that the material model is extrapolated beyond temperatures above 250°C, the maximum considered by Verma [73]. Furthermore, O-temper has very low strength to begin with at room temperature, which degrades quickly as temperature increases due to thermal softening as predicted in the model. However, the overall trend was captured qualitatively in which springback actually increased at intermediate temperatures compared to room temperature as seen in the experiment. This trend was explained by the overall increase in strength-to-modulus ratio at elevated temperatures discussed previously.

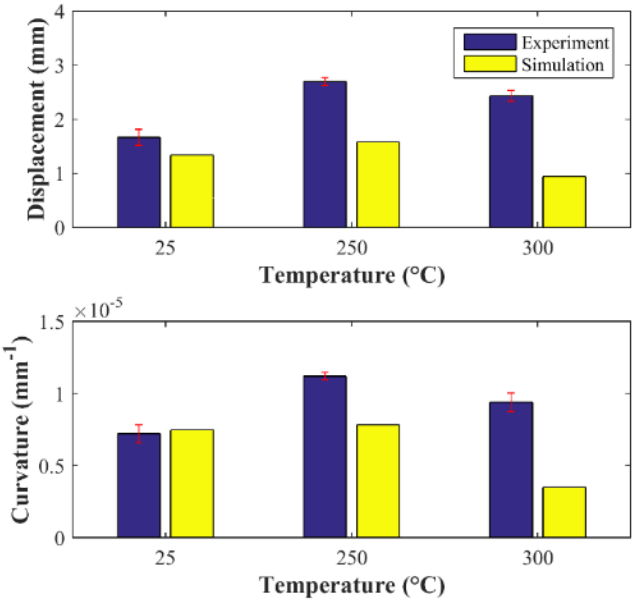

Figure 136: TC4: Experiment *vs.* simulation results for O-temper formed at dry and 10kN punch load condition

For the H22-temper, the springback behavior (Figure 137) was slightly over-predicted in the temperature range of 25°C and 300°C. However, springback was severely under-predicted at 350°C. Again this is probably due to poor extrapolation beyond the range of the material characterization experiments performed (up to 250°C). Furthermore, the extended Nadai model might not be suitable for very high warm forming temperatures such as 350°C. The H24-temper (Figure 138) results displayed modest over-prediction in all of the temperatures considered, but the general trend was captured.

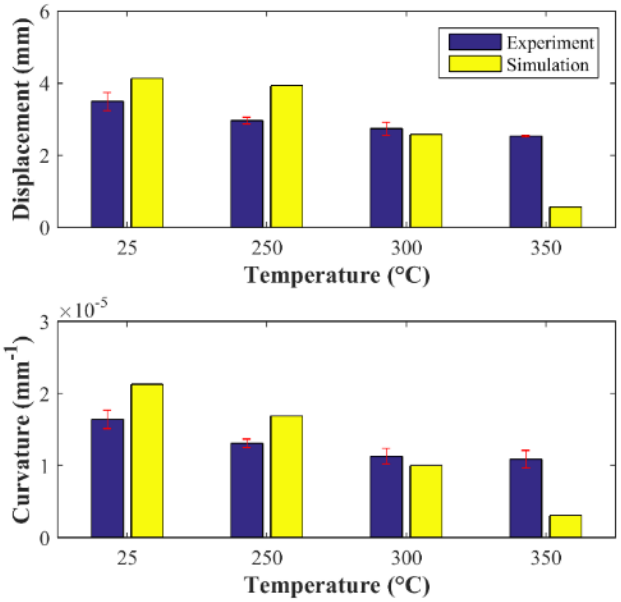

Figure 137: TC4: Experiment *vs.* simulation results for H22-temper formed at dry and 10kN punch load condition

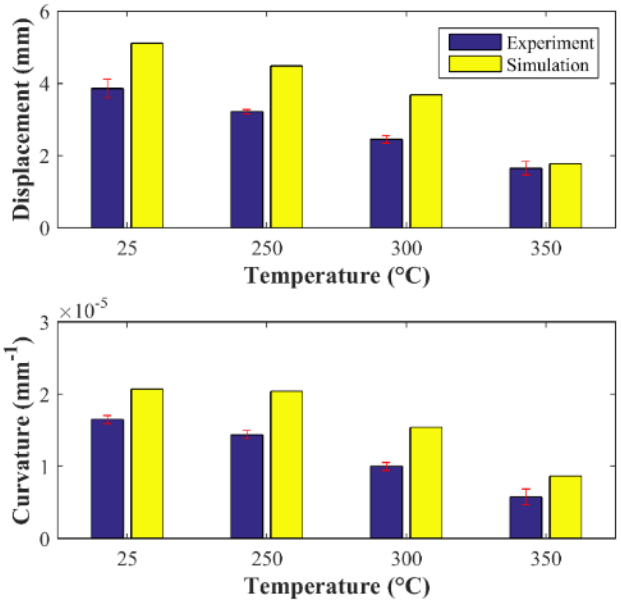

Figure 138: TC4: Experiment vs. simulation results for H24-temper formed at dry and 10kN punch load condition

Figure 139 shows the effect of sheet orientation in simulation of the H24-temper sheet formed at room temperature. As previously shown, there was a reduction in springback when the sheet was placed in the die with the clad layer oriented away from the braze joint. From Figure 139, it can be seen that the model captures this trend, although the change in springback reduction with sheet

orientation was larger than observed in the experiments. The over-prediction could be attributed to the simple approximation made for the strength of the clad layer based on the micro-hardness test results. More accurate flow behavior of the clad layer (AA4045) should be determined through tensile characterization.

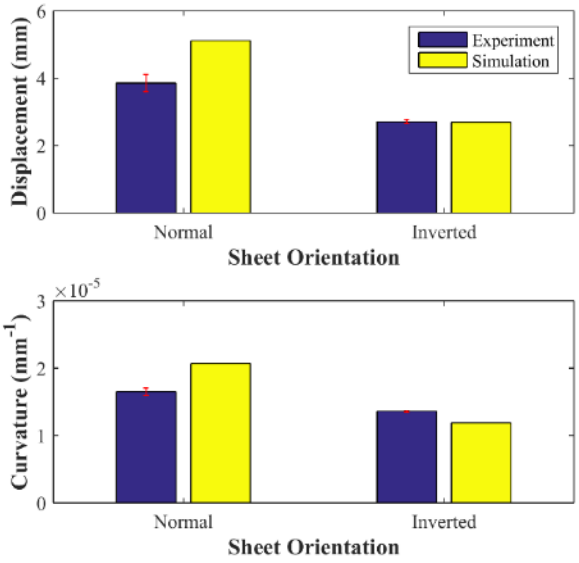

Figure 139: TC4: Effect of sheet orientation on H24 springback at 25°C and 10kN punch load condition

Figure 140 shows the predicted effect of Teflon versus dry lubrication on springback of the H24 parts. Overall, the predicted springback exceeded the measured values for each temperature considered. Also, the springback behavior of the component simulated at 300°C with Teflon exhibited unusual twisting behavior that was not observed in the experiments. The increase in springback with the use of lubricant in the experiments was not captured in the simulations for the y-displacement while it was observed in terms of the change in curvature. The reasons for this discrepancy are unknown.

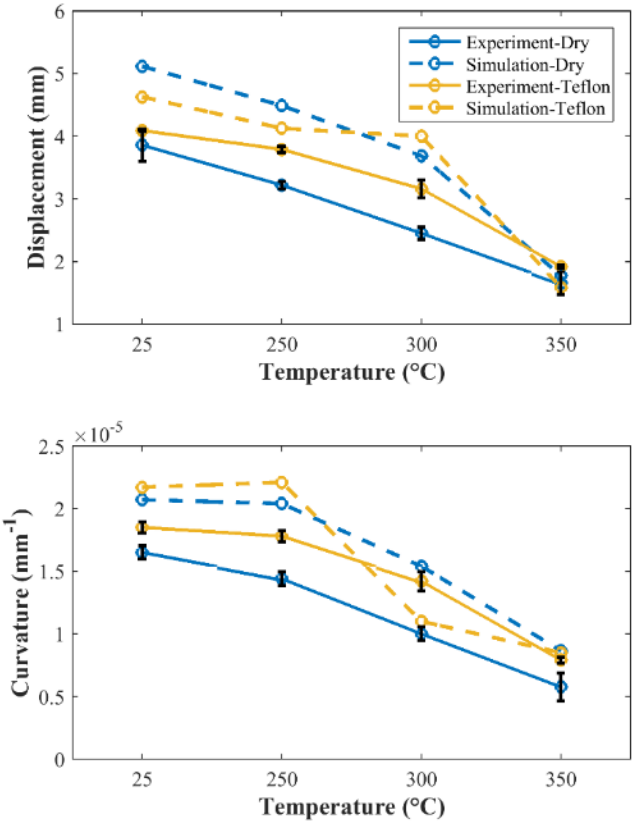

Figure 140: TC4: Effect of Teflon lubricant on H24 springback at 10kN punch load condition

Figure 141 shows the effect of punch of load (10 kN and 80 kN) on H24 springback. In the experiments, a significant reduction in springback was observed due to through-thickness deformation caused by high compressive loads. The simulation results show that the effect of punch load in reducing springback was predicted qualitatively, but the quantitative change was underestimated significantly.

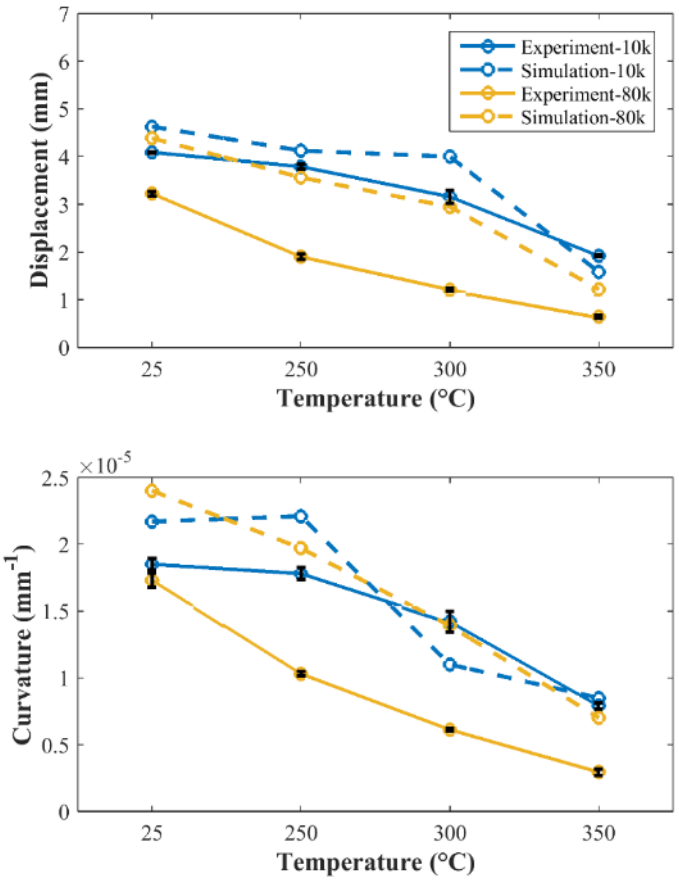

Figure 141: TC4: Effect of punch load on H24 springback (Teflon lubricated)

6.4 Summary

Overall, the springback simulations were able to predict the qualitative trends for both shell and solid-shell elements in displaying reduction in springback with increasing temperature. The shell-based simulation results were over-predicted compared to that of solid-based simulation which had much higher correlation to the experimental data. The thermal expansion effect was demonstrated but it should be validated in the experiment by more carefully measuring how much the part deviates when heated. The effect of sheet orientation was captured successfully with the simulation with the inverted sheet orientation displaying reduction in springback. The simulations were not able to capture the effect of lubricant and punch load on springback.

7 Conclusions and Recommendations

7.1 Conclusions

A component-level study has been performed to investigate the effect of warm forming on formability and springback behavior on aluminum alloy brazing sheet widely used in the automotive heat exchanger industry. The brazing sheet consisted of AA3003 core and AA4045 clad layers and manufactured to O-, H22- and H24-temper conditions. The following conclusions were derived from the results of this research:

1. Vickers hardness tests were performed after heating samples blanks to temperatures ranging from 25 to 350°C for pre-selected heating time of 40 seconds. The results show that there was no permanent reduction in strength (hardness) with increasing temperature.

2. Twist compression tests were performed to characterize the tribological behavior at elevated temperatures. It was found that the coefficient of friction (COF) is a strong function of temperature. For dry tests, the core side (AA3003) had significantly higher COF compared to the clad side (AA4045). Little difference was observed between the two layers using lubricant.

3. The extended Nadai model [32] was able to capture the negative hardening effect observed for harder temper materials at elevated temperatures.

4. Four different tooling configurations (TC1 to TC4) were developed to improve the formability and wrinkling behavior in the warm forming process.
   a. Parts formed using TC1 fractured at the I/O port region due to tight radii

b. A two-stage forming operation was implemented for TC2 to pre-form the I/O port region to promote a more uniform strain distribution to prevent strain localization in the second stage. The part displayed severe wrinkling.
c. TC3 included the optimized I/O port geometry and channel geometry in the first stage to increase formability and reduce wrinkling. Formability was improved but the design was ineffective in terms of reducing wrinkling behavior. An undesirable snap-through buckling effect was also introduced.
d. The TC4 (single-stage forming) introduced geometric modifications to the I/O port-cooling channel intersection and a developed blank was used to optimize the material flow into the I/O port feature while still maintaining a sufficient flange area for brazing. These changes significantly improved formability.
e. Multi-stage forming was quite effective in increasing formability but introduced part defects such as wrinkling and snap-through buckling.
f. Use of lubrication was essential to promote a successful forming operation, especially at elevated temperatures due to increase in COF
g. The punch velocity had minor adverse effects on formability
h. The benefit of warm forming on formability was not clearly observed as fracture and localization occurred at elevated temperatures

5. The springback behavior was characterized by studying a wide range of experimental parameters. Overall, warm forming was very effective in reducing springback. The results show that:
   a. Harder temper conditions exhibit higher springback. H24 springback was more than two-fold greater than that of O-temper.
   b. No beneficial effect of temperature was observed in terms of reducing springback for O-temper parts.
   c. Significant reduction in springback was observed for H22 and H24 with increases in temperature. The maximum reductions occurred at 325°C (51% and 68% respectively).
   d. The use of lubricant increased springback slightly (up to 15% at 350°C).
   e. An increase in punch speed reduced the benefit of warm forming.
   f. Initial coil set did not have an effect on springback.

g. Sheet direction did not have an effect on springback.
h. Sheet orientation had considerable effect on springback due to the strength and thermal expansion differences between the two layers. The inverted sheet orientation had 29% lower springback compared to the conventional sheet orientation (clad layer up).
i. Punch load increase from 10 kN to 80 kN and holding time (2 to 30 seconds) had significant impact on springback (up to 88% reduction observed at 325°C for 30 second holding time and 54% at 250C for 2 second holding time for H24-temper).

6. Springback simulations that take the thermal expansion and strength gradient and through-thickness compression into account were developed. This was accomplished by discretizing the mesh with a combination of solid and shell elements. The simulation results successfully predicted the qualitative trend in the experiment with satisfactory match to the measured data in regards to the temperature effects. The model was not able to accurately capture the effect of lubricant and punch load.

7.2 Recommendations

The following recommendations are made for future work:

1. Material characterization should be expanded to include higher temperature conditions (up to 350°C). More advanced material models that considers texture-based anisotropy and kinematic hardening (Bauschinger effect) should be considered.

2. The effect of through-thickness compression was underestimated in the numerical simulations. The cause for the underestimation should be identified to accurately capture the compression effect that has significant impact on springback. The blank mesh should be refined to contain more elements in the through-thickness direction to better capture the residual stress gradient.

3. Sheet thinning should be measured at critical locations to correlate forming temperature, punch load, and lubrication to formability quantitatively.

4. The effect of warm forming and lubricants on brazeability should be assessed to ensure the brazing performance is not hindered. Furthermore, the maximum allowable springback for the parts to be brazed successfully should be established.

5. The reduction in die clearance at elevated temperatures due to thermal expansion could have negative impact on warm formability; thus further investigation is needed.

6. Different friction characterization tests capable of measuring the coefficient of friction at very low sliding distance should be explored.

7. The mechanical behavior of the clad layer should be obtained with more reliable method such as tensile testing.

8 References

[1] A. Pesaran, "Battery Thermal Management in EVs and HEVs : Issues and Solutions," in *Advanced Automotive Battery Conference*, 2001, p. 10.

[2] S. Al-Hallaj and J. R. Selman, "Thermal modeling of secondary lithium batteries for electric vehicle/hybrid electric vehicle applications," *J. Power Sources*, vol. 110, no. 2, pp. 341–348, 2002.

[3] G.-H. Kim and A. Pesaran, "Battery Thermal Management System Design Modeling," in *22nd International Battery Hybrid and Fuel Cell Electric Vehicle Conference and Exhibition EVS22*, 2006, vol. 1, no. November, pp. 126–133.

[4] K. Abels, "US Patent US20120237805A1," 2012.

[5] W. S. Miller *et al.*, "Recent development in aluminium alloys for the automotive industry," *Mater. Sci. Eng. A*, vol. 280, no. 1, pp. 37–49, 2000.

[6] F. Shehata, M. J. Painter, and R. Pearce, "Warm forming of aluminium/magnesium alloy sheet," *J. Mech. Work. Technol.*, vol. 2, no. 3, pp. 279–290, 1978.

[7] S. Toros, F. Ozturk, and I. Kacar, "Review of warm forming of aluminum-magnesium alloys," *J. Mater. Process. Technol.*, vol. 207, no. 1–3, pp. 1–12, 2008.

[8] R. A. Ayres and M. L. Wenner, "Strain and strain-rate hardening effects in punch stretching of 5182-0 aluminum at elevated temperatures," *Metall. Trans. A*, vol. 10, no. 1, pp. 41–46, 1979.

[9] D. J. Lloyd, "The deformation of commercial aluminum-magnesium alloys," *Metall. Trans. A*, vol. 11, no. 8, pp. 1287–1294, 1980.

[10] D. Li and A. Ghosh, "Tensile deformation behavior of aluminum alloys at warm forming temperatures," *Mater. Sci. Eng. A*, vol. 352, no. 1–2, pp. 279–286, 2003.

[11] S. Kurukuri, "Simulation of Thermally Assisted Forming of Aluminum Sheet," 2010.

[12] T. Naka and F. Yoshida, "Deep drawability of type 5083 aluminium-magnesium alloy sheet under various conditions of temperature and forming speed," *J. Mater. Process. Technol.*, vol. 89–90, pp. 19–23, 1999.

[13] T. B. Stoughton, "General forming limit criterion for sheet metal forming," *Int. J. Mech. Sci.*, vol. 42, no. 1, pp. 1–17, 2000.

[14] A. K. Ghosh, "The influence of strain hardening and strain-rate sensitivity on sheet metal forming," *Trans. ASME J. Engng Mater. Technol.*, vol. 99, no. 1, pp. 264–274, 1977.

[15] S. S. Hecker, "Formability of Aluminum Alloy Sheets," *J. Eng. Mater. Technol.*, vol. 97, no. 1, pp. 66–73, 1975.

[16] G. J. Davies et al., "Superplasticity : A Review," *J. Mater. Sci.*, vol. 5, no. 12, pp. 1091–1102, 1970.

[17] R. A. Ayres, "Enhanced ductility in an aluminum-4 Pct magnesium alloy at elevated temperature," *Metall. Trans. A*, vol. 8, no. 3, pp. 487–492, 1977.

[18] D. Li and A. K. Ghosh, "Biaxial warm forming behavior of aluminum sheet alloys," *J. Mater. Process. Technol.*, vol. 145, no. 3, pp. 281–293, 2004.

[19] P. J. Bolt, N. A. P. M. Lamboo, and P. J. C. M. Rozier, "Feasibility of warm drawing of aluminium products," *J. Mater. Process. Technol.*, vol. 115, no. 1, pp. 118–121, 2001.

[20] M. M. H. Takuda, K. Mori, I. Masuda, Y. Abe, ""Finite element simulation of warm deep drawing of aluminium alloy sheet when accounting for heat conduction," *J. Mater. Process. Tech.*, vol. 120, pp. 412–418, 2002.

[21] S. Kaya, G. Spampinato, and T. Altan, "An Experimental Study on Nonisothermal Deep Drawing Process Using Aluminum and Magnesium Alloys," *J. Manuf. Sci. Eng.*, vol. 130, no. 6, 2008.

[22] A. H. van den Boogaard and J. Huétink, "Simulation of aluminium sheet forming at elevated temperatures," *Comput. Methods Appl. Mech. Eng.*, vol. 195, no. 48–49, pp. 6691–6709, 2006.

[23] Y. Bergstrom, "A Dislocation Model for the Stress-Strain Behaviour of Polycrystalline Alpha-Fe with Special Emphasis on the Variation of the Densities of Mobile and Immobile Dislocations," *Mater. Sci. Eng.*, vol. 5, no. 4, pp. 193–200, 1969.

[24] R. Hill, "A theory of the yielding and plastic flow of anisotropic metals," *Proc. R. Soc. London, Ser. A*, vol. 193, no. 1033, 1948.

[25] H. Vegter, "A plane stress yield function for anisotropic sheet material by interpolation of biaxial stress states," *Int. J. Plast.*, vol. 22, pp. 557–580, 2006.

[26] N. Abedrabbo, F. Pourboghrat, and J. Carsley, "Forming of aluminum alloys at elevated temperatures – Part 2 : Numerical modeling and experimental verification," *Int. J. Plast.*, vol. 22, pp. 342–373, 2006.

[27] F. Barlat, Y. Maeda, Y. Hayashida, S. J. Murtha, S. Hattori, and R. C. Becker, "YIELD FUNCTION DEVELOPMENT

ALLOY SHEETS FOR ALUMINUM," *J. Mech. Phys. Solids*, vol. 45, no. 11–12, pp. 1727–1763, 1997.
[28] G. Palumbo and L. Tricarico, "Numerical and experimental investigations on the Warm Deep Drawing process of circular aluminum alloy specimens," *J. Mater. Process. Tech.*, vol. 184, pp. 115–123, 2007.
[29] D. G. Tari and M. J. Worswick, "Elevated temperature constitutive behavior and simulation of warm forming of AZ31B," *J. Mater. Process. Tech.*, vol. 221, pp. 40–55, 2015.
[30] D. G. Tari, M. J. Worswick, U. Ali, and M. A. Gharghouri, "Mechanical response of AZ31B magnesium alloy : Experimental characterization and material modeling considering proportional loading at room temperature," *Int. J. Plast.*, vol. 55, pp. 247–267, 2014.
[31] O. Cazacu, B. Plunkett, and F. Barlat, "Orthotropic yield criterion for hexagonal closed packed metals," *Int. J. Plast.*, vol. 22, pp. 1171–1194, 2006.
[32] A. H. Van Den Boogaard and J. Huétink, "Modeling of AlMg sheet forming at elevated temperatures," *Int. J. Form. Process.*, vol. 4, pp. 361–375, 2001.
[33] K. Ghavam, "Analysis of Nonisothermal Deep Drawing of Aluminum Alloy Sheet With Induced Anisotropy and Rate Sensitivity at Elevated Temperatures," *J. Manuf. Sci. Eng.*, vol. 136, pp. 1–16, 2013.
[34] F. Barlat, J. C. Brem, J. W. Yoon, K. Chung, and R. E. Dick, "Plane stress yield function for aluminum alloy sheets — part 1 : theory," vol. 19, pp. 1297–1319, 2003.
[35] R. Bagheriasl, K. Ghavam, and M. J. Worswick, "Formability improvement with independent die and punch temperature control," *Int. J. Mate. Form.*, vol. 7, no. 2, pp. 139–154, 2014.
[36] S. Kurukuri, "Constitutive modelling of aluminium alloy sheet at warm forming temperatures," *J. Phys. Conf. Ser.*, vol. 734, 2016.
[37] E. Nes, K. Marthinsen, B. Holmedal, E. Nes, K. Marthinsen, and B. Holmedal, "The effect of boundary spacing on substructure strengthening The effect of boundary spacing on substructure strengthening," *Mat. Sci. Tech.*, vol. 17, pp. 1377–1382, 2004.
[38] S. Dicecco, C. Butcher, M. Worswick, E. Boettcher, E. Chu, and C. Shi, "Determination of Forming Limit Diagrams of AA6013-T6 Aluminum Alloy Sheet using a Time and Position Dependent Localized Necking Criterion," *IOP Conf. Ser. Mater. Sci. Eng.*, vol. 159, no. 1, 2016.
[39] W. Hui, L. U. O. Ying-bing, P. Friedman, C. Ming-he, and G. A. O. Lin, "Warm forming behavior of high strength aluminum alloy AA7075," *Trans. Nonferrous Met. Soc. China*, vol. 22, no. 1, pp. 1–7, 2012.
[40] M. Kumar, N. Sotirov, and C. M. Chimani, "Investigations on warm forming of AW-7020-T6 alloy sheet," *J. Mater. Process. Tech.*, vol. 214, no. 8, pp. 1769–1776, 2014.
[41] R. Bagheriasl and M. J. Worswick, "Formability of AA3003 brazing sheet at elevated temperatures: Limiting dome height experiments and determination of forming limit diagrams," *Int. J. Mater. Form.*, vol. 8, no. 2, pp. 229–244, 2015.
[42] J. Mckinley, "Warm Forming of Aluminum Brazing Sheet," 2010.
[43] E. Jain, "Investigation of Effect of Temperature and Forming Speed on the Formability of AA3003 Brazing Sheets," 2016.
[44] A. El-Megharbel, "Springback and Residual Stresses After Stretch Bending of Warmhardening Sheet Metal," *J. Mater. Process. Tech.*, vol. 24, pp. 191–200, 1990.
[45] S. K. Panthi, N. Ramakrishnan, M. Ahmed, S. S. Singh, and M. D. Goel, "Finite Element Analysis of sheet metal bending process to predict the springback," *Mater. Des.*, vol. 31, no. 2, pp. 657–662, 2010.
[46] K. Ã. Mori, K. Akita, and Y. Abe, "Springback behaviour in bending of ultra-high-strength steel sheets using CNC servo press," *Int. J. Mach. Tools Manuf.*, vol. 47, no. 2, pp. 321–325, 2007.
[47] R. K. Verma and A. Haldar, "Effect of normal anisotropy on springback," *J. Mater. Process. Tech.*, vol. 190, pp. 300–304, 2007.
[48] M. L. Garcia-romeu, J. Ciurana, and I. Ferrer, "Springback determination of sheet metals in an air bending process based on an experimental work," *J. Mater. Process. Tech.*, vol. 191, pp. 174–177, 2007.
[49] M. Samuel, "Experimental and numerical prediction of springback and side wall curl in U-bendings of anisotropic sheet metals," *J. Mater. Process. Tech.*, vol. 105, pp. 382–393, 2000.
[50] F. Yoshida and T. Uemori, "A model of large-strain cyclic plasticity and its application to springback simulation," *Int. J. Mech. Sci.*, vol. 45, pp. 1687–1702, 2003.
[51] E. H. Ouakdi, R. Louahdi, D. Khirani, and L. Tabourot, "Evaluation of springback under the effect of holding force and die radius in a stretch bending test," *Mater. Des.*, vol. 35, pp. 106–112, 2012.
[52] K. P. Li, W. P. Carden, and R. H. Wagoner, "Simulation of springback," *Int. J. Mech. Sci.*, vol. 44, pp. 103–122, 2002.
[53] Z. Dongjuan, C. Zhenshan, R. Xueyu, and L. Yuqiang, "An analytical model for predicting springback and side wall curl of sheet after U-bending," *Comput. Mater. Sci.*, vol. 38, pp. 707–715, 2007.
[54] J. Gau and G. L. Kinzel, "An experimental investigation of the influence of the Bauschinger effect on springback predictions," *J. Mater. Process. Tech.*, vol. 108, no. 3, pp. 369–375, 2001.
[55] R. H. Wagoner, "Sheet Springback," in *Continuum Scale Simulation of Engineering Materials*, vol. 42, 2005, pp. 758–774.
[56] A. Baba and Y. Tozawa, "Effect of tensile force in stretch-forming process on the springback," *Bull. JSME*, vol. 7, pp. 835–843, 1964.
[57] Y. C. Liu and E. Procedure, "The Effect of Restraining Force on Shape Deviations in Flanged Channels," *J. Eng. Mater. Technol.*, vol. 110, pp. 389–394, 1988.
[58] D. Schmoeckel and M. Beth, "Springback Reduction in Draw-Bending Process of Sheet Metals," *CIRP Ann. - Manuf.*

Tech., vol. 42, no. I, pp. 339–342, 1993.
[59] R. H. Wagoner, H. Lim, and M. Lee, "Advanced Issues in springback," *Int. J. Plast.*, vol. 45, pp. 3–20, 2013.
[60] A. P. Karafillis; and M. C. Boyce, "Tooling Design in Sheet Metal Forming Using Springback Calculations," *Int. J. Mech. Sci.*, vol. 34, no. 2, pp. 113–131, 1992.
[61] W. Gan and R. H. Wagoner, "Die design method for sheet springback," *Int. J. Mech. Sci.*, vol. 46, pp. 1097–1113, 2004.
[62] J. Weiher, B. Rietman, K. Kose, S. Ohnimus, and M. Petzoldt, "Controlling Springback With Compensation Strategies," in *AIP Conference Proceedings 712*, 2004, vol. 712, no. 1.
[63] R. Lingbeek, J. Hu, S. Ohnimus, M. Petzoldt, and J. Weiher, "The development of a finite elements based springback compensation tool for sheet metal products," *J. Mater. Process. Tech.*, vol. 169, pp. 115–125, 2005.
[64] Y. H. Moon, S. S. Kang, J. R. Cho, and T. G. Kim, "Effect of tool temperature on the reduction of the springback of aluminum sheets," *J. Mater. Process. Tech.*, vol. 132, pp. 365–368, 2003.
[65] J. Yanagimoto and K. Oyamada, "Springback-free Isothermal Forming of High-strength Steel Sheets and Aluminum Alloy Sheets under Warm and Hot Forming Conditions," *ISIJ Int.*, vol. 46, no. 9, pp. 1324–1328, 2006.
[66] H. Kim and M. Koc, "Numerical investigations on springback characteristics of aluminum sheet metal alloys in warm forming conditions," *J. Mater. Process. Tech.*, vol. 204, pp. 370–383, 2008.
[67] F. Ozturk, S. Toros, S. Kilic, and M. H. Bas, "Effects of cold and warm temperatures on springback of aluminium – magnesium alloy 5083-H111," in *Proc. IMechE*, 2009, vol. 223, pp. 427–431.
[68] R. Greze, P. Y. Manach, H. Laurent, S. Thuillier, and L. F. Menezes, "Influence of the temperature on residual stresses and springback effect in an aluminium alloy," *Int. J. Mech. Sci.*, vol. 52, pp. 1094–1100, 2010.
[69] H. Laurent, J. Coër, P. Y. Manach, M. C. Oliveira, and L. F. Menezes, "Experimental and numerical studies on the warm deep drawing of an Al-Mg alloy," *Int. J. Mech. Sci.*, vol. 93, pp. 59–72, 2015.
[70] B. J. E. Hockett, "LARGE STRAIN ~ EFURMATIUN OF POLYCRYSTALLINE METALS AT LOW," *J. Mech. Phys. Solids*, vol. 23, pp. 87–98, 1975.
[71] K. Takata, "Warm Forming of Aluminum Alloys," 2013.
[72] A. Wang *et al.*, "Springback analysis of AA5754 after hot stamping : experiments and FE modelling," *Int. J. Adv. Manuf. Technol.*, vol. 89, no. 5–8, pp. 1339–1352, 2016.
[73] R. Verma, "Effect of Elevated Temperature on Mechanical Behaviour and Springback of Aluminum Alloy Brazing Sheets," 2016.
[74] M. J. Benoit, M. A. Whitney, and M. A. Wells, "Effect of Temperature and Sheet Temper on Isothermal Solidification Kinetics in Clad Aluminum Brazing Sheet," *Metall. Mater. Trans. A*, vol. 47, no. 9, pp. 4425–4436, 2016.
[75] M. J. Benoit, R. Kaur, M. A. Wells, H. Jin, B. S. Amirkhiz, and S. Winkler, "Sagging resistance of warm formed aluminum brazing sheet," *J. Mater. Process. Tech.*, vol. 254, no. November 2017, pp. 353–360, 2018.
[76] *ZRCI-301*. 2005.
[77] *Standard Test Method for Microindentation Hardness of Materials*. 2016.
[78] J. Noder, "Characterization and Simulation of Warm Forming of 6xxx and 7xxx Series Aluminum Alloys by," 2017.
[79] J. A. Schey, "Tribology in Metalworking: Friction, Lubrication, and Wear," *J. Appl. Metalwork.*, vol. 3, no. 2, pp. 173–173, 1984.
[80] M. J. Worswick, M. A. Wells, and K. J. Daun, "Warm Forming of Aluminum Alloy Brazing Sheet – Progress Report (Confidential). University of Waterloo, Waterloo, Canada," 2015.
[81] W. G. Beare and F. P. Bowden, "Physical Properties of Surfaces I - Kinetic Friction," *Philos. Trans. R. Soceity London*, 1935.
[82] E. Voce, "A Practical Strain-hardening Function," *Metallurgica*, vol. 51, pp. 219–226, 1955.
[83] A. H. van den Boogaard, "Modelling of aluminum sheet forming at elevated temperatures," in *AIP Conference Proceedings 712*, 2004, vol. 712, no. 1.
[84] A. K. Ghosh, "The Influence of Strain Hardening and Strain- Rate Sensitivity on Sheet letal Forming," *J. Eng. Mater. Technol*, vol. 99, no. 3, pp. 264–274, 1977.
[85] R. E. N. Kahl and H. Ekstro, "Tensile , Fatigue , and Creep Properties of Aluminum Heat Exchanger Tube Alloys for Temperatures from 293 K to 573 K," *Metall. Mater. Trans. A*, vol. 45, no. 2, pp. 663–681, 2014.
[86] LSTC, "LS-DYNA_Manual_Volume_I_R8.0," vol. I. .
[87] X. Wang and J. Cao, "On the prediction of side-wall wrinkling in sheet metal forming processes," *Int. J. Mech. Sci.*, vol. 42, no. 12, pp. 2369–2394, 2000.
[88] R. Wiebe and L. N. Virgin, "On Snap-Through Buckling," *Struct. Struct. Dyn. Mater. Conf.*, 2011.
[89] K. Omer, "Private Communication." .
[90] M. D. Hanna, "Tribological evaluation of aluminum and magnesium sheet forming at high temperatures," *Wear*, vol. 267, pp. 1046–1050, 2009.
[91] R. Hino, Y. Goto, and F. Yoshida, "Springback of sheet metal laminates in draw-bending," *J. Mater. Process. Tech.*, vol. 139, pp. 341–347, 2003.
[92] D. Leu and C. Hsieh, "The influence of coining force on spring-back reduction in V-die bending process," *J. Mater. Process. Tech.*, vol. 196, no. 1–3, pp. 230–235, 2008.
[93] A. Forcellese, L. Fratini, F. Gabrielli, and F. Micari, "The evaluation of springback in 3D stamping and coining processes," *J. Mater. Process. Tech.*, vol. 80–81, pp. 108–112, 1998.
[94] *Properties and Selection: Nonferrous Alloys and Special-Purpose Materials*, vol. 2. 1990.